Influence of defects and disorder on anomalous Hall effect and spin Seebeck effect on permalloy and Heusler compounds

Dissertation zur Erlangung des Grades

Doktor der Naturwissenschaften

am Fachbereich Physik
der Johannes Gutenberg-Universität Mainz

Enrique Vilanova Vidal
geb. in Valencia (Spanien)

Mainz, 2012

Abstract

In this work Heusler thin films have been prepared and their transport properties have been studied. Of particularly interest is the anomalous Hall effect (AHE). The effect is a long known but still not fully understood transport effect. Most theory papers focus on the influence of one particular contribution to the AHE. Actual measured experimental data, however, often are not in accordance with idealized assumptions. This thesis discusses the data analysis for materials with low residual resistivity ratios. As prototypical materials, half metallic Heusler compounds are studied. Here, the influence of defects and disorder is apparent in a material with a complex topology of the Fermi surface.

Using films with different degrees of disorder, the different scattering mechanisms can be separated. For $Co_2FeSi_{0.6}Al_{0.4}$ and $Co_2FeGa_{0.5}Ge_{0.5}$, the AHE induced by B2-type disorder and temperature-dependent scattering is positive, while DO_3-type disorder and possible intrinsic contributions possess a negative sign.

For these compounds, magneto-optical Kerr effects (MOKE) are investigated. First order contributions as a function of intrinsic and extrinsic parameters are qualitatively analyzed. The relation between the crystalline ordering and the second order contributions to the MOKE signal is studied.

In addition, sets of the Heusler compound Co_2MnAl thin films were grown on MgO (100) and Si (100) substrates by radio frequency magnetron sputtering. Composition, magnetic and transport properties were studied systematically for samples deposited at different conditions.

In particular, the anomalous Hall effect resistivity presents an extraordinarily temperature independent behavior in a moderate magnetic field range from 0 to 0.6 T. The off-diagonal transport at temperatures up to 300 °C was analyzed. The data show the suitability of the material for Hall sensors working well above room temperature.

Recently, the spin Seebeck effect (SSE) has been discovered. This effect is within the framework of spin caloritronics and it generates a "spin voltage" due to a temperature gradient in magnetic materials. Here, the preliminary measurements of the spin-Seebeck effect in permalloy and Heusler compounds are presented.

Kurzzusammenfassung

In dieser Arbeit wurden dünne Schichten von Heusler-Verbindungen hergestellt und auf ihre Transporteigenschaften hin untersucht. Der Anomale Hall-Effekt (AHE) ist dabei von besonderem Interesse. Er ist ein seit langer Zeit bekannter, jedoch noch nicht vollständig verstandener Transport-Effekt. Die meisten Veröffentlichungen theoretischer Arbeiten konzentrieren sich auf den Einfluss eines bestimmten Beitrags zum AHE. Tatsächlich gemessene experimentelle Daten können jedoch oft nicht in Einklang mit idealisierten Annahmen gebracht werden. Die vorliegende Arbeit diskutiert die Ergebnisse, welche aus Messungen von Materialien mit niedrigem Restwiderstand erhalten wurden. Als prototypische Materialien wurden hier hyphenation Heusler-Verbindungen untersucht. Als Material mit einer komplexen Topologie der Fermi-Fläche zeichnet sich dort der Einfluss von Defekten und der Unordnung der Kristallstruktur deutlich ab.

Durch Verwendung von Filmen mit unterschiedlichem Grad der Unordnung können verschiedene Streumechanismen unterschieden werden. Für $Co_2FeSi_{0.6}Al_{0.4}$ and $Co_2FeGa_{0.5}Ge_{0.5}$ zeigt sich ein positiver AHE bei einer Unordnung vom Typ B2 und bei einer induzierten temperaturabhängigen Streuung, wo hingegen eine Typ DO_3-Unordnung zusammen mit anderen möglichen intrinsischen Beiträgen einen negativen Effekt hervorruft.

Darüber hinaus wurden die magneto-optische Kerr-Effekte (MOKE) dieser Verbindungen untersucht. Hierfür wurden Beiträge erster Ordnung als Funktion der intrinsischen und extrinsischen Parameter qualitativ analysiert. Auf den Einfluss der kristallinen Ordnung auf Beiträge zweiter Ordnung des MOKE-Signals wird ebenfalls eingegangen.

Des Weiteren wurden dünne Schichten der Heusler-Verbindung Co_2MnAl auf MgO- und Si-Substraten (beide (100)) mit Hochfrequenz-Magnetron-Sputtern erzeugt. Die zusammensetzung sowie die magnetischen und Transport-Eigenschaften wurden hinsichtlich unterschiedlicher Abscheidebedingungen systematisch untersucht.

Insbesondere zeigt der AHE-Widerstand ein außerordentliches temperaturunabhängiges Verhalten in einem Bereich moderater Magnetfeldstärken von 0 bis 0,6 T. Hierfür wurde der nicht-diagonale Transport bei Temperaturen bis zu 300 °C analysiert. Die Daten zeigen die Eignung des Materials für Hall-Sensoren auch oberhalb der Raumtemperatur.

Jüngst wurde der Spin Seebeck-Effekt (SSE) entdeckt. Der Effekt aus dem Bereich der Spin-Kaloritronik erzeugt eine "Spin-Spannung" aufgrund eines Temperaturgradienten in magnetischen Materialien. Hier werden vorläufige Messungen des SSE in $Ni_{80}Fe_{20}$ und in Heusler-Verbindungen präsentiert.

Contents

List of Figures

Chapter 1

Introduction

In 1873, James Clerk Maxwell published the book *"Treatise on Electricity and Magnetism"*. He presented and conceptually and formally described the idea of an electromagnetic wave and gave an introduction of the unification between electricity and magnetism. Thirty years later, Sir John Ambrose Fleming invented the vacuum tube and the age of electronics began. The electronic technology is based on the use and control of charged particles. In the last century this field has improved strongly in its achievements. The invention of the triode in 1904 by Lee De Forest and the later introduction of the transistor in 1948 by Bardeen and Brattain and further uses of semiconductors are the early key steps in the electronics.

This theoretical framework provides a robust formulation to describe electromagnetic effects. Despite this, a complete understanding of some of these effects remains in materials, inadequately explained. An example is the Hall effect which refers to a transversal current to a non-parallel applied electric and magnetic field. As a consequence of the Lorentz force, the electrons are deflected in the transversal direction leading to a measurable voltage. The system can be described by

$$\begin{pmatrix} E_x \\ E_y \end{pmatrix} = \begin{pmatrix} \rho_{xx} & -\rho_{xy} \\ \rho_{xy} & \rho_{xx} \end{pmatrix} \cdot \begin{pmatrix} j_x \\ 0 \end{pmatrix}, \tag{1.1}$$

where ρ_{xx} and ρ_{xy} are the longitudinal and the transversal resistivities, respectively. However, an excess of the transverse Hall voltage, the so-called Anomalous Hall effect (AHE), is observed in materials with broken time-reversal symmetry like ferromagnets (contained in ρ_{xy}). The AHE has attracted significant theoretical and experimental efforts in the last decades. Even nowadays, there exists no complete understanding of this effect to predict experimental data. Nevertheless, recent progress using semiclassical transport and Green's-function theory have contributed to clarify the

phenomenon. From the applied point of view, the AHE is a suitable tool in the context of spintronics. It can be used to control and generate spin polarized currents.

A main part of this thesis focuses its attention on analyzing the role of defects (dislocations, grain boundaries) and disorder in the AHE. The data treatment is also another challenging aspect to deal with. In particular, splitting the different contributions which are mixed together in the measured raw data.

To detect the contribution arising from defects and disorder to the AHE, materials sensitive to different concentration of both are required i.e. materials which present a measurable change of Fermi surface in relation with the concentration of defects and disorder. This change leads to a measurable effect of the AHE. Heusler compounds fulfill this condition. These compounds can possess $L2_1$, DO_3, B2 and A2 crystal structures. A change in the crystal structure will lead a change in the Fermi surface. Therefore, measurable variations in the AHE are expected, accordingly.

Aside, one of the studied Heusler compounds in this thesis presents attractive properties for applications. A Giant Hall Effect is driven by the AHE and an extraordinary temperature independent behavior in a moderate magnetic field range from 0 to 0.6 Tesla. The off-diagonal transport at temperatures up to 300 °C is analyzed. The data show the suitability of the material for Hall sensors working well above room temperature. Such sensor can have a wide application in the automotive industry where a temperature range well above RT is wanted in order to place the sensor close to the engine. A sensor based on this Heusler compound is sketched. It also presents some challenges which are discussed and possible solutions are presented.

The effects of the crystal structure on magnetic and optical properties of the Heusler compounds were also investigated. QMOKE ellipsometry measurements were performed in collaboration with the "Technische Universitaet Kaiserslautern".

Another important topic of the thesis focuses on the study of the Seebeck effect (SE) in the context of the spin caloritronics.

In 1821, Thomas Johann Seebeck, observed the conversion of a temperature difference into a charge current. In his experiment, a compass needle was deflected by a closed loop. The loop was made of two different metals joint to each other. The two metallic junctions were exposed to different temperatures.

The cause of this phenomena lies in two mechanisms. One mechanism is a charge carrier diffusion from a side with a higher charge carrier density to the side with a lower value. The second is electron-phonon interaction, so-called phonon drag. If one establishes a temperature gradient along one sample, the

phonons flow from the hot side to the cold side. They will interact with the electrons and a net momentum is transferred to the electrons. The electrons gain this momentum, and flow in the sample along the temperature gradient direction.[1] The phonon-drag gains importance at temperatures lower than the Debye temperature (θ_D), where the electron-phonon interactions become more important than the phonon-phonon interaction.[2]

One can summarize the basic thermopower effects in the following phenomenological equations[3]

$$\mathbf{E} = \rho\mathbf{j} + S\boldsymbol{\nabla}T \qquad \mathbf{j} = \sigma\mathbf{E} + \epsilon\boldsymbol{\nabla}T \qquad S = -\rho\epsilon \tag{1.2}$$

$$\mathbf{Q} = \Pi\mathbf{j} - \kappa\boldsymbol{\nabla}T \tag{1.3}$$

$$\Pi = ST \tag{1.4}$$

where S is the Seebeck coefficient, Π is the Peltier coefficient, κ is the heat conductivity, σ is the electric conductivity, ρ is the electric resistivity, $\boldsymbol{\nabla}T$ is the temperature gradient, $\mathbf{Q}$ is the heat, $\mathbf{E}$ is electric field, $\mathbf{j}$ is the electric current and ϵ is a thermoelectric coefficient.

Nowadays, the SE and its inverse effect, the Peltier effect (PE), are widely used to satisfy different quotidian needs. For instance, cooling down small volumes in portable fridges. One advantage of using thermoelectric methods is that they don't produce noise. Additionally, they don't contain any liquid or gas like the traditional fridges and can be easily converted in a heat pump by inverting the current. Nevertheless, they are not as energetically efficient as the traditional fridges. Another important application is thermoelectric generators, where the drawback is again the low energetic efficiency. However, they can be used in cars or other environments, where it is important to optimize the energetic efficiency by reusing the residual heat.

Spincaloritronics is an emergent field. This field refers to the phenomena which combines spin currents, heat currents and magnetism. The different effects included in this issue can help to deal with the generated ohmic heat in electronic devices and can also contribute to the increase in data storage speed. An equivalent effect to the SE has been observed in the framework of caloritronics

Due to its similarities with the SE, in spin caloritronics, this effect is called Spin Seebeck Effect (SSE). The SSE can be split in two different effects depending on the source of the effect. The "direct" and the "magnon driven" SSE.

On "direct" SSE, the role of a junction made of two different metals is taken by the spin channels. It is considered that each spin channel has its

own S. Therefore, the same reasoning which is used to explain the regular SE was proposed to hold to the *"direct"* SSE. The *"magnon driven"* SSE was reported for the first time in 2008 on a bilayer system by Uchida et al.[4] In their experiment the system was composed by a non-ferromagnetic metal layer on top of a ferromagnetic layer. Magnons are thermally activated in the ferromagnetic layer and they lose torque in the interface with the non-ferromagnetic layer injecting a spin current. This spin current can be converted into a charge current through the inverse Spin Hall effect. Since the effect is related with magnon propagation, any magnetic material with a low Gilbert damping constant is a good candidate. For this purpose permalloy was considered an appropriate choice.

The thesis is structured as follows:

Chapter 2. It is discussed the origin of ferromagnetism and half-ferromagnetism. It is also treated factors which can influence this behavior.

Chapter 3. Different concepts are presented to properly understand the topics treated.

Chapter 4. I explain the general experimental procedures which I follow to characterize the samples, independently of the topic treated. Furthermore, the characterization of the crystalline structure of the Heusler compounds and its evolution is also presented.

Chapter 5. The role of defects and disorder on AHE is studied. I also present a possible data treatment which can be used to separate the intrinsic and the extrinsic contributions to the AHE.

Chapter 6. The potential application of Co_2MnAl to make magnetic field sensors based on this material is explored.

Chapter 7. It is presented and analyzed the data from MOKE ellipsometry. This results from cooperation between the "Technische Universität Kaiserslautern" with the "Johannes Gutenberg-Universität Mainz".

Chapter 8. I show the experimental setups constructed to perform the measurements. The different challenges which arise from the experimental geometry and the material chosen are explained. Furthermore, preliminary results and the current state of this research are also presented.

Chapter 9. In this final chapter the most important findings are reviewed.

Chapter 2

Materials

Heusler compounds and permalloys were selected to perform the different studies. In the current chapter, general properties of these metallic compounds like ferromagnetic and half-ferromagnetic behavior are described in detail. In addition, the source of interesting magnetic properties is discussed. Finally, the most relevant properties of the different compounds used ($Ni_{80}Fe_{20}$, $Co_2FeSi_{0.6}Al_{0.4}$, $Co_2FeGa_{0.5}Ge_{0.5}$ and Co_2MnAl) are described.

2.1 Ferromagnetic materials

2.1.1 Origin of the ferromagnetism

Ferromagnetism refers to the presence of a total magnetic moment (spontaneous magnetization) in some solids without the need of an external applied magnetic field. This effect rises mainly from magnetic interactions. Therefore, the deepest level of a description must involve the electron-electron interaction. The Heisenberg model is used to describe these interactions. Nevertheless, it is important to remark that this model is working properly only in the atomic or molecular scale.

In order to clarify the electron-electron interaction described by the Heisenberg model a short derivation of it is presented. The following reasoning is a compilation from different sources.[2,5,6]

One considers a two electron system in a quantum mechanical framework, where the two electrons can not be distinguished from each other. Therefore, $\phi(\boldsymbol{r_1}, \boldsymbol{r_2}) = \phi(\boldsymbol{r_2}, \boldsymbol{r_1})$ must be a solution of the time independent Schrödinger equation with the same eigenvalue. In the non degenerate case, the difference between $\phi(\boldsymbol{r_1}, \boldsymbol{r_2})$ and $\phi(\boldsymbol{r_2}, \boldsymbol{r_1})$ can only be a multiplicative constant $\lambda = \pm 1$ ($+$ symmetric and $-$ antisymmetric). The last consideration also

applies for a degenerate case. If the spin is introduced in a function, which depends on the spatial coordinates and the spin is a free parameter, the wave function $\Psi(\boldsymbol{r_1}, \boldsymbol{s_1}; \boldsymbol{r_2}, \boldsymbol{s_2})$ can be written as a product of two functions, $\phi(\boldsymbol{r_1}, \boldsymbol{r_2})\chi(\boldsymbol{s_1}, \boldsymbol{s_2})$. By considering all the possible spin orientations four possibilities for χ arise. Three of them are symmetric (triplet state with total spin S = 1) and one antisymmetric (singlet state with total spin S = 0). Finally, if the lowest eigenvalue E_s (E_t) is associated with the singlet (triplet), the total spin of the ground state will depend on E_s-E_t, i.e. whether the spin alignment is parallel (ferromagnet) or antiparallel (antiferromagnet).

The Heisenberg model can be extended to systems with many atoms/ions. In this case, the model assumes that each atom/ion is located in a fixed position in a lattice and close together. However, the atoms are located far enough apart such that any excitation energy is higher than the splitting of the degenerate ground states. Finally, if one writes $J_{ex} = E_s - E_t$, where J_{ex} (J_{ij}) is the exchange interaction energy, it is possible to introduce the spin-Hamiltonian operator like[2,7,8]

$$\mathcal{H}^{spin} = -2\sum_{i>j} J_{ij}\mathbf{S_i}\mathbf{S_j}. \tag{2.1}$$

Note that $\mathcal{H}^{spin}$[1] is dependent on the relative spin orientation and no spatial direction is considered. Typically, extended ferromagnets present anisotropic properties (magnetic domains, domain walls, etc...). In order to break the rotational symmetry, dipolar interactions and spin-orbit coupling have to be considered.

Micromagnetic approximation shifts to a larger scale by considering the average over the individual magnetic moments. Due to the averaging, it needs a continuous vector field to describe the magnetization $\mathbf{M}$. In principle, the vector $\mathbf{M}$ can point in any direction which may change in time. Nevertheless, the modulus of this vector is everywhere $|\mathbf{M}|$=M_s. The magnetization saturation M_s refers to the density of magnetic moments and is a quantity widely used to characterize ferromagnetic solids.

Due to the different magnetic anisotropies, it usually costs less (more) energy to align $\mathbf{M}$ along one specific direction, which is so-called easy (hard) magnetic axis. Magnetocrystalline and shape anisotropies are the two main sources of anisotropies which finally lead to the presence of the magnetic axis measured.

[1] In this thesis, it is followed the notation presented by N. W. Ashcroft and N. D. Mermin.[2] In this notation $\mathbf{S}^2 = (\mathbf{S}_1 + \mathbf{S}_2)^2 = \frac{3}{2} + 2\mathbf{S_1} \cdot \boldsymbol{S_2}$ and a factor $1/\hbar^2$ is missing in the Heisenberg Hamiltonian.

In summary, the direction of **M** is determined by the different anisotropies and the modulus of **M** (M_s) is roughly driven by the exchange energy.

2.1.2 Magnetocrystalline anisotropy

The magnetocrystalline anisotropy arises from the crystalline structure of the solid. Through spin-orbit interaction, the spins of the electrons couple with the lattice. In consequence, **M** is aligned along a certain crystallographic direction which relates to a lower energy. The energy of the anisotropy is described by a phenomenological expression, which is a function of the particular crystalline structure studied. Power expansion series are typically used to write such expressions, where the coefficients are taken from experiments.

E.g. hexagonal lattice which is energetically symmetric in the crystallographic a-b-plane.[8] Therefore, the anisotropy energy (E_{an}) has to be a function of the angle θ between the c-axis and the magnetization direction (uniaxial anisotropy)[2].

$$E_{an} = -K_1 cos^2\theta + K_2 cos^4\theta = -K_1 m_z^2 + K_2 m_z^4, \tag{2.2}$$

$$E_{an} = -K_1'(1 - m_z^2) + K_2'(1 - m_z^2)^2. \tag{2.3}$$

The equations (2.2) and (2.3) are equivalent and their use in literature depends on the author. K_1 (K_1') and K_2 (K_2') are experimental constants, which are functions of the temperature. The subindex z represents an axis parallel to the crystallographic c-axis and $\mathbf{m}=\frac{\mathbf{M}}{|\mathbf{M}|}$. Experimentally it is found that for all ferromagnets the coefficients of the equation (2.2) have a value $|K_1| \gg |K_2|$. In general, the second order term for uniaxial anisotropy is negligible. The difference between (2.2) and (2.3) is a constant energy which means a shift in the zero energy and it does not carry physical relevance.

For cubic anisotropy, the parameters K_1 and K_2 might also be determined from experiments, but in this case, both are necessary. However, no further terms need to be considered

$$E_{an} = -K_1(m_x^2 m_y^2 + m_y^2 m_z^2 + m_z^2 m_x^2) + K_2 m_x^2 m_y^2 m_z^2. \tag{2.4}$$

In case of iron (nickel), the magnetic easy axis is following the (100) ((111)) direction.

[2]The notation presented on the equations (2.2), (2.3) and (2.4) follows the one introduced in different books.[8,9]

2.1.3 Shape anisotropy

The concrete shape of a particle can lead into a magnetic anisotropy. The origin is the dipole interaction. This is a long range interaction and it's approximately four orders of magnitude weaker than the exchange interaction.[10]

Firstly, if it is considered an uniformly magnetized spherical particle. The resulting magnetic field is a dipole (Fig. 2.1 a). In addition, an internal demagnetization field ($\mathbf{H_D}$) with opposite direction to $\mathbf{M}$ appears (Fig. 2.1 b). $\mathbf{H_D}$=-$\hat{N}_D\mathbf{M}$, where $\hat{N}_D$ is the internal demagnetization tensor.[11,12]

In the simplest case, ellipsoidal particles are considered (figure 2.1). When the magnetization is aligned along one of the principal axes of the ellipsoid, the tensor becomes diagonalizable and $N_{Dxx}+N_{Dyy}+N_{Dzz}=1$.[13,14]

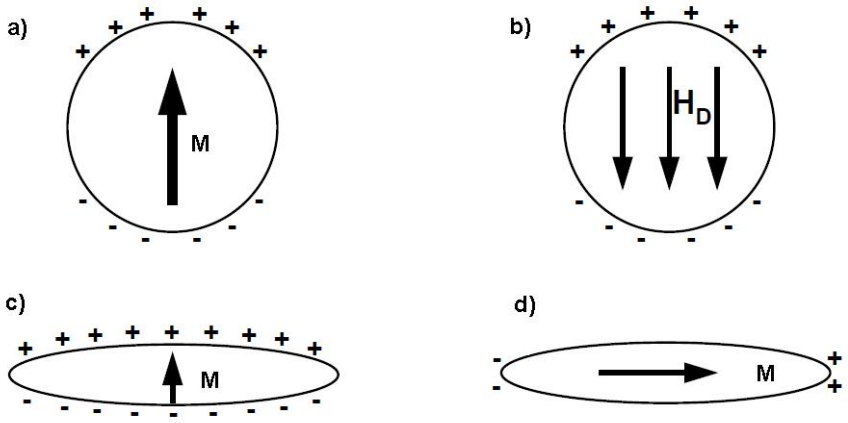

Figure 2.1: a), c) and d) surface charge distribution depending on the magnetization direction. b) Demagnetization field vector in relation to the charge distribution.[11]

The sphere is the isotropic shape case. Therefore, it is necessary to consider an elongated ferromagnetic particle (Fig. 2.1 c) and d)). On such particles, the equivalent magnetic charge distribution on the surface depends differently on the direction of $\mathbf{M}$. This asymmetry leads into a lower magnetization energy if $\mathbf{M}$ is parallel to the long axis (Fig. 2.1 d)). In order to switch the magnetization direction, a magnetic field $\mathbf{H}$=-(N_{Dp}-N_{Dl})$\mathbf{M}$ must be applied, where the sub-index Dp refers to the perpendicular direction to long side of the particle and Dl refers to the long direction of the particle.

2.1.4 Permalloys: General remarks

First experiments performed by the Bell System laboratory on nickel-iron alloys showed extraordinary magnetic properties.[15] In the next years, studies on the crystal structure of such alloys have shown a transition from the characteristic iron bcc crystal structure to a nickel fcc arrangement, while the nickel content was increased to a proportion higher than 25 %.[16]

In particular, the alloys with an approximate content of 80 % of nickel and 20 % of iron are ferromagnets with a high permeability, low coercivity, and small magnetic anisotropy. These alloys are so-called *permalloys*.

Epitaxial thin films of $Ni_{79}Fe_{21}$ have been grown on Si (111) with a high crystal quality.[17] In this former work, they also report a maximum in-plane coercivity of 2,64 Oe and 20 Oe for samples deposited on (111) and (100) substrates, respectively. Despite the large mismatch between MgO (a = 0,42 nm) and $Ni_{80}Fe_{20}$ (a = 0,35 nm), it was also reported epitaxial growth on this substrate.[18]

Annealing temperature has shown to be a relevant parameter to tune the surface morphology of the thin films[19] and their other properties (e.g. coercivity, electrical resistivity and relative permeability).[20]

The permalloys can be applied in many fields. Spin valve devices[21,22] or patterned recording media[23] are some possible applications.

2.2 Half-metallic ferromagnets: Heusler compounds

Heusler compounds are widely investigated since Heusler found an extraordinary ferromagnetic behavior in some compounds made of nonmagnetic elements.[24] Depending on their generic chemical formula, X_2YZ or XYZ, they are commonly labeled as Heusler or *half*-Heusler compounds, respectively. These ternary magnetic compounds contain two different transition metals on their X and Y positions and one sp metal on the Z position. In a fully ordered state, the Heusler compounds crystallize in a $L2_1$ phase and in a $C1_b$ phase in *half*-Heusler compounds. These lattices consist of four interpenetrating fcc sublattices. There is a X atom located at (0,0,0) and a X (void) atom at the $(\frac{1}{2},\frac{1}{2},\frac{1}{2})$ position for $L2_1$ ($C1_b$) crystal structure. The Y atom lies at $(\frac{1}{4},\frac{1}{4},\frac{1}{4})$ and the Z atom at $(\frac{3}{4},\frac{3}{4},\frac{3}{4})$ for both crystal structures.

The half-metallic behavior is a remarkable property, which arises from the electronic configuration of some of those compounds. This property refers to the fact that the majority spin electrons are metallic and the minority spin electrons are semiconducting. Therefore, the ones which are half-metallic

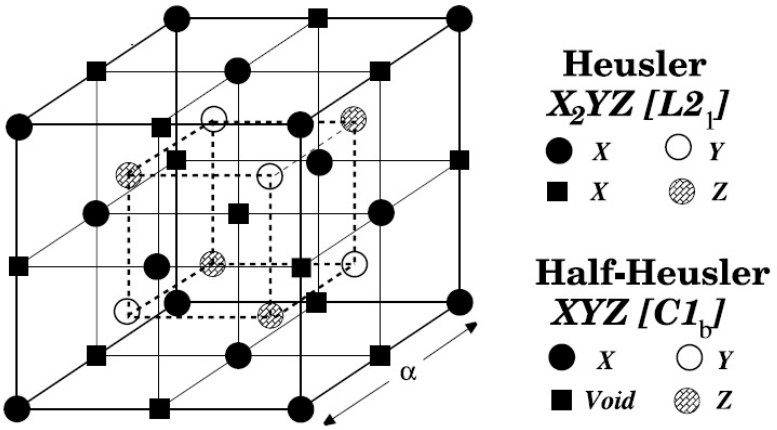

Figure 2.2: Schematic representation of the $C1_b$ and $L2_1$ crystalline structure.[25]

ferromagnetic can present ideally up to 100 % spin polarization at the Fermi energy. De Groot et al.[26] studied different half-Heusler compounds. For the first time, they predicted, the half-metallic behavior for some half-Heusler compounds, like NiMnSb and PtMnSb. In the course of time, the half-metallic ferromagnetic behavior has been predicted on different half- and Heusler compounds.

In addition, cobalt based Heusler compounds (Co_2YZ) present a high Curie temperature (T_c). Therefore, the half-metallicity predicted for some of these compounds and their characteristic high T_c values are making them promising candidates for many applications.[27–30]

2.2.1 Electronic and magnetic properties of Heusler compounds

In the current section, the discussion will focus on the prototypic case of Co_2MnZ. Note that the different studies presented in this thesis were performed using cobalt based Heusler compounds with Y = Mn or Fe. However, the difference of Mn and Fe is just one valence electron and the discussion can be straight forward extended to Co_2FeZ compounds.

Origin of the band gap

In the $L2_1$ structure each Mn or Z atom has eight Co atoms as first neighbour. Whereas a Co atom has four Mn or Z atoms as a first neighbour. The

surrounding Co atoms of different sublattices show the same surrounding, only rotated by 90°, which makes them chemically equivalent. The band gap is mainly controlled by the hybridization of the d orbitals of cobalt.[25]

The molecular orbitals can be described as following: First, the 5-d orbitals of Co bond with the 5-d orbitals of the other Co atom. This results in 5-d bonding orbitals and 5-d antibonding orbitals. Then the 5-d bonding orbitals of Co-Co hybridize with the 5-d orbitals of Mn, which results in 5-d bonding orbitals and 5-d antibonding orbitals plus 5-d antibonding orbitals. The antibonding ones can not hybridize with any d-orbital of Mn. In consequence, the (Co-Co)-Mn bonding and the three Co-Co antibonding orbitals, which are lying below of the Fermi energy, are fully occupied. In the spin down band structure, the seven hybridized d-orbitals above the Fermi energy are unoccupied for Z = Ge.[31]

The Z or sp atom does not participate in the formation of the gap. Although, it opens the possibility to tune the magnetic features which is also an interesting property for applications. The Z atom contributes with four sp bands but only contributes with n electrons. Consequently, m = 8-n electrons must to be taken from the d orbitals. In the case of Z = Al or Ga n = 3 and for Z = Si or Ge n = 4.

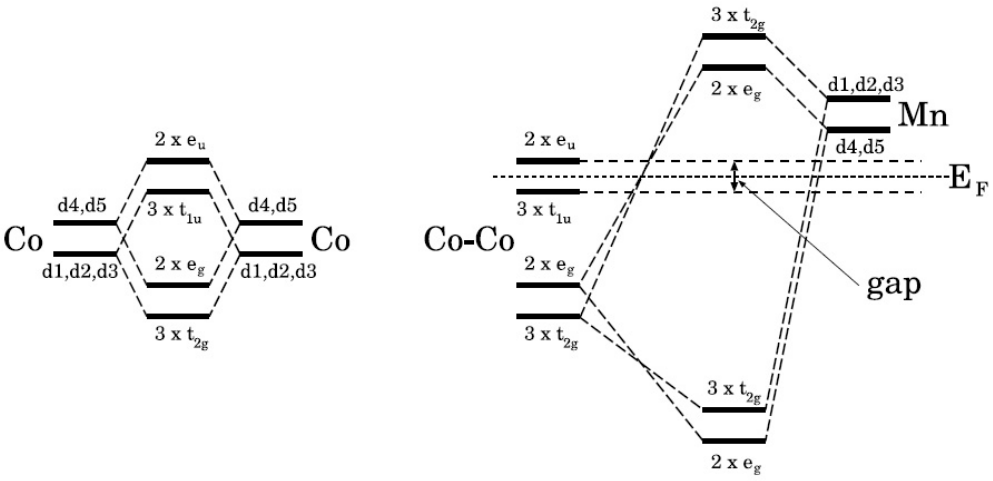

Figure 2.3: The orbitals d_{xy}, d_{yz} and d_{zx} are represented by d1, d2 and d3. The d_{z^2} and $d_{x^2-y^2}$ are represented by d4, d5. The coefficient on the hybrid orbitals gives the degeneracy. Left: Sketch of Co-Co orbitals hybridization. Right: Sketch of (Co-Co)-Mn orbital hybridization for spin down minority electrons.[25]

Notice that the former discussion assumes fully ordered $L2_1$ crystal struc-

ture. Unfortunately, in real crystals, one usually finds defects and impurities. The presence of DO_3 (Co-Y atoms randomly exchanged) breaks the half-metallic configuration by introducing in-gap states from the non bonded antibonding states of Co atoms sited in Y position. The B2 phase (Y,Z atoms are randomly exchanged) can also reduce the spin polarization. In some cases, however, it has a weak influence, e.g. Co_2CrAl.[32] The A2 phase (Co,Y,Z atoms are randomly exchanged) results in an arbitrary electronic configuration, which gives no reason to suspect high spin polarization.

Besides the structural consideration, recent works[33,34] have shown that the influence of the spin-orbit coupling can introduce in-gap states through spin-flip scattering of the majority states. Co_2MnSi and Co_2MnGe reduce their full spin polarization by 3 % and 1 % respectively.[35] Furthermore, effects of finite temperature have to be considered, like magnon excitation, changes in lattice parameter and the introduction of defects,[36] which will also lead to a reduction of the spin polarization.

Magnetic properties

The magnetization saturation M_s of the 3-d elements and their alloys is related with the valence electrons.[37,38] The magnetic moment per atom can be calculated by M_s=$N^{\uparrow}$-$N^{\downarrow}$ in μ_B/f.u. Where $N^{\uparrow}$ and $N^{\downarrow}$ represent the number of electrons per atom with spin-up and spin-down, respectively. Whereas, the valence number of electrons is given by Z=$N^{\uparrow}$+$N^{\downarrow}$. In case of Heusler compounds, it is convenient to describe the M_s behavior like:

$$M_s = Z - 2 \times N^{\downarrow}. \tag{2.5}$$

$N^{\downarrow}$ can be calculated easily considering figure 2.3. The spin-down electrons are in fully occupied bands located below the Fermi energy. These are, 8 d-like bands ($3\times t_{1u}$, $3\times t_{2g}$ and $2\times e_g$), 3 p-like bands and 1 s-like band. Thus, one obtaines $N^{\downarrow}$=12. The linear relation between M_s and Z is widely known as the Slater-Pauling behavior (Fig. 2.4).

Notice that the Slater-Pauling behavior results in integer numbers of M_s for each X_2YZ half-ferromagnetic Heusler compound. However, this behavior is no longer followed by compounds that have two different elements on the Y or Z position. For instance, $Co_2YZ1_xZ2_{x-1}$, where Z1 and Z2 are two different sp atoms occupying the Z position. Such a compounds have a fractional value of M_s.

In a context of material engineering, one can infer from figure 2.3 that the theoretical limit of the M_s for Heusler compounds is $7\mu_B$/f.u. (spin-up electrons occupying 7 d-like orbitals above the Fermi energy).[31]

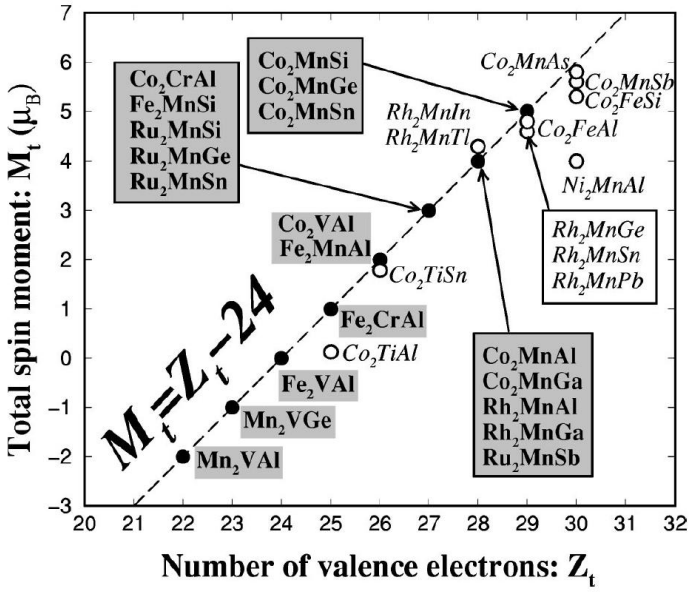

Figure 2.4: Full (open) circles represent elements, which follow (do not follow) the Slater-Pauling behavior. The dashed line is the magnetization saturation predicted by the equation in the plot.[31]

The measurement of the saturation magnetization can be performed by different methods (section 4.2.3) in a short time. However, the measurement of the theoretical value on a sample is not a guarantee for a $L2_1$ structure. Nevertheless, the measurement of values far from the theoretical one is a clear proof of the presence of disorder or defects.

2.2.2 Selected Heusler compounds

$Co_2FeSi_{0.6}Al_{0.4}$ and $Co_2FeGa_{0.5}Ge_{0.5}$

In order to deal with the effects of the defects and temperature, the electronic configuration has to be engineered appropriately. For this purpose, series of quaternary alloys have been investigated. In this series, the concentration of two components is fixed. Typically, the concentration of the other two compounds is tuned simultaneously. It is assigned a value x to the concentration of one compound and $1 - x$ to the other one. Then the value of x is progressively increased. In the $Co_2Cr_{1-x}Fe_xAl$ series it is challenging to grow the alloy in a $L2_1$ phase. The B2 phase of this compound destroys its half-metallic behavior.[39] In $Co_2Mn_{1-x}Fe_xSi$ series the width of the gap

marginally decreases while x is increased. The Fermi energy can be seen to shift within the minority gap. It moves from the top of the minority valence band (Co_2MnSi) to the bottom of the minority conduction band (Co_2FeSi). The most stable half metallic behavior is found for x = 0.5. In this configuration the Fermi energy lies in the middle of the minority band gap.[40] Finally, a TMR ratio of 175 % at room temperature has been reported for $Co_2FeSi_{1-x}Al_x$ with x = 0.5.[41]

Recently, calculations of the electronic structure of $Co_2FeSi_{1-x}Al_x$ with different x were performed by using LDA+U approximation.[42] In them, it is also possible to observe a continuous shift (from bottom to top) of the Fermi energy in the gap while the Aluminum content is increased (Fig. 2.5 a)). In addition, the influence of disorder must be considered. As a result, the most promising candidates for applications and the most robust against disorder have an aluminum content of $0.25 \leq x \leq 0.75$. (Fig. 2.5 b) & c)).

The density of states for $Co_2FeGa_{0.5}Ge_{0.5}$ is not published in literature. The parent compound Co_2FeGe was predicted as a true half-metal but Co_2FeGa was not. As it is shown in figure 2.5 a), it is expected that the Fermi energy for $Co_2FeGa_{0.5}Ge_{0.5}$ behaves like in the $Co_2FeSi_{1-x}Al_x$ and $Co_2Mn_{1-x}Fe_xSi$ cases. Therefore the Fermi energy should lie at the bottom of the spin-down band gap. In consequence, smaller amounts of disorder may destroy the half-metallic behavior, introducing electrons from the spin-down channel. The resulting change in the topology of the Fermi surface should modify its properties. Thus the spectrum of the magnonic excitations would also change, leading to a different strength of the skew scattering contribution.

Co_2MnAl

As it was shown in the former section, Heusler compounds should present 100 % of atomic ordering for $L2_1$ phase. Progressive increases of defects tend to reduce the spin polarization. However, Co_2MnAl is not following this general behavior. It presents 15 % of spin polarization for the $L2_1$ phase and 76 % for the B2 phase.[45] Therefore, it is not a true half-metallic ferromagnet. Nevertheless, Co_2MnAl is a good candidate for spintronic applications, because it still offers a large value of spin polarization in a B2 phase, which is easier to obtain than a $L2_1$ ordered phase by depositing or annealing the samples at lower temperatures.[46] Moreover, the Giant Hall effect was reported on Co_2MnAl.[47] This fact triggered the research on this compound. In addition its viability as a Hall sensor was explored.

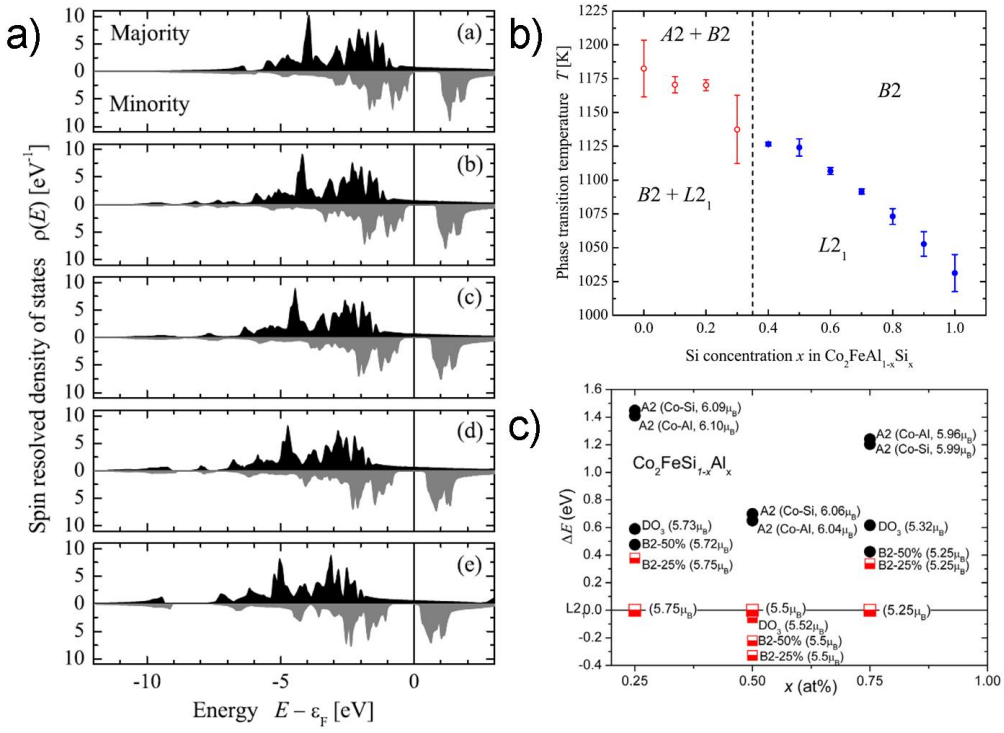

Figure 2.5: a). Spin resolved density of states of $Co_2FeAl_{1-x}Si_x$ calculated using LDA+U with x = 0, 0.25, 0.5, 0.75 and 1.[42] b) Transition temperature, Blue (Red) indicates single (coexistence) phase.[43] c) Influence of disorder on the spin polarization (P), filled (half-filled) circle (square) represents P<1 (P=1).[44]

Chapter 3

Theoretical background

3.1 Hall-like effects

In a first approach to the Hall effect or ordinary hall effect (OHE), one can consider a rectangular conductor or semiconductor in isothermal conditions. If it is applied a magnetic field $\mathbf{H}$ and a current $\mathbf{j}$ (figure 3.1), then electrons will feel a force $\mathbf{F_m} = -q \cdot (\mathbf{v} \times \mu_0 \mathbf{H})$. The consequence of this situation is an excess of negative charges in one side and a deficit in the other side. The charge distribution will lead into a difference of potential V_{Hall}.

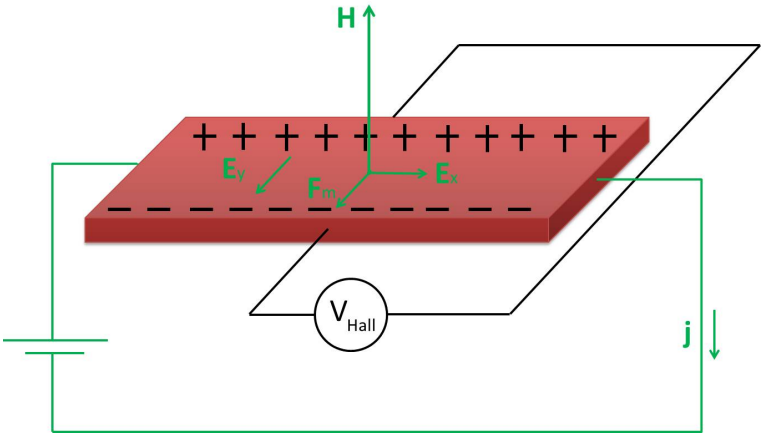

Figure 3.1: Ordinary Hall effect geometry.

By contacting appropriately the sample described on figure 3.1, it is possible to measure the Hall voltage V_{Hall}. There are many effects with an experimental geometry similar to the OHE, because of this, they might be called Hall-like effects. Some examples are the Nernst effect and the spin

Hall effect. For the Nernst effect, the Nernst voltage is transversal to a temperature gradient and **H**. Due to the spin-orbit interaction, in the spin Hall effect, a spin-up (-down) current propagates to "left" ("right"). The current is transversal to the applied electric field and leads to a spin accumulation at the opposite edges of the sample.

It is is particularly interesting to study the Hall effect in materials like ferromagnets because it behaves anomalously. In such materials, instead of the monotonic increase of the Hall voltage while the magnetic field **H** raises, on the Hall voltage is observed a rapid linear increment of the its value by setting higher values of **H**. When the material reaches the value of M_s, the initial behavior is followed by a strong reduction of the slope (V_{Hall} against **H**).

The anomalous and the spin Hall effect can not be understood by using classic theory. Before going into detail on the theoretical aspects regarding to these Hall-like effects, it is convenient to describe briefly the OHE by using semiclassical approximation[1].

3.1.1 Ordinary Hall effect (OHE)

Based the on Drude model, the study starts on the motion of an electric charge located in a x-y plane. Then, an electric field **E** is applied in an arbitrary direction of the plane and a magnetic field **H** is applied in the z direction, perpendicular to the x-y plane. Consequently it is possible to extract:

$$\sigma_0 E_x = \omega_c \tau j_y + j_x, \tag{3.1}$$

$$\sigma_0 E_y = \omega_c \tau j_x + j_y, \tag{3.2}$$

where σ_0 is the conductivity, ω_c is the cyclotron frequency, τ is the average relaxation time and j is the current density in x or y direction. Depending on the value of $\omega_c\tau$, the OHE is divided in three regions: low, high and intermediate field region. The low field region, for $\omega_c\tau \ll 1$, where the time between collisions does not allow to complete a cyclotron orbit. This condition is usually valid at high temperatures or in samples with an important content of defects, like in the case treated in the present thesis. On such conditions it is important to remark that in general, the influence of the topological features of the Fermi surface are negligible. The high field region is for $\omega_c\tau \gg 1$. In this case, the electron can describe several orbits and an extremely pure

[1]The OHE description follows the reasoning presented in different sources.[2,48]

crystal and low temperatures are required to achieve this region. Finally, the intermediate field region, $\omega_c\tau \approx 1$, which is a transition between the previous conditions.

To reach further understanding about this phenomena, it is convenient to consider the semiclassical approach. In this model, a band structure is supposed to be known, i.e., the model associates to each electron in a certain band n and a position $\mathbf{r}$, a wave vector $\mathbf{k}$ and a function $\varepsilon_n(\mathbf{k})$. Furthermore, there is no interband transition and the motion of an electron in such a system, under an applied $\mathbf{E}$ and $\mathbf{H}$, is calculated by[2]

$$\mathbf{v}_n(\mathbf{k}) = \frac{1}{\hbar}\frac{\partial\varepsilon_n(\mathbf{k})}{\partial\mathbf{k}}, \tag{3.3}$$

$$\hbar\,\dot{\mathbf{k}} = -e\left[\mathbf{E}(\mathbf{r},t) + \mathbf{v}_n(\mathbf{k}) \times \mu_0\mathbf{H}(\mathbf{r},t)\right]. \tag{3.4}$$

In order to get a description of the OHE within these boundary conditions, one has to start considering the contribution of H. Furthermore, the problem is still too complex and has to be restricted to the high field region and it is assumed that the electron has the Fermi energy $\varepsilon_n(\mathbf{k}) = \varepsilon_f(\mathbf{k})$ and a momentum $\hbar\mathbf{k}$. Then, the presence of $\mathbf{H}$ will not change the energy of the electron and it will describe a cyclotron orbit in the real and momentum space. In the momentum space, the orbit can be evaluated from considering the intersection of the Fermi surface with a plane normal to $\mathbf{H}$. This intersection gives an area of constant energy.

Finally, by applying an electric field E_x in the defined x-y plane, the electron will feel a Lorentz force $\mu_0 e v_{nx} H$ and the constant energy area is perturbed. As result, the area enclosed by the electron orbit is not longer a constant energy surface. The energy deviation from the Fermi surface and the increment of $\mathbf{k}$ can be calculated by[48]

$$\Delta\varepsilon = \varepsilon - \varepsilon_f = \hbar\frac{E_x}{\mu_0 H}k_y + const, \tag{3.5}$$

$$\Delta k_y = \frac{\Delta\varepsilon}{\hbar v_{ny}} \qquad \Delta k_x = \frac{\Delta\varepsilon}{\hbar v_{nx}}. \tag{3.6}$$

Therefore, the electric field E_x is perturbing the orbit in real space and displacing the Fermi surface in the momentum space. In consequence, it is also possible to correlate a displacement of the Fermi surface in the momentum space with a net electric current.

3.1.2 Nernst effect

The Nernst effect is, in essence, the OHE in which the current flow is substituted by a heat flow. Therefore, it is only necessary to study the influence of a temperature gradient in a conductor and join the result with the former discussion.

In the presence of a temperature gradient, the current flow can be written like in equation (1.2). In order to present a complete description of the phenomena, it is convenient to substitute the coefficients by the appropriate tensors, resulting in[49]

$$\mathbf{J} = \bar{\sigma}\mathbf{E} - \bar{\alpha}\boldsymbol{\nabla}T, \tag{3.7}$$

where $\bar{\sigma}$ is the conductivity tensor, $\bar{\alpha}$ is the thermoelectric conductivity tensor and ∇T is the temperature gradient. One should consider that in the Nernst effect there is no charge current, thereby the former equation has to be expressed like:

$$\mathbf{E} = \bar{\sigma}^{-1}\bar{\alpha}\boldsymbol{\nabla}T. \tag{3.8}$$

Once this point is reached, the discussion presented above is straight forward continued. By solving the Boltzman equation for a Fermi gas in the relaxation time approximation,[50] it is possible to find a relation between the off-diagonal term of the conductivity and the thermoelectric tensor

$$\alpha_{xy} = \frac{\pi^2}{3}\frac{k_B^2 T}{e}\frac{\partial\sigma_{xy}}{\partial\varepsilon}\bigg|_{\varepsilon=\mu}, \tag{3.9}$$

where k_B is the Boltzman constant and e is the electric charge of an electron. In conventional metals, the chemical potential is $\mu \approx \varepsilon_f$ close to the Fermi energy. Therefore, equation (3.9) is useful to understand the Nernst effect in terms of infinitesimal shifts in the chemical potential.

3.1.3 Spin Hall effect (SHE)

The discussion presented in section 3.1.1 might help to explore other Hall-like systems configuration as Spin Hall effect. This phenomena is still not well understood. Even its division into intrinsic and extrinsic contributions remains a source of controversy. S. Zhang and Z. Yang predict an exact cancellation of the intrinsic spin Hall current by spin torque, which make only the extrinsic contributions relevant.[51] However, recent experiments support the idea of a non-vanishing intrinsic contribution.[52,53] Therefore, it is convenient to present a brief discussion of the SHE in terms of intrinsic and extrinsic contributions.

To describe the intrinsic source, one has to consider a 2D electron gas system under the Rashba effect and then, the influence of an electric field **E** in a certain direction on such a system. The Rashba effect consists in spin-splitting of the electronic band structure without the presence of a magnetic field **H**, in systems with broken inversion symmetry. These systems are described by the Hamiltonian:[54]

$$\mathbf{H} = \frac{(\hbar \mathbf{k})^2}{2m} + \alpha_R(\mathbf{z} \times \mathbf{k})\vec{\sigma}, \tag{3.10}$$

where α_R is the Rashba constant, $\vec{\sigma}$ is the Pauli matrix and m is the effective mass of the electron. The origin of the splitting lies in the defined momentum of the electronic eigenstates and due to the spin-orbit coupling, it appears a momentum-dependent effective magnetic field which aligns the spins perpendicular to the momentum[55] (Fig.3.2).

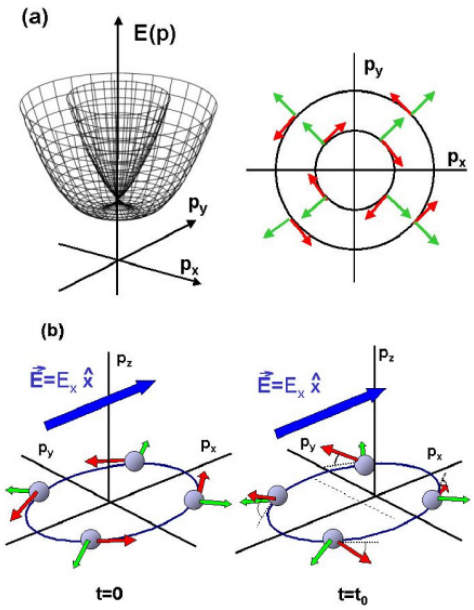

Figure 3.2: (a) Representation of the 2D electron gas eigenstate under Rashba effect. Green arrows represent momentum and the red ones label the eigenspinors. (b) Sketch of the displacement of the Fermi surface in the presence of an electric field in a time t_0 shorter than the average scattering time. Figure taken from reference.[55]

In this proposed system, the consequence of applying an electric field in the x direction is a displacement of the Fermi surface, which in this case is an amount $\mid eE_x t_0/\hbar \mid$, considering a time lower than the average scattering

time. While the Fermi surface is displaced in the momentum space, it is induced an effective torque over the electrons which tilts the spins of the electrons. This HE-like mechanism creates a spin current in the y direction. In addition to intrinsic mechanisms, one has also to consider the extrinsic contributions.

The extrinsic mechanisms are mainly coming from the asymmetric scattering events. If one considers a slab and an apply current j in a direction parallel to the plane defined by the slab, then the electrons which carry charge and spin, not only follow the direction of j, they also will be deflected, by impurities and defects. Due to the spin-orbit coupling, it happens preferentially in a direction transversal to the slab plane, depending on the carried spin.[56] This mechanism is so-called skew scattering and it will also play a significant role on the Anomalous Hall effect.

The SHE has interesting applications, since it allows to create a spin current out of a charge current. Also its inverse effect (ISHE) is interesting to perform research in any field which requires spin current detection because by the ISHE it is possible to convert a net spin flow into a charge current which is possible to measure. This last property will be exploited during the investigation on the Spin Seebeck effect.

3.1.4 Anomalous Hall effect (AHE)

From a general point of view, the Hall effect can be divided into two parts, $\rho_{xy} = R_H B + \rho_{xy}^{AHE}$, where R_H is the ordinary Hall coefficient and ρ_{xy}^{AHE} is the anomalous Hall resistivity. The ordinary Hall effect has been already discussed above. More interesting are the AHE contributions induced by the symmetry-breaking effect of the magnetization leading to transversal currents at zero magnetic field. From a theoretical point of view ρ_{xy}^{AHE} encodes several effects and it is possible to decompose it like:[57]

$$\rho_{xy}^{AHE} = \rho_{xy}^{IAHE} + \rho_{xy}^{AHE-skew} + \rho_{xy}^{AHE-jump}, \tag{3.11}$$

ρ_{xy}^{IAHE} contains the intrinsic anomalous Hall effect (IAHE) contribution to AHE. It depends only on the crystal band structure and can be calculated from the semiclassical transport theory and the anomalous distribution part of the transverse conductivity.[2,58–60] Recently, the introduction of Berry-phase theory provided an explanation, in the framework of semiclassical theory, to the appearance of this spontaneous anomalous Hall current in the presence of an electric field. The Berry-phase theory adds an extra term (anomalous velocity) to the equation (3.3) which in certain conditions turns

out relevant by considering the interband contribution:[61]

$$\mathbf{v}_n(\mathbf{k}) = \frac{1}{\hbar}\boldsymbol{\nabla}\varepsilon_n(\mathbf{k}) - \frac{e}{\hbar}\mathbf{E} \times \boldsymbol{\Omega}_n(\mathbf{k}), \tag{3.12}$$

where $\boldsymbol{\Omega}_n(\mathbf{k})$ is the Berry curvature. In addition to the usual term of the band velocity appears a second one which is transverse to the electric field and it results in a Hall current without magnetic field.

In order to be consistent with the observations, $\boldsymbol{\Omega}_n(\mathbf{k})$ only has to rise with a measurable value under symmetry broken conditions. By considering spatial inversion, $\mathbf{v}_n$, $\mathbf{k}$ and $\mathbf{E}$ will change its sign and the systems which present spatial inversion symmetry will lead into $\boldsymbol{\Omega}_n(-\mathbf{k}) = \boldsymbol{\Omega}_n(\mathbf{k})$. By time reversal symmetry $\mathbf{v}_n$ and $\mathbf{k}$ will change sign but $\mathbf{E}$ stays fixed. Therefore $\boldsymbol{\Omega}_n(-\mathbf{k}) = -\boldsymbol{\Omega}_n(\mathbf{k})$. In consequence, crystalline structures which lead into spatial and time reversal symmetry have a vanishing $\boldsymbol{\Omega}_n(\mathbf{k})$.[61]

The label "intrinsic" is used widely in the literature, since this term does not depend on the scattering rates. Thus it brings in mind the idea of a perfect crystal and the band structure related with it. This idea is justified in metals with a simple band structure, like gold or iron, where the introduction of defects or disorder is not changing appreciably the topology of the Fermi surface. However, in Heusler compounds, the disorder can lead to relevant variations on the topology of the Fermi surface, disorder can induce spin minority states at the Fermi energy. In this sense the so-called "intrinsic" term is no longer intrinsic, because the disorder modifies the topology of the Fermi surface. Therefore ρ_{xy}^{IAHE} is renamed as $\rho_{xy}^{AHE-band}$ in the following.

$\rho_{xy}^{AHE-skew}$ is the contribution from the skew scattering. This term is connected with asymmetric scattering events and the impurity concentration and it is inversely proportional to the transport state lifetime.[62–64] Therefore it is considered as an extrinsic contribution to the AHE. However, such a term being inversely proportional to the relaxation time also arises formally from the Bloch transport theory due to the spin-orbit coupling within a perfect crystal with scalar disorder.[57]

$\rho_{xy}^{AHE-jump}$ is the side-jump contribution and can be understood as a sharp shift in the coordinate system during one scattering event and it is dependent on the scattering potential.[64,65] Unfortunately, $\rho_{xy}^{AHE-jump}$ does not depend on the scattering rate, which makes it impossible to distinguish it from $\rho_{xy}^{AHE-band}$ by the lifetime. That forces to compact equation (3.11) as follows, in order to analyze the data:

$$\rho_{xy}^{AHE} = \rho_{xy}^{AHE-skew} + \rho_{xy}^{AHE-bj}, \tag{3.13}$$

where ρ_{xy}^{AHE-bj} is the anomalous Hall resistivity related with the band structure which contains also the side-jump contribution. In addition, theory

proposes to separate extrinsic and intrinsic contributions due to their dependence on the longitudinal resistivity, which is linear or quadratic, respectively.[62,63,66] In the usual case where $\rho_{xy} \ll \rho_{xx}$ this leads to

$$\rho_{xy}^{AHE} = a\rho_{xx} + \rho_{xx}^2 \qquad \text{with} \qquad \rho_{xy}^{AHE} \approx \sigma_{xy}^{AHE} \cdot \rho_{xx}^2, \tag{3.14}$$

$$\sigma_{xy}^{AHE} = \left(\frac{a}{\rho_{xx}} + b\right) = \sigma_{xy}^{AHE-skew} + \sigma_{xy}^{AHE-bj}. \tag{3.15}$$

$a = \sigma_{xy}^{AHE-skew} \cdot \rho_{xx}$ is the parameter which contains the information about skew scattering, while $b = \sigma_{xy}^{AHE-bj}$ is related to quadratic contributions. This simplification allows to identify the dominant mechanism ($\rho_{xy}^{AHE} \propto \rho_{xx}^n$). Skew scattering is dominant for n = 1 and intrinsic contributions are dominant for n = 2. Alternatively, recent discussions have appeared in which the proportionality is proposed of the conductivities $\sigma_{xy} \propto \sigma_{xx}^{\alpha}$. Depending on the value of the exponent α, three regimes are distinguished: (i) good metal regime with $\sigma^{AHE} \propto \sigma_{xx}^0$, (ii) high conductivity regime with $\sigma^{AHE} \propto \sigma_{xx}^1$, (iii) bad-metal-hopping regime with a scaling law of $\sigma^{AHE} \propto \sigma_{xx}^{1.6-1.8}$. This relation was based on experiments on different thin films.

In following chapters will be shown, how different longitudinal scattering mechanisms influence the data analysis along the lines sketched above. Despite these complications, the AHE can be very useful and provides a valuable tool to generate and control a spin polarized current, which connects this topic with other fields, like spintronics and the spin-Hall effect.

3.1.5 Anisotropic Magnetoresistance (AMR) and Planar Hall effect (PHE)

Typically, ferromagnetic materials present an increase of their resistance up to 1 %,[67,68] while applying a magnetic field. The AMR depends on the angle between the current flow and the magnetization direction in the sample.[69] Commonly, its value is expressed as $(\rho_{\parallel} - \rho_{\perp})/\rho_0$, where $\rho_0 = \frac{1}{3}\rho_{\parallel} + \frac{2}{3}\rho_{\perp}$. In the former equations, $\rho_{\parallel}$ ($\rho_{\perp}$) is the resistivity with the current flowing parallel (perpendicular) to the magnetization vector at saturation.[70] The source of the effect is due to the spin orbit coupling. In case of Ni, it has s and d electrons at the valence band. Due to the spin orbit coupling, it is possible that some electrons from the band up(down)-d mix into the down(up)-d band. Part of the mixing occurs at the Fermi energy. This up-down d mix allows the up-s electrons to scatter into the region where the d electrons are mixed at the Fermi surface. This process would be not possible without the spin orbit interaction, because the up-d electrons are below of the Fermi

energy. Therefore, the scattering process, at the Fermi energy, from the up-s electrons into the up-d electrons is not possible.

The presence of the magnetization introduces an axis in the system which makes the mixing of the d electrons by spin-orbit coupling anisotropic. The consequence of this anisotropy is a resistivity depending on the magnetization direction.[71] In case of Heusler compounds and permalloys, the situation is more complex due to their more complex band structure. Unfortunately, the model can not be straight forward extrapolated. McGuire and Potter contribute to clarify the AMR in permalloys by considering their particular features of the band structure and also contributions from different effects.[72] M. Weiler et al. successfully model the AMR behavior of Co_2FeAl by using the effective macrospin approximation.[73]

In order to describe formally the AMR, the resistivity tensor is written as follow (in a reference system fixed by the magnetization direction)

$$\begin{pmatrix} E_\perp \\ E_\parallel \end{pmatrix} = \begin{pmatrix} \rho_\perp & 0 \\ 0 & \rho_\parallel \end{pmatrix} \cdot \begin{pmatrix} j_\perp \\ j_\parallel \end{pmatrix}. \tag{3.16}$$

In the current case, is convenient to fix the reference system to one side of the used substrates (each lateral side is the x and y direction, respectively). The current is introduced parallel to long axis (x direction) of the substrates. Therefore, the angle α is defined as the angle between the current and the magnetization of the sample. Consequently, the matrix above has to be rotated

$$\begin{pmatrix} E_x \\ E_y \end{pmatrix} = \begin{pmatrix} \rho_\perp \sin^2\alpha + \rho_\parallel \cos^2\alpha & (\rho_\perp - \rho_\parallel)\sin\alpha\cos\alpha \\ -(\rho_\perp - \rho_\parallel)\sin\alpha\cos\alpha & \rho_\perp \cos^2\alpha + \rho_\parallel \sin^2\alpha \end{pmatrix} \cdot \begin{pmatrix} j_x \\ j_y \end{pmatrix}, \tag{3.17}$$

and by taking $j_y = 0$, it is possible to extract[74,75]

$$E_x = j_x\rho_\parallel - j_x(\rho_\parallel - \rho_\perp)\sin^2\alpha, \tag{3.18}$$

$$E_y = j_x(\rho_\parallel - \rho_\perp)\sin\alpha\cos\alpha \quad \rightarrow \quad V_y = \frac{j_x(\rho_\parallel - \rho_\perp)}{t}\sin\alpha\cos\alpha. \tag{3.19}$$

A common experiment in a ferromagnetic thin film with a thickness t is to apply current parallel to one of the side of the film j_x. In addition, a magnetic field is also applied in y direction. Consequently, the magnetization direction forms an angle α with respect to the reference system defined by the film geometry. A voltage V_y, which can be calculated from the equation (3.19),

appears. This transversal voltage to the applied current is widely call Planar Hall effect, due to its experimental similarity with the Hall effect.

The Planar Hall effect is very sensitive to changes of the magnetization direction and it has been used with different goals. To produce magnetic random access memories,[76] to build sensors which can work in the range of nano-Tesla[77] or to study the magnetization in a multilayer system.[78]

3.2 Magnetization dynamics

Up to this point, the motion of the free electrons in the presence of either an applied magnetic or electric field or both at the same time has been discussed. The current section, is focused on the interaction of the time dependent magnetization with a magnetic field. Through it, a consistent description extracted from different sources is also presented.[7–9,79] The magnetization $\mathbf{M}$ refers to the dipolar momentum of the bound charges. Through this section the total magnetic field $\mathbf{H}$ is renamed as *effective* external magnetic ($\mathbf{H}_{eff}$). The label *effective* refers to the influences of the different sources:

$$\mathbf{H}_{eff} = \mathbf{H}^{ext} + \mathbf{H}^{crys} + \mathbf{H}^{shape} + ..., \tag{3.20}$$

where the label *ext* is the external applied magnetic field, *crys* refers to the magneto-crystalline anisotropy and *shape* to shape anisotropy. For the purpose of this section it is not relevant to discuss the origin of the anisotropies in the crystal lattice. However, they are analyzed in the next chapter.

3.2.1 Landau-Lifshitz-Gilbert equation

In the framework of micromagnetics and considering a homogeneous magnetization, it is possible to observe an alignment of the magnetization with the external magnetic field. The magnetization dynamics is described by the Landau-Lifshitz-Gilbert (LLG) equation.

It is well known that a $\mathbf{H}_{eff}$ which is not parallel to the magnetization, induces a precession of the magnetization in a direction perpendicular to $\mathbf{H}_{eff}$ and the magnetic moment ($\boldsymbol{\mu}_\mathbf{m}$) due to the torque:

$$\mathbf{T}_\mathbf{m} = \boldsymbol{\mu}_\mathbf{m} \times \mu_0 \mathbf{H}_{eff}, \tag{3.21}$$

In addition, $\boldsymbol{\mu}_\mathbf{m}$ is connected with the angular momentum $\mathbf{J}_\mathbf{m}$ through:

$$\mathbf{J}_\mathbf{m} = -\frac{\hbar}{g\mu_B}\boldsymbol{\mu}_\mathbf{m} = -\frac{1}{\gamma}\boldsymbol{\mu}_\mathbf{m}, \tag{3.22}$$

where $\hbar$ is the reduced Planck constant, μ_B is the Bohr magneton, g is the g-factor of the electron and γ is the gyromagnetic ratio. It is convenient to replace $\boldsymbol{\mu}_\mathbf{m}$ by $\mathbf{M}$ (since, $\mathbf{M}$ is the magnetic moment):

$$\mathbf{T}_\mathbf{m} = \frac{d\mathbf{J}_\mathbf{m}}{dt} = -\frac{1}{\gamma}\frac{d\mathbf{M}}{dt} = \mathbf{M} \times \mu_0 \mathbf{H}_{eff} \rightarrow \frac{d\mathbf{M}}{dt} = -\gamma\mu_0(\mathbf{M} \times \mathbf{H}_{eff}), \quad (3.23)$$

Note that this equation is not containing any term which contributes to the energy dissipation, i.e., a friction-like term. In order to give a more realistic description, an additional term which leads to a spiraling down of the magnetization with time is required.

Landau and Lifshitz introduced the phenomenological damping term. It should be perpendicular to $\mathbf{M}$ and $\frac{d\mathbf{M}}{dt}$. They also imposed two restrictions: i) The final state is time independent with $\mathbf{M}$ and $\mathbf{H}_{eff}$ aligned, i.e, this condition implies $\frac{d\mathbf{M}}{dt} = 0$. ii) The equality $|\mathbf{M}|$=M_s is true for any considered time or $|\mathbf{M}|$=$\sqrt{\mathbf{M}^2}$=constant.

$$\frac{d}{dt}\mathbf{M}^2 = 2\mathbf{M}\frac{d}{dt}\mathbf{M} = -2\gamma\mu_0\mathbf{M}(\mathbf{M} \times \mathbf{H}_{eff}) = 0, \quad (3.24)$$

$$\left.\frac{d\mathbf{M}}{dt}\right|_{damping} = -\frac{\eta}{M_s}(\mathbf{M} \times \mu_0[\mathbf{M} \times \mathbf{H}_{eff}]), \quad (3.25)$$

where η is the phenomenological damping constant. Finally the Landau-Lifshitz equation can be written as:

$$\frac{d\mathbf{M}}{dt} = -\gamma\mu_0(\mathbf{M} \times \mathbf{H}_{eff}) - \frac{\eta\mu_0}{M_s}(\mathbf{M} \times [\mathbf{M} \times \mathbf{H}_{eff}]). \quad (3.26)$$

From this equation arises an unphysical situation, because the precession term is not affected by the damping. Therefore, a high enough γ can lead to a situation where the frequency increases and the time to get $\mathbf{M}$ parallel to $\mathbf{H}_{eff}$ becomes shorter.

Gilbert tried to solve this problem by introducing a dissipation time dependent term in the different sources of $\mathbf{H}_{eff}$ which will contribute like:[79]

$$\mathbf{H}_{eff} = \mathbf{H}^{ext} + \mathbf{H}^{crys} + \mathbf{H}^{shape} - \frac{\alpha}{\gamma M_s}\frac{d\mathbf{M}}{dt} + ..., \quad (3.27)$$

where α is the Gilbert damping constant and the formal development results in:

$$\frac{d\mathbf{M}}{dt} = -\gamma\mu_0(\mathbf{M} \times \mathbf{H}_{eff}) + \frac{\alpha}{M_s}\left(\mathbf{M} \times \frac{d\mathbf{M}}{dt}\right). \quad (3.28)$$

Conceptually equation (3.28) implies an increase of the damping with the magnetization precession speed. However, equations (3.28) and (3.26) result in an equivalent expression which is the so called Landau-Lifshitz-Gilbert equation:

$$\frac{d\mathbf{M}}{dt} = -\frac{\gamma\mu_0}{1+\alpha^2}(\mathbf{M}\times\mathbf{H}_{eff}) - \frac{\alpha\gamma\mu_0}{M_s(1+\alpha^2)}\left(\mathbf{M}\times(\mathbf{M}\times\mathbf{H}_{eff})\right). \tag{3.29}$$

3.2.2 Magnons

As it has been mentioned before, the Heisenberg Hamiltonian is not the most appropriate tool to study the behavior of macroscopic ferromagnetic bulks. In micromagnetic approximation the relevant properties are averaged and the model is more suitable for surfaces or volumes. However, interesting features predicted by the Heisenberg model can be found in complex 3D systems. A particularly interesting system for the understanding of the spin Seebeck effect is the one described by a chain of N spins which is simplified by assuming interactions only with the nearest neighbor, spin $s = 1/2$ and exchange energy $J > 0$.[9] Thereby, the equation (2.1) can be reformulated like:

$$\mathcal{H}^{spin} = -2J\sum_n \mathbf{S}_n\mathbf{S}_{n+1}. \tag{3.30}$$

In this system the minimum energy state is reached for all the spin aligned (ground state). The excited state with lowest energy has to be the ground state plus a flip of only one spin. This state, where the spin "m" is flipped, is denoted by $|m\rangle$ and the state of this spin chain with one spin flipped can be formulated as follows:

$$|\psi\rangle = \sum_m |m\rangle\langle m|\psi\rangle, \tag{3.31}$$

where $\langle m|\psi\rangle$ represents the probability amplitude to find the chain with certain spin "m" flipped. By solving the Schrödinger equation and applying the exchange operator to the state $|m\rangle$ it is possible to extract the following dispersion relation:

$$\varepsilon = 2J(1-\cos ka) \quad \rightarrow \quad \omega = \frac{2J}{\hbar}(1-\cos ka). \tag{3.32}$$

For $ka \ll 1$, i.e., the wavelength is much longer than the spacing between spins, then $\omega \approx \frac{Ja^2}{\hbar}k^2$. The result, in comparison with $\frac{\hbar k^2}{2m^*}$, suggests

that if one considers several closed spaced frequencies, it is possible to associate to the displacement of the oscillation along the chain a quasi-particle with an effective mass $m^* = \frac{\hbar^2}{2Ja^2}$. This quasi-particle is called magnon and it can be understood as a quantized spin wave. The spin waves might be compared with sound waves but governed by different dispersion laws (eq. (3.29)). In order to understand the magnon behavior in a 3D ferromagnet at atomic/molecular scale, one has to add to the former assumption of nearest neighbor interaction, the Zeeman energy from a static bias magnetic field H which results in:

$$\mathcal{H}^{spin} = -2J \sum_{n,\boldsymbol{\delta}} \mathbf{S}_n \mathbf{S}_{n+\boldsymbol{\delta}} - g\mu_B H \sum_n S_{nz}, \tag{3.33}$$

where $\boldsymbol{\delta}$ is a a vector pointing in a direction to one of the nearest neighbors of n and H is chosen to give minimum spin configuration when all spins are up. By considering $S_{nz}|s_{nz}\rangle = s_{nz}|s_{nz}\rangle$, a certain number of nearest neighbors and in case of small k, the dispersion relation now has to be expressed, like:

$$\hbar\omega = g\mu_B H + 4Jsa^2k^2. \tag{3.34}$$

Some of the first and more remarkable attempts on the theoretical studies of spin wave interactions were performed by Dyson and Oguchi.[80–82] They divided the interactions between magnons in kinetics, dynamics and a mix between both. The kinetic interaction is related to the fact that the different spin deviations can not appear on the same site rather than being distributed over a certain region. To understand dynamical interaction one should think on the presence of two spin waves at the same time. Such system can be described by using two rotations to the spin vector. However, the rotations will not lead in a commutative result which finally gives a mutual disturbance. Another important result from Dyson's calculations is that the kinetic iteration becomes negligible when the number of magnons is small, i.e., $T \to 0$.

Magnon-driven spin injection

Tserkovnyak introduced in 2002 a novel theoretical mechanism to pump a spin current into a "normal" metal.[83] The "normal" metal is defined as a perfect spin reservoir where the spin can diffuse. For this mechanism a ferromagnet is required in contact with a normal metal (N-F), see figure 3.3. If there is no applied external voltage but a homogeneous magnetic field ($\mathbf{H}_{eff}$) in a certain direction not parallel to the magnetization, a torque is induced (eq. (3.23)). On the interface of the system N-F, the magnetization acts like

a spin pump transferring momentum from the ferromagnet to the normal metal.

In this system the total spin current is divided in two contributions $\mathbf{I} = \mathbf{I}_{sp} + \mathbf{I}_{fl}$. $\mathbf{I}_{sp}$ is the spin current which flows from the ferromagnet to the normal metal and $\mathbf{I}_{fl}$ is the current which flows in the opposite direction. It is important to remark that $\mathbf{I}_{fl}$ is a fluctuating spin current. The $\mathbf{I}_{sp}$ and I_{fl} are described by:[84]

$$\mathbf{I}_{sp} = \frac{\hbar}{4\pi}\left(g_r \mathbf{m}(t) \times \dot{\mathbf{m}}(t) + g_i \dot{\mathbf{m}}(t)\right), \tag{3.35}$$

$$\mathbf{I}_{fl} = -\frac{M_s V}{\gamma}\gamma \mathbf{m}(t) \times \mathbf{h'}(t), \tag{3.36}$$

where $g_{mix} = g_r + ig_i$ is the spin mixing conductance. g_r is related with the Gilbert damping constant and represents the losses of energy due to the spin current. g_i is connected with the gyromagnetic ratio in γ of the LLG equation. $\mathbf{h'}(t)$ represents a random magnetic field which acts on the magnetization and $\mathbf{m}(t)$ is the magnetization direction.

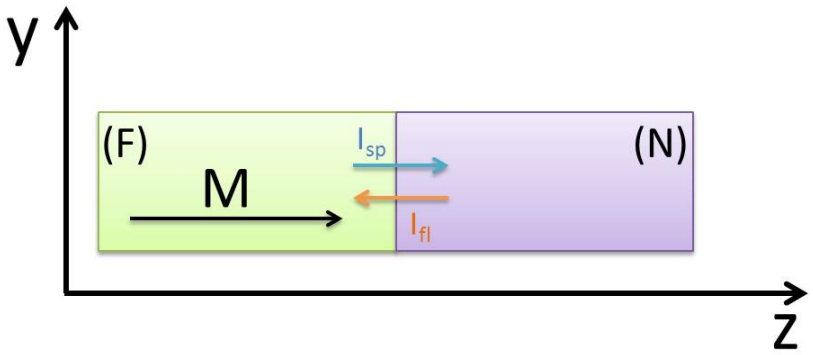

Figure 3.3: (F) and (N) represent the ferromagnetic material and the normal metal, respectively. The figure fixes a coordinate system and it is a scheme of spin injection in a F-N junction. $\mathbf{I}_{sp}$ is spin current flowing from the (F) to (N). $\mathbf{I}_{fl}$ is the uncharged spin current flowing from (N) to (F).

3.3 Spin Seebeck effect (SSE)

The SSE is a novel effect introduced by Uchida et al. in 2008.[4] The effect was explained in terms of "direct" SSE, i.e., due to a difference in the electrochemical potential for each spin channel ($\mu_{(\uparrow,\downarrow)}$) a "spin voltage" appears. The result of an applied thermal gradient and the ISHE is used to convert the spin flux into a measurable charge current. Based on this scenario, Eq. (1.2) has to be reformulated in order to introduce the effect of the spin channels:[85]

$$\begin{pmatrix} \mathbf{J}_c \\ \mathbf{J}_s \\ \dot{\mathbf{Q}} \end{pmatrix} = \sigma \begin{pmatrix} 1 & P & S \\ P & 1 & P'S \\ ST & P'ST & \mathcal{L}_0 T \end{pmatrix} \cdot \begin{pmatrix} \boldsymbol{\nabla}\tilde{\mu}_c/e \\ \boldsymbol{\nabla}\mu_s/2e \\ \boldsymbol{\nabla}T \end{pmatrix} \tag{3.37}$$

where $\mathbf{J}_c$, $\mathbf{J}_s$ and $\dot{\mathbf{Q}}$ are the charge, spin and heat current, respectively. P is the spin polarization of the conductivity and P' is its energy derivative. $\mathcal{L}_0$ is the Lorenz number. μ_c and μ_s are the charge electrochemical potential and the difference between the chemical potential of the spin channels, respectively. This explanation has a fundamental drawback because it ignores the spin coherence length of an electron. The experiment performed by Uchida[4] is done on a film of 8 mm length and the typical spin diffusion length for the electron is in the range of nanometers. In case of long distances ($\approx$mm), Hatamia et al.[85] proved theoretically that the spin accumulation is a local phenomena in equilibrium that can not lead into a lateral non-equilibrium spin current, i.e., the spin flip scattering is short circuiting the spin channels.

Xiao et al.[84] proposed an alternative explanation based on magnons, although it is not a satisfactory explanation for all the available experimental data. However, this theoretical approach gives a theoretical framework consistent with the common SSE experimental dimensions. The whole magnon-driven SSE (MSSE) might be understood as a consequence of three processes: (i) magnon-phonon temperature difference, (ii) magnon-driven spin pumping and (iii) inverse spin Hall effect.

3.3.1 Previous considerations

It is assumed that the systems phonon (p), conduction electron (e) and magnon (m) can be described by their local temperature and the interactions electron-phonon are stronger compared to the interaction with magnons. Consequently, it is possible to consider that locally, their temperatures in the ferromagnet are $T_F^e = T_F^p \equiv T_F$. The same consideration can be taken for the normal metal $T_N^e = T_N^p \equiv T_N$. This consideration might not be extended to the magnon system, therefore for both systems $T_{F,N} \neq T_{F,N}^m$. However,

T_F^m is affected by the temperature of the other systems $\alpha T_F^m = \alpha_0 T_F + \alpha' T_N$, where α is the total magnetic damping constant, α_0 is the bulk damping and α' enhanced damping.[84]

3.3.2 Magnon-phonon temperature difference.

Sanders and Walton[86] studied the magnon-phonon temperature distribution when a temperature gradient is established between the ends of films made of YIG. They established boundary conditions in this scenario in which phonons are excited on the edge of the sample where the heater is located and diffuse to the cold side. During the diffusion process, the phonons interact with the magnons. Therefore, the temperature in the magnon system depends on the flux of energy through the phonon system. The magnons are isolated from the nonmagnetic heat bath.

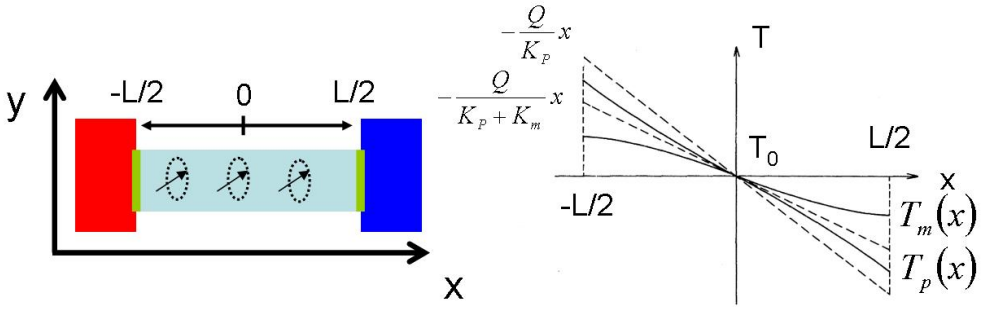

Figure 3.4: Left figure: Scheme of heat boundary conditions. The red rectangle represents heater or warm side. The blue rectangle represents cold side. Green line represents the interface from (to) where the phonons can take (transfer) energy. Right figure: Solid lines represent $(T_{m,p}(x))$ the temperature profile for magnons and phonons, respectively. Dashed lines, represent the temperature profile for phonon system in the limiting cases of perfect coupling and no coupling with the magnon system.[86]

The temperature difference is written as follows:[84]

$$\Delta T_{mp}^{-1}(x) = \frac{1}{\eta \Delta T} \frac{\sinh \frac{L}{2\lambda}}{\sinh \frac{x}{\lambda}}, \tag{3.38}$$

where the reference system is fixed in figure 3.4 and λ is the magnon diffusion length. η is a complicated function wich depends on K_m, K_p, K_T, K'_m and K'_p. $K_T = K_p + K_m$ is the total thermoconductivity of the magnetic isolator

material, where the magnon system is label by (m) and the phonon system by (p). $K'_{p,m}$ is the phonon and magnon thermoconductivity on the interface between the warm (cold) side and the magnetic material. In the scenario described by the magnon driven spin Seebeck effect, the magnons can only interact with phonons in the magnet, therefore $K'_m \to 0$ and in addition, it is assumed $K'_p \to \infty$. By using this boundary conditions, the function η might be reduced to:[84]

$$\eta = \frac{K_T}{\frac{L}{\lambda}K_p \coth\frac{L}{2\lambda} + 2K_m} \approx \frac{1}{\frac{L}{\lambda}\coth\frac{L}{2\lambda}} \tag{3.39}$$

It is possible to assume that in a ferromagnet the electron-phonon relaxation time would be faster than the magnon-phonon relaxation time. Therefore, the phonon-electron system will be in thermal equilibrium. This makes it easy to extend the previous calculations to ferromagnets by replacing $K_p \to K_{pe} = K_p + K_e$. K_e is the thermoconductivity of the electron system.

3.3.3 Magnon-driven spin pumping caused by ΔT_{mp}

In order to simplify a first approach, it is considered: i) the framework of the macro spin approximation and ii) the system composed by a normal metal jointed to a ferromagnet described on section 3.2.2. In this case, the process is activated by ΔT_{mp}.

In the system presented on figure 3.3 the total spin current injected can be formulated like:[84]

$$\langle I_z \rangle \approx \frac{\gamma\hbar g_r k_B}{2\pi M_s V}\left(T_F^m - T_N\right) \equiv L'_s \Delta T_{mp} \tag{3.40}$$

where the fraction before brackets is the interfacial spin Seebeck coefficient and it is denoted by L'_s. Conceptually, it is possible to extract from the former equation that the spin pumping is caused by the temperature difference between magnons and the system composed by electrons and phonons. The magnon is a collective motion which might be extended in the range of mm (depending on the material). Therefore, this approach conceptually fits with the dimensions of the original experiment.

In order to present a more realistic description of the discussed problem, one has to consider an extended ferromagnet, where different magnetic domains can exist. To get a result for the new situation, it is just necessary to replace the ferromagnetic V on equation (3.40) by the coherence volume V_a. This V_a defines a volume where the magnon temperature can be considered constant.

3.3.4 Inverse Spin Hall effect

In the final step of this process (fig.3.5), the spin flow diffusing to the normal metal (equations (3.35) and (3.40)) is converted in a measurable voltage V_H trough the inverse spin Hall effect which has to be proportional to the temperature difference. The expected Hall voltage for this phenomena can be calculated via:

$$V_H = \xi \frac{\sinh \frac{z}{\lambda}}{\sinh \frac{L}{2\lambda}} \Delta T \tag{3.41}$$

where ξ is a function of the interfacial spin Seebeck coefficient and geometrical factors like the length of the normal metal (fig. 3.5) and the contact area.

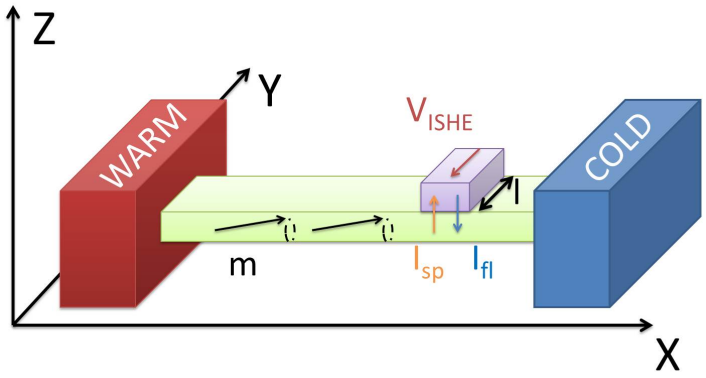

Figure 3.5: Sketch of the global scenario through which the magnon-driven spin Seebeck effect (MSSE) arises.

By using the equation (3.41) an expected value for permalloy of $\xi = 4.4\mu V/K$[84] is obtained and the measured value by Uchida et al. is $\xi = 0.25\mu V/K$.[4] The predicted value is 20 times higher than the measured one. Xiao et al. speculate that the origin of this discrepancy in ferromagnetic materials might be due to the uncertainty in the relaxation times for magnons and phonons which were used to perform the theoretical calculations.

3.3.5 Further considerations

Recent experiments have shown an enhancement of the magnon-driven spin Seebeck effect (MSSE) signal measured at low temperatures[87] and a persistent signal when the spin flow is interrupted by doing a scratch on the

magnetic material.[88] Adachi et al.[87] argued that, once a stable temperature gradient is reached, there is locally no temperature difference between the ferromagnet and the substrate which holds the ferromagnetic film. In this situation the phonons propagate through the substrate, interact with the phonons in the ferromagnet thus overcome the blocking of the spin flow.

In addition, it is well known that the thermopower is enhanced by phonon drag[89–91] at low temperatures. This process is due to the decay of the number of phonons available for an Umklapp process with the temperature $n(k) \approx e^{-\Theta_D/T}$,[2] i.e., by reducing the temperature it is possible to reach a point where the mean free path for the phonons involved in an Umklapp process is similar to the mean free path of one ballistic scattering event due to imperfections or defects of the crystal structure. Therefore, the phonon mean free path is increased by reducing the temperature, τ_{ph}. Since the ISHE is proportional to the magnon-phonon interaction, it is plausible to expect a dependence of V_{ISHE} (fig. 3.5) with τ_{ph}. In fact, Adachi et al.[87] found a relation between the phonon relaxation time and the spin current injected:

$$I_{sp}/\nabla T = P'\tau_{ph}\mathcal{B}_1\mathcal{B}_2 \tag{3.42}$$

where P' is an approximately temperature independent coefficient and $\mathcal{B}_1$ and $\mathcal{B}_2$ are functions dependent on the Debye temperature, the temperature and the phonon velocity. A good agreement results from comparing this theoretical predictions with the available experimental data (fig. 3.6).

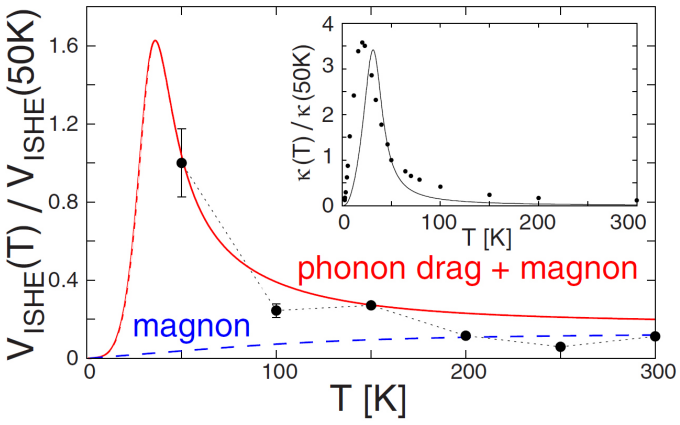

Figure 3.6: Values of V_{ISHE}: Blue line: Theoretical predictions due to the magnons. Red line: Theoretical predictions due to the magnons + phonon drag. Black dots: Measured values for $Y_3Fe_5O_{12}$. Figure taken from .[87]

Chapter 4

Deposition and film characterization

The investigations presented in this thesis were carried out on various thin films. Most films were prepared and characterized using the following procedure: Typically, the samples were produced by sputtering in an ultra high vacuum system. The material was deposited onto MgO (100), Al_2O_3 (110) or Si (100) substrates. After deposition, the morphology of the sample surface was analyzed by an AFM. The thickness was determined using x-ray reflectometry. Grain size and crystal structure were measured by x-ray diffraction in 2-circle and 4-circle x-ray diffractometers. Finally, the saturation magnetization was measured using a VSM or using a SQUID (Quantum Design MPMS II). These described steps are the common procedure which was followed to produce and characterize the samples studied. In the case of permalloys, low coercive fields and a low damping constant is more important rather than to achieve a good crystalline ordering. Therefore, permalloy samples were not investigated with the 4-circle x-ray diffractometer.

The following chapter introduces the individual production and characterization steps. Specific experimental setups used to perform transport or optic measurements are discussed in separate chapters (where a general description is required to understand the data) as well as the physical principles which they are based on.

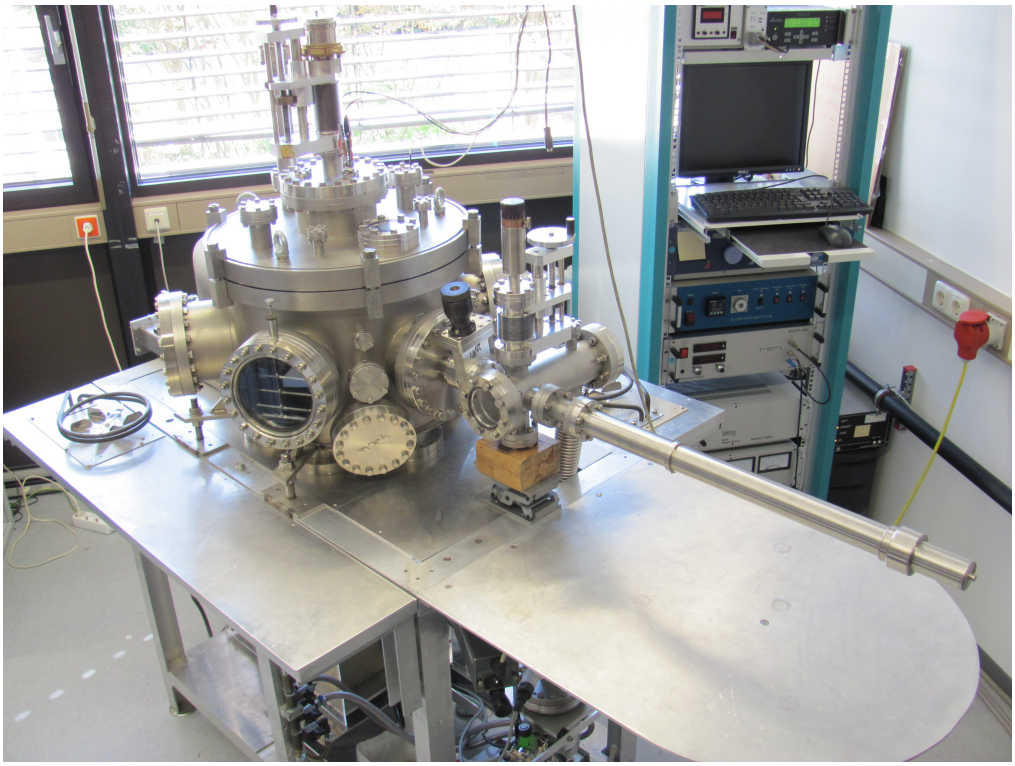

Figure 4.1: Ultra high vacuum system.

4.1 Deposition procedure

4.1.1 Ultra high vacuum system

The ultra high vacuum system (UHV) which was used is presented in figure 4.1. It can be divided into a load lock and a main chamber. Both parts are connected to different pumps which are configured to lower the pressure. In a first step of the regular bake-out procedure, the pressure is lowered from atmospheric pressure to $\approx 1 \times 10^{-2}$ mbar by a pre-pumping system, through the load lock. Once this pressure is reached, the main chamber is separated from the load lock by using a gate valve. Then, a turbo molecular pump evacuates the load lock system to $\approx 5 \times 10^{-8}$ mbar. Finally, the main chamber is connected to its own pump system. However, in order to reach a pressure close to $\approx 1 \times 10^{-9}$ mbar in short time, the process of outgassing has to be accelerated. The whole chamber can be covered with a thermal isolation box. Afterwards, the closed environment is heated to 150 °C for 12 hours using 2 resistive heaters and 2 fans. This process removes water and other

contaminants from the inner wall surfaces which reduces the time required to reach the working pressures.

In the load lock a magazine is mounted which allows to store 4 substrates. A transfer arm can be used to transport the samples from the load lock to the main chamber.

Inside the main chamber, there are 6 CF100 flanges at the bottom (fig. 4.2 right), distributed in a ring geometry. Five of them are used to mount cathodes. Three of them are used to mount magnetic targets and two for non magnetic targets. On the sixth place, a window is mounted which allows us, in combination with a mirror mounted below the window, to measure the film temperature by radiation. Each cathode has its own gas and water cooling line which can be manipulated independently.

On the upper flange, a mass spectrometer can be found which is used to measure the gas composition and to perform leak tests. A ceramic plate is used as heater and it can reach temperatures up to 1100 °C. The substrates transported from the load lock are placed below the heater and they can be located on top of any cathode by using a rotating arm.

4.1.2 Sputtering

In science and industry, sputtering commonly refers to a process in which gas ions are accelerated against a target (Fig. 4.2 left). As a result of the collision of the gas ions with the target, some material is extracted and it is collected onto a surface of a substrate (deposition process). In order to control the possible sources of contamination, the whole process takes place in a closed system which can be pumped down to UHV conditions. However, UHV is not an essential condition. In order to initialize the process, the UHV system is filled with inert high purity argon gas. The ignition of the plasma can be performed by applying a DC voltage. It generates a difference in potential between a cathode (which is located the target material) and an anode. This describes the basic sputtering mechanism.

Typically, in the sputtering process, it is possible to tune the sputtering current, the temperature of the substrate and the gas pressure, which results in a certain control of the properties of the studied material. The highest kinetic energy of a sputtered particle or cluster is determined by the applied voltage. The crystallographic properties and surface textures of the deposited layer are strongly influenced by the temperature of the substrate either during the deposition or after the deposition (annealing process).

To initialize the plasma and to get a stable burning plasma a high enough ionization probability is needed which requires high enough pressure. The deposition rate is a function of the pressure $f(1/p)$, i.e., the higher is the

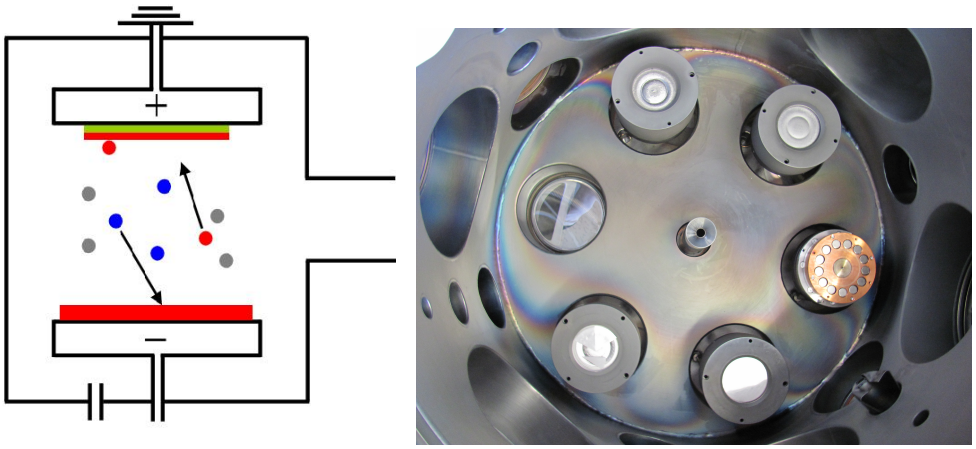

Figure 4.2: Left: Sputtering scheme. Grey dots represent neutral Ar atoms. Blue dots represent positively charged Argon atoms. Red dots represent sputtered atoms or clusters. The green line represents the substrate. Right: Inner view of the main chamber. The three upper features are cathodes for magnetic materials and the two lower ones are for non-magnetic materials. The cathode on the right shows the magnet distribution for magnetron sputtering.

pressure the lower is the mean free path. This means that an increase in pressure leads into an increase of the ionization probability and stabilizes the plasma but it also results in low deposition rates. In order to achieve high deposition rates magnetron sputtering is used. In this sputtering technique, two concentric rings of magnets are placed below the target. Because of this, electrons are trapped in the magnetic field. As they circulate over the target, they increase the ionization probability and reduce the amount of gas required for the process. A characteristic ring appears on the target surface as a consequence of the magnets distribution (fig. 4.2 right). The drawback of this technique is that a considerable amount of the target material is unused.

The break-through voltage needed to initialize the process becomes extremely high to sputter dielectric materials.[92] Therefore another approach is required. In this case, a radio frequency source is used. Instead of using a DC-Voltage, one applies a voltage which can be described by $V(t) = V_{dc} + V_{rf} \sin \omega t$. The RF-sputtering exploits the different mobilities between electrons and ions. A V_{dc} is self adjusted to avoid the ion accumulation on the target surface. A match box is frequently placed between the cathode and the radio frequency generator to minimize the reflected power and to maximize the power dissipation in the discharge.[93] This method can be also used

with conducting targets. It has the advantage to require lower gas pressures to initiate and maintain the plasma stable.

Although they are not used in this thesis, there are other possibilities to sputter. For instance, in reactive sputtering, Oxygen or Nitrogen are used as sputtering gas. For some industrial applications, cylindrical rotating targets are used to increase the percentage of used material in combination with magnetron sputtering.

4.1.3 Substrate

The research performed on anomalous Hall effect is connected with the crystalline structure of the used Heusler alloys. In order to get certain control on the crystal quality of the compounds, the appropriate choice of the substrate is an important issue. Many previous works report an epitaxial growth of Heusler thin films with high crystal quality on MgO (100) and Al_2O_3(110) substrates. In epitaxial growth or heteroepitaxial growth, a material A (Heusler alloy) is growing on top of a material B (substrate) and A follows the crystal arrangement of B, as this behavior is energetically favorable. The quality of the epitaxial growth is straight forward connected with the mismatch between the lattice constants of A and B. This lattice mismatch leads to an increase of the elastic energy with increasing layer thickness. If the thickness reaches a certain critical value, then it will be energetically favorable to reduce the nonuniform strain field by an island-like formation or by formation of dislocations. To prevent such situation, the substrate has to be chosen with regard to the lattice constant. The three used Heusler compounds present a lattice constant a $\approx 0.57\,\mathrm{nm}$.[42,94,95]

MgO crystallizes in a cubic structure with a lattice constant a $\approx 0.42\,\mathrm{nm}$. The diagonal of each face, which contains three identical atoms, is $\approx 0.59\,\mathrm{nm}$. Consequently, it is energetically favorable to grow the Heusler alloys rotated by 45 ° in respect to the MgO cubic structure, i.e. following the diagonal direction. Al_2O_3 has a hexagonal crystal structure with a,b $\approx 0.47\,\mathrm{nm}$ and c $\approx 1.29\,\mathrm{nm}$. Despite the mismatch between the used Heusler alloys and Al_2O_3, it is still possible to grow films with high crystal quality.

It is not necessary to grow monocrystalline permalloy to get its characteristic ferromagnetic properties. In fact, permalloy is grown even onto amorphous substrates.[96,97] In the research based on permalloy, good thermal conductivity of the substrate is required. Therefore, it is preferable to use Al_2O_3 at room temperature due to its high thermal conductivity, $23\,\mathrm{W/mK}$. At low temperature ($\approx 30\,\mathrm{K}$) both Al_2O_3 or MgO are suitable.[98]

Si (100) has cubic structure with a lattice constant a $\approx 0.54\,\mathrm{nm}$. This substrate is selected in the context of mass production. It is used if the lattice

constant is not a relevant parameter. However, price and easier availability in industry are key considerations.

It is common requirement to grow thin films on clean surfaces. For this purpose, Al_2O_3 and Si are cleaned by four successive ultrasonic baths of acetone and isopropanol. The surface of MgO reacts with H_2O and CO_2. Therefore, in order to remove such contaminants, it is heated up to 900 °C inside the vacuum chamber.[99] This cleaning process of heating is also applied on Al_2O_3 and Si.

4.2 Characterization techniques

4.2.1 Surface characterization

It is a well known experimental fact that the surface roughness is connected with the transport properties on metallic and semiconducting films.[100] By increasing the electron scattering on the surface, a reduction of the conductivity is obtained. One of the first theoretical approaches to this phenomenon was performed by Fuchs.[101] In his quasi-classical theory, the so-called classical size effect, the roughness of the surface is considered using phenomenological parameters which take the role of boundary conditions in the electron distribution function. However, the conductivity of Heusler alloys is closer connected with the crystal structure ordering than with the surface roughness.[102] Despite this fact, a decrease of the conductivity (longitudinal and transversal) might be partially due to the increasing roughness surface.

In order to be able to estimate qualitatively the influence of the roughness on the conductivity, the surface of the films deposited at different deposition temperatures (T_d) has to be measured. Such measurements are performed using an AFM in a non-contact mode. This technique, invented in 1986, uses a flexible cantilever in which a tip scans over the surface of the sample. While the surface is scanned, the cantilever is deflected and a program can construct an image of the surface out of the measurement of the cantilever deflection. The cantilever deflection might be due to different forces and depending on the used force, the AFM is working in a particular mode. For this research, it is convenient to preserve the surface morphology in order not to introduce extra sources of scattering for electrons. Therefore, the non-contact mode is appropriate, because it is desirable to measure transport properties on the samples. In the non-contact mode, the tip is placed some nanometers above the sample and the cantilever is oscillating at a frequency slightly out of resonance with a typical maximum amplitude lower than 10 nm. In this configuration, the Van der Waals forces ($\approx 10^{-12}$ N) will act on the cantilever

reducing the resonance frequency while the amplitude is kept constant.

Surface morphology evolution

Samples of $Co_2FeSi_{0.6}Al_{0.4}$ and $Co_2FeGa_{0.5}Ge_{0.5}$ were deposited on MgO and Al_2O_3 at different temperatures by DC-sputtering and their surfaces were systematically studied.

Figures 4.3 and 4.4 show AFM pictures taken on $Co_2FeGa_{0.5}Ge_{0.5}$. The behavior exhibited by this compound can be also observed on $Co_2FeSi_{0.6}Al_{0.4}$.

Bellow a deposition temperature of 450 °C[1], one does not observe any significant feature in the morphology of the Heusler thin films studied. Neither, on the ones deposited on MgO or Al_2O_3. From 450 °C to 750 °C, the samples deposited on MgO show a characteristic labyrinth structure which is becoming more pronounced while the samples are deposited at higher temperatures (Figs. 4.3 a) and c)). Instead of this, samples deposited on Al_2O_3 show a granular morphology (Fig. 4.3 d)). By increasing the deposition temperature, the samples show again a labyrinth structure but less pronounced. This can be seen on the samples deposited at 750 °C (Fig. 4.3 b)). In the former range of temperature the average roughness is ≈15 nm. For samples deposited at temperatures higher than 750 °C, the labyrinth structure breaks down to a columnar structure (Figs. 4.4). The height of the columns match with thickness of the films, at least up to 80 nm which is the thickest film studied.

The morphology of the surface was also studied depending on certain T_d for different thicknesses. As it can be seen in the profile of the figure 4.4 b), for 30 nm thin films deposited at 750 °C, columns of ≈ 30 nm in height and 100 nm in width can be observed. While the thickness of the thin film increases, the material from close areas merges and it results in wider columns. This structures can reach a width up to 500 nm for thin film thickness of 80nm (Fig. 4.4 a)). This trend is also observed for samples deposited at lower temperatures. For instance, ≈ 20 nm thickness samples deposited onto MgO at 750 °C, show small labyrinthine structures which become bigger and better defined as the thickness increases.

It has been shown that a progressive increase of the deposition temperature, produces an increase of the roughness. In the case of Heusler compounds, where the electrical resistivity is tightly connected with the crystal structure, it might be challenging to separate the contribution of the surface

[1]The deposition temperature of the substrates can be measured by a thermo element or by a pyrometer. The deposition temperatures used in the thesis correspond to the ones measured with the pyrometer.

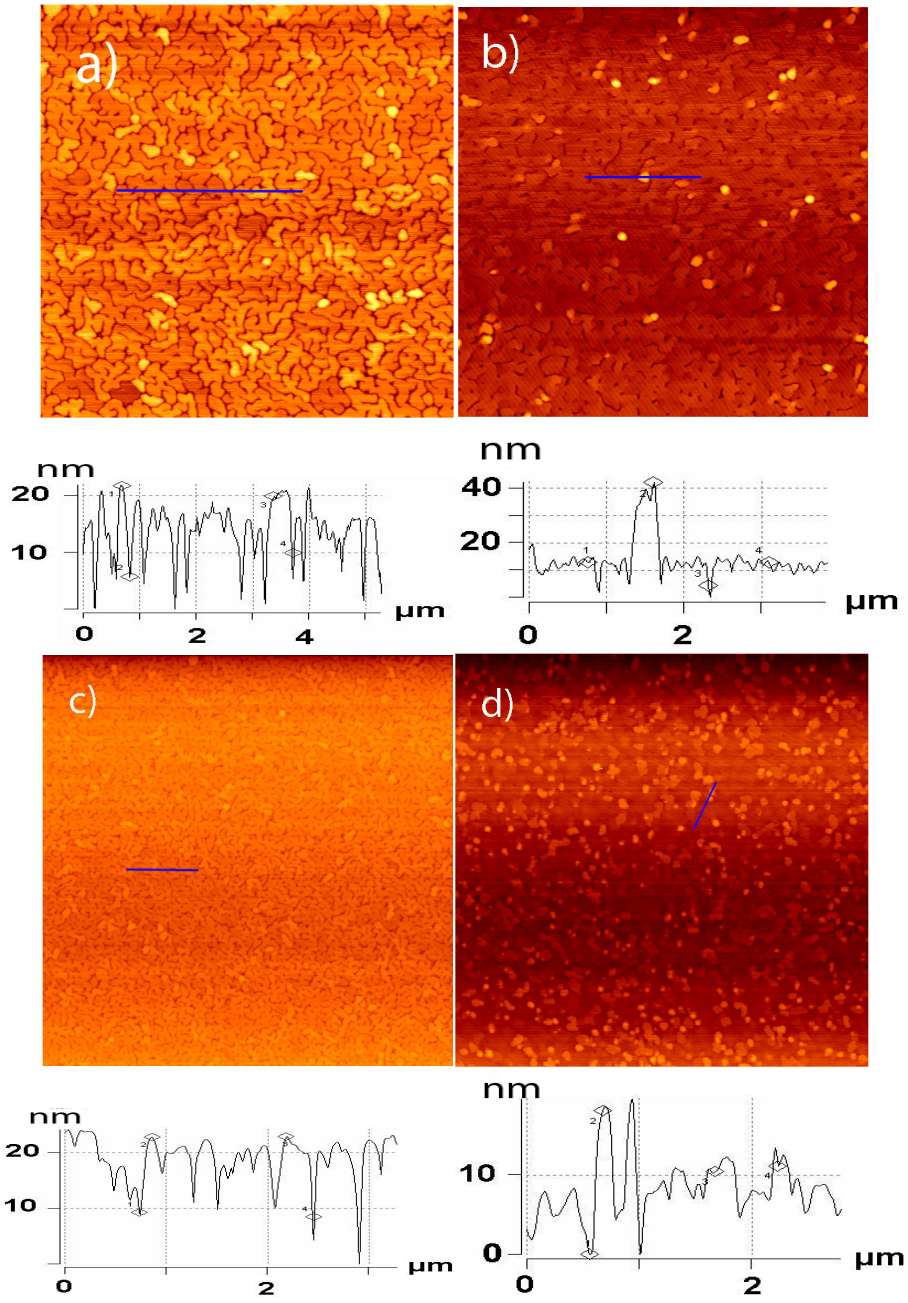

Figure 4.3: AFM pictures of $10\times10\mu m$ lateral size taken on films of 70nm thickness of $Co_2FeGa_{0.5}Ge_{0.5}$ deposited at 750°C (up) and 625°C (down). Onto MgO (left) and onto Al_2O_3 (right). Plots below the pictures show height profiles of the measurements.

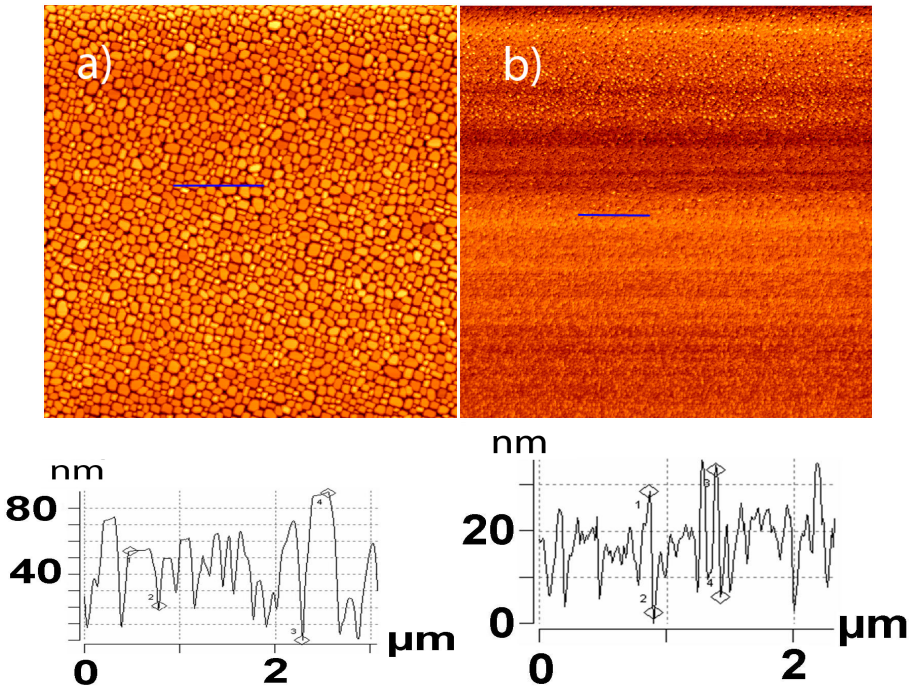

Figure 4.4: AFM pictures of $10\times10\mu m$ lateral size taken on films of $Co_2FeGa_{0.5}Ge_{0.5}$ deposited at 950°C onto MgO. The thickness of the film shown in a) is ≈80nm and ≈ 30nm for b), respectively.

scattering from the other sources which all together rise the measured resistivity. However, the columnar organization of the thin films deposited at the highest temperatures could lead to isolated columns which might block the path of the electrons. Therefore, it is convenient to establish an upper limit of 700 °C to study the transport properties. Above this limit, the surface morphology might mask the signal.

4.2.2 X-ray diffractometry and reflectometry

The crystal structure of Heusler compounds changes by depositing at different conditions. In order to infer qualitatively how the crystal structure is evolving by shifting systematically some of the deposition parameters, a probe with a size comparable to the inter-atomic distances is required. X-ray sources of Cu $K_{\alpha1}$ radiation which have a wave length of $\lambda = 1.54056\ \mathring{A}$ are commonly used to perform such investigations.

An extensive theoretical description of the different interaction mechanisms and experimental techniques can be found in other books.[103] In this

section, general concepts are sketched. In order to simplify the description, it is convenient to constrain the treatment by imposing some boundary conditions. It is considered a thin film made of a single layer with an infinite lateral size. The incident and a scattered wave have the same wave length. The experiments were performed in a Bragg Brentano geometry, where scattered waves can be only emitted above the sample. In the description using kinematical scattering theory it is considered that each x-ray photon is scattered only one time in an elastic process. In this conditions, the incident monochromatic wave is

$$\mathbf{E}_0(r,t) = \mathbf{E}_0 e^{-i(\omega t - \mathbf{k}_0 \mathbf{r})}, \tag{4.1}$$

where $|\mathbf{k}_0| = |\mathbf{k}|$ and they are the wave vectors for the incident and the scattered waves, respectively. If one selects a common origin for $\mathbf{k}$ and $\mathbf{k}_0$ the opposite ends of vectors are placed on the surface of the so-called Ewald sphere. In a von Laue formulation, a pair of scattered beams are considered. They have to satisfy the following condition in order to produce constructive interference

$$\mathbf{d} \cdot (|\mathbf{k} - \mathbf{k}_0|) = 2\pi m, \tag{4.2}$$

where $\mathbf{d}$ is the Bravais lattice vectors, m is an integer number and $|\mathbf{K}| = |\mathbf{k} - \mathbf{k}_0|$ is a vector of the reciprocal lattice. If now, a primitive unit cell is considered, composed of different atoms located at positions $\mathbf{d}_1 ... \mathbf{d}_n$, the phase difference will be $\mathbf{K} \cdot (\mathbf{d}_i - \mathbf{d}_j)$. The total intensity will be a sum over all the scattered rays[2]

$$I \propto \left| \sum_{j=1}^{n} f_j(\mathbf{K}) e^{i\mathbf{K}\mathbf{d}_j} \right|^2, \tag{4.3}$$

with $f_j(\mathbf{K})$ being the atomic form factor. It depends on the Fourier transform of the charge distribution ρ_j of the ion which occupies certain position $\mathbf{d}_j$

$$f_j(\mathbf{K}) = -\frac{1}{e} \int d\mathbf{r}\ e^{i\mathbf{K}\cdot\mathbf{r}} \rho_j(\mathbf{r}). \tag{4.4}$$

The relation presented in the former equation becomes specially important to understand the influence of the disorder on the scattered beam and to recognize the limitations of this method. In equation (4.4) the intensity of a beam scattered in certain direction (h,k,l) depends on the electronic environment of the particular atom involved in the scattering. Therefore, the substitution of an atom in a certain position d_j by another one which has similar $\rho_j(\mathbf{r})$ might lead in to an unrecognizable change of the intensity.

In case of Heusler compounds (X_2YZ), the form factor in different crystallographic directions can be calculated as follows[104]

$$F(111) = 4|f_Y - f_Z|, \tag{4.5}$$

$$F(200) = 4|2f_X - (f_Y + f_Z)|, \tag{4.6}$$

$$F(220) = 4|2f_X + (f_Y + f_Z)|, \tag{4.7}$$

where F(hkl) is depending on the miller indexes, f_X, f_Y and f_Z are the form factors of the elements occupying the positions X, Y and Z (Fig 2.2), respectively. In the investigations presented, where the disorder in the crystal lattice is a key factor, Co_2MnZ and Co_2FeZ have been used. Co, Fe and Mn are transition metals and the main difference, in terms of electronic distribution, is only one and two d-electrons of difference between Co-Fe and Co-Mn, respectively. In consequence $f_{Co} \approx f_{Fe} \approx f_{Mn}$.

As it was already mentioned, the DO_3 disorder refers to a random exchange between X (Co) and Y (Fe) atoms. Therefore, an exchange of f_{Co} and f_{Fe} will not have an appreciable influence on F(111), F(200) and F(220). Consequently, the trend of this disorder with the change of the deposition parameters can not be easily analyzed by this method. The diffracted patterns of powder samples crystallized in different crystal arrangements are simulated by the program "Powder cell" (Fig. 4.5). The red curve represents $Co_2FeSi_{0.6}Al_{0.4}$ crystallized in a $L2_1$ phase and the blue curves in a DO_3 phase. In these curves the different diffracted peaks exhibit similar intensities.

In the case of B2 disorder Y (Fe) and Z (Si and Al) are randomly exchanged. In this case, the intensities of the diffracted beams in (200) and (220) directions remain unmodified (Fig. 4.5). On the other hand, depending on the percentage of B2 disorder present in the crystal lattice, the intensity of the peak (111) can even vanish. The green curve (Fig. 4.5) represents powder sample of $Co_2FeSi_{0.6}Al_{0.4}$ fully crystallized in the B2 phase. Therefore, by comparing the integral intensity of the peak (111) from samples deposited at different conditions it is possible to establish a general trend of the B2 disorder evolution. The same can be applied to (hkl) diffracted peaks with all the Miller indexes equal to odd numbers.

The A2 disorder represents a random exchange between the atoms located in X, Y and Z positions. The presence of this phase influences the intensity of (111) and (200). For 100 % of A2 phase the (200) vanishes (Fig. 4.5).

For the crystal structure analysis, a X-ray diffractometer in a four circle geometry was used in order to perform a detailed study of the ordering (Fig. 4.6).

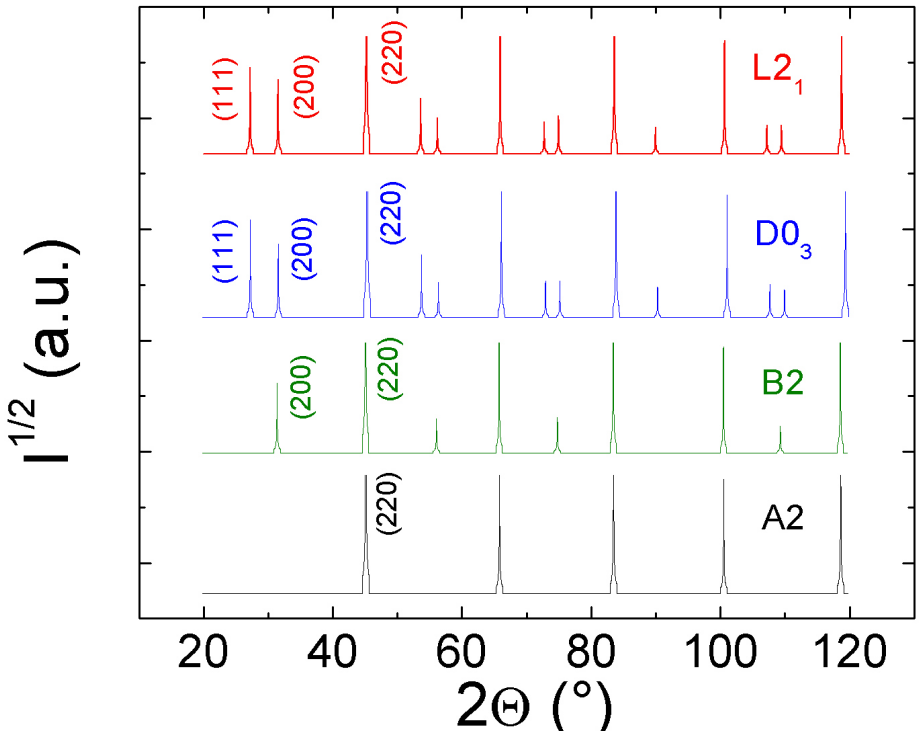

Figure 4.5: $L2_1$, B2 and DO_3 simulated diffraction pattern of $Co_2FeSi_{0.6}Al_{0.4}$ with the program Powder Cell. The numbers between brackets represent Miller indexes (hkl).

ϕ scans (ω, 2Θ and χ remain constant) were used to prove the alignment between the crystalline structures of the substrate and the thin film. They are also used to investigate the presence of domains.

Figure 4.7 shows representative data for the studied Heusler compounds. In figure 4.7 on the right the expected rotation by 45 ° between the crystalline structure of MgO and the Heusler compound is measured which occurs due to their lattice mismatch. In contrast, all the studied Heusler compounds follow the structure of Al_2O_3 (Fig 4.7, left). The presence of different domains is observed, which is in agreement with previous results. Due to the bigger lattice mismatch, the underlying substrate, accommodates the Heusler compounds in different directions. The case of Co_2MnAl (Fig 4.7, left) is particularly remarkable because it presents a lower amount of domain structures compared with the other studied materials.

The presence or absence of the families of reflections {111} and {200} or-

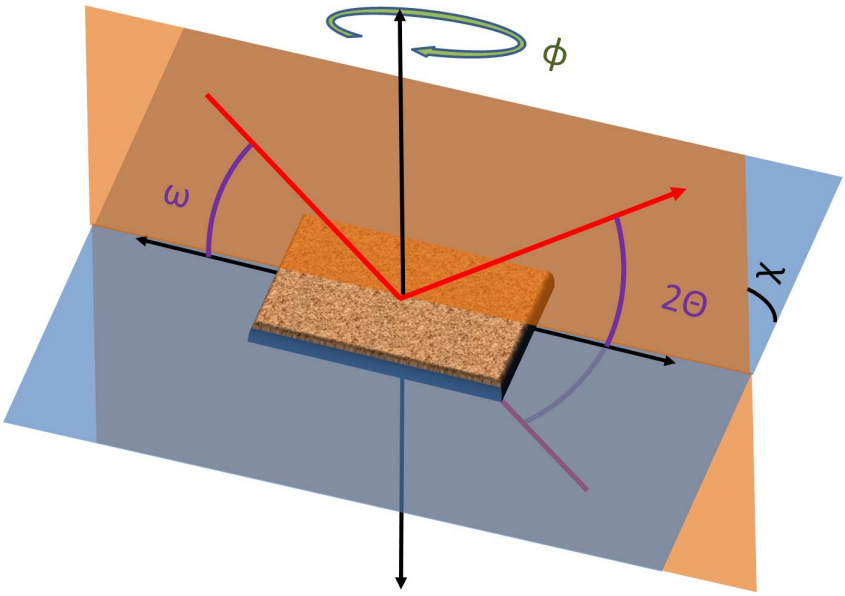

Figure 4.6: General scheme of a x-ray diffractometer, where the red arrow marks the direction of the x-ray beam from the source. In a two circle geometry, ω and 2Θ can be changed. In a four circle geometry, it also possible to rotate the sample in ϕ and χ.

dering are commonly investigated. These reflections indicate the $L2_1$ ordered crystal structure. Typically, $Co_2FeSi_{0.6}Al_{0.4}$ and $Co_2FeGa_{0.5}Ge_{0.5}$ deposited in the range of temperatures from 450 °C to 750 °C and at $4{\cdot}10^2$ mbar of argon pressure show the characteristic (111) reflection. Co_2MnAl does not show the (111) reflection at any conditions.

In a statistically homogeneous distributed sample, the density and types of defects are homogeneously distributed in the lateral direction. Therefore, a statistically homogeneous scattered beam arises from the diffraction with such an object. In the measured intensity, there will be a contribution from the coherent and the incoherent scattering.[103] In the reciprocal space a diffraction peak at a given scattering vector $\vec{G}$ of the reciprocal lattice is not longer a δ-function but the peak suffers a broadening (Fig. 4.8). Consequently, the intensity is measured in reciprocal space planes that contain the scattering vector, but are aligned perpendicular to the scattering vector. These scans give information on the alignment of the crystallites corresponding to rocking curves done in perpendicular directions, e.g., in ω and χ. Linear scans changing the length but not the orientation of the scattering vector are equivalent to 2Θ scans and yield information on the size of the

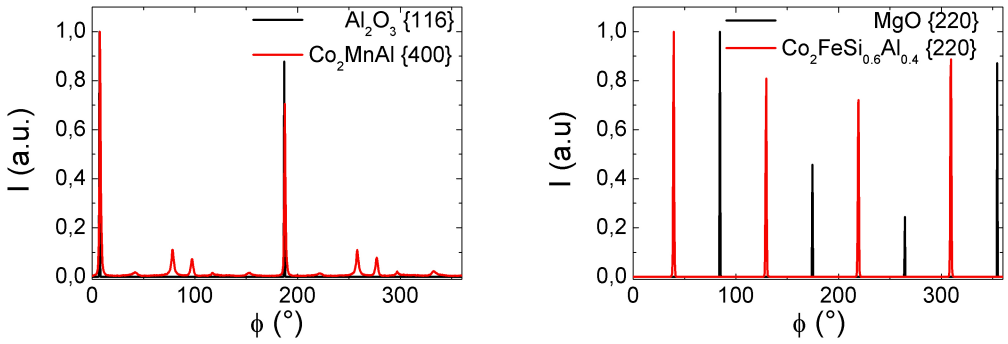

Figure 4.7: ϕ scans performed on thin films deposited at 750°C and $4{\cdot}10^2$mbar of argon pressure. Left: Co_2MnAl deposited onto Al_2O_3. Right: $Co_2FeSi_{0.6}Si_{0.4}$ deposited onto MgO.

coherent scattering region.

For each reflection family ({1,1,1}, {2,0,0}, {2,2,2} and {2,2,0}) the intensity of the full scattering ellipsoid was determined. The integral intensity increases for all peaks due to an increased crystallite size. Also, it is necessary to remark that $L2_1$ and DO_3 order contribute to the integral intensity detected in the (111) peak. B2 and A2 disorder produce a vanishing of the (111) reflection. In addition, A2 also produces a vanishing of the (200) reflection. Consequently, to perform a quantitative ordering evolution study, the ratios I_{111}/I_{400} and I_{111}/I_{200} have to be inspected. For annealing temperatures lower than 600 °C, the experimental data show a linear decrease of the ratio I_{111}/I_{200}[105] which ends at 450 °C. It also shows a quasi constant behavior between 600 °C and 750 °C with a maximum at 650 °C. Therefore, the deposition temperature range between 490 °C and 710 °C was systematically studied for different thin film thicknesses in $Co_2FeGa_{0.5}Ge_{0.5}$ onto MgO.

The data reproduces the behavior for the ratio I_{111}/I_{200} at constant thickness in the whole range of temperatures (Fig. 4.9). Qualitatively, this coincidence could be understood in terms of similar lattice constant and atomic mobility for the compound studied by Arbelo et al.[105] and $Co_2FeGa_{0.5}Ge_{0.5}$. However, it is convenient to remark that this behavior can not be fully explained by using the former arguments, because they are also applicable for Co_2MnAl, but $L2_1$ structure was never reported on thin films. Also, an investigation reported in a recent paper[105] was performed on thin films deposited at room temperature and post annealed. The ones presented in the current thesis are deposited at different substrate temperatures. Even though, they

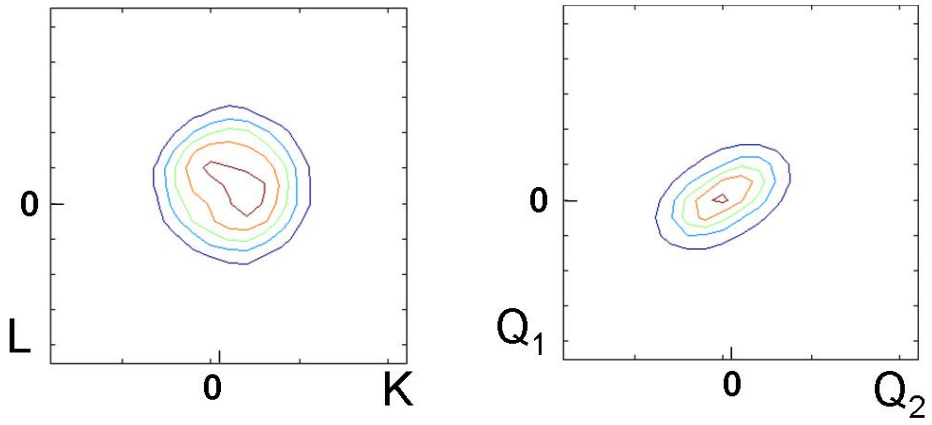

Figure 4.8: Plane scan on the (200) and (111) reflections, left and right pictures respectively. K and L are Miller Indices. Q_1 and Q_2 mark a reference system perpendicular to the (111) reflection.

present the same tendency for a particular thickness. Further analysis, presented in next the chapter, shows up $I_{111}/I_{200} \neq 0$ even at 450 °C which make the experimental process of deposition at certain substrate temperature more convenient in terms of achieving good crystal structures.

In order to have a further insight in the crystal ordering concentration, the experimental data from the ratios I_{111}/I_{200} has to be compared with theoretical predictions. The simulations are performed by PowderCell program (developed by Werner Kraus and Gert Nolze, on the Federal Institute for Materials Research and Testing BAM, Berlin). This program is prepared to simulate and manipulate the diffraction pattern of the crystal structures. It even allows to simulate the presence of a percentage of disorder. Most of the scans performed on the 2-circle difractometer are done in a Bragg-Brentano geometry, i.e. the detector is placed under an angle 2Θ respect to the incoming beam, while the sample surface is at an angle Θ.

Unfortunately, to obtain an exact simulation of the diffraction peaks and their shapes is a quite complex topic. One has to consider finite size of the sample, penetration depths, illuminated area, polarization of the beam, contributions from dislocations, strains in the lattice, non-uniform composition,...

Therefore, the I_{111}/I_{200} ratios obtained by PowderCell have to be used for a qualitative analysis. Also, one has to keep in mind the former discussion about DO_3 disorder. Nevertheless, it is possible to give a rough estimation of

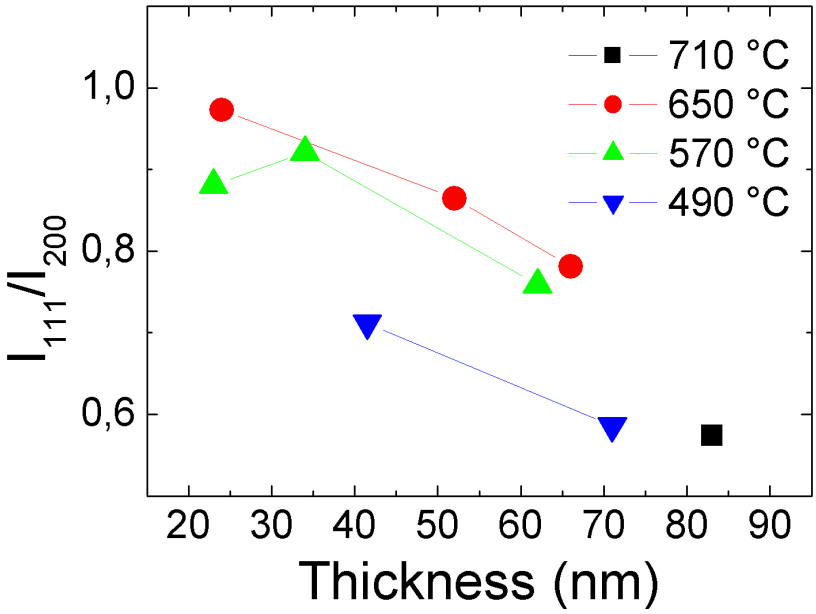

Figure 4.9: $Co_2FeGa_{0.5}Ge_{0.5}$ onto MgO at $4{\cdot}10^{-2}$mbar argon pressure. Ratio I_{111}/I_{200} against thin film thickness and deposition temperature (T_d).

the $L2_1$ content in the samples. Values presented in figure 4.9 are compatible with $L2_1$ concentration lower than 28 %.

If an uniform distribution of the crystallites is assumed and the samples can only contain either $L2_1$ or B2 structure, then the former result opens two possible scenarios. i) The samples contain grains which are fully crystallized in a $L2_1$ or in a B2 structure. In this case, the grain size ratio between grains which contain $L2_1$ and the grain which contains B2 has to be around 1/4. ii) The other possibility is to have both structures mixed in each grain. Consequently, the grain size ratio between $L2_1$ and B2 structures has to be around 1. In both cases, the Scherrer-Formula[106] can be used to investigate those scenarios.

If monochromatic radiation is diffracted by a random oriented crystal, a broadening of the peak in the resulting diffracted radiation depending on the crystallite size is observed. P. Scherrer was able to infer the crystallite size out of this broadening. He introduced the so-called Scherrer-Formula:[106]

$$L \approx \frac{K\lambda}{\Delta 2\Theta \cos\Theta}, \tag{4.8}$$

where K is a numerical constant $2(\ln 2/\pi)^{1/2} = 0.93$, λ is the wavelength of the monochromatic radiation, Θ is the angle shown in figure 4.6 and $\Delta 2\Theta$ is the Full Width Half Maximum (FWHM) of the rocking curve for one particular (hkl) direction. Different values of the Scherrer constant K can be calculated by using alternative numerical approximations which consider different shapes or distributions of the grains.[107]

In order to perform this study, sets of samples of $Co_2FeGa_{0.5}Ge_{0.5}$ and $Co_2FeSi_{0.6}Al_{0.4}$ of 70nm thickness were deposited onto MgO and Al_2O_3 at different substrate temperatures (from 450 °C to 750 °C) by DC-Sputtering. The parameter $\Delta 2\Theta$ for the characteristic family of reflections {111} and {200} was analyzed for each sample. The resulting data show up values of approximately ≈ 10 nm associated with {111} and ≈ 11 nm associated with {200} independently of the deposition temperature. This result points out that inside each grain coexists different crystalline ordering.

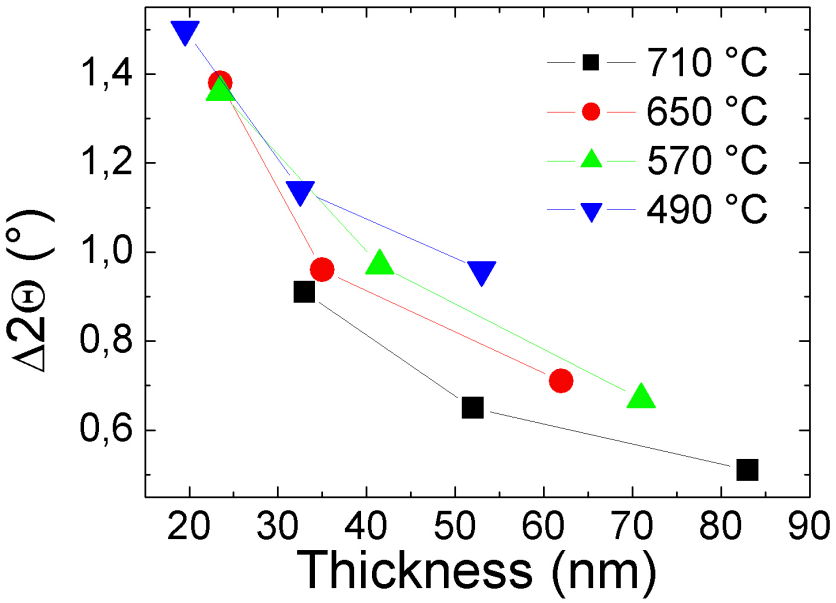

Figure 4.10: $Co_2FeGa_{0.5}Ge_{0.5}$ onto MgO at $4{\cdot}10^{-2}$mbar argon pressure. $\Delta 2\Theta$ of (400) peak against deposition temperature (T_d) and thickness.

An increase of the crystallite size and better crystallite arrangement is observed (lower values of $\Delta 2\Theta$, fig. 4.10) by increasing the film thickness. Their partner values (fig. 4.9) show a reduction of the I_{111}/I_{200} ratio by increasing the film thickness i.e. a reduction of the content of $L2_1$ phase. However, one

has to keep in mind that different corrections might be required, in order to compare properly, measurements coming from films with different thickness. It is not possible to exclude that part or the whole reduction of the I_{111}/I_{200} ratio caused by reducing the thickness is an artificial effect. Particularly, the lowest I_{111}/I_{200} value in figure 4.9 which corresponds to a 80 nm sample deposited at 710 °C is too small. For this temperature, one would expect $I_{111}/I_{200} \approx 0.7$. This expected value is extrapolated from a linear fit for samples deposited at 650 °C (fig. 4.9). It can be explained by a misalignment.

Transport measurements were performed to cross check the relation between ordering and thickness. For this purpose, two $Co_2FeGa_{0.5}Ge_{0.5}$ thin films at 550 °C and 4×10^{-2} mbar of Ar pressure were deposited by DC-Sputtering with 50 mA. The deposition time of the first film was 360 s and it offers a residual resistivity ratio of 1.5. The second one was deposited at the same conditions but twice the time and it gives a residual resistivity ratio of 1.36. This result can not be taken as a proof of the x-ray result. However, it points consistently in the same direction.

In this paragraph, it is presented a picture of the growth process. In the discussion it is assumed that a tendency exists to reduce the amount of $L2_1$ by increasing the film thickness. For a film thickness of about 20 nm, small structures or grains appear, as can be seen in figure 4.4 right (higher values of $\Delta 2\Theta$ on figure 4.10 at certain T_d). These crystallites contain higher amount of the $L2_1$ order structure (higher values of I_{111}/I_{200} on figure 4.9 at certain T_d). The main source which introduces defects and disorder at such thickness might be due to the crystal structure minimizing the elastic energy caused by the lattice mismatch with respect to the substrate. While the film keeps growing, the crystals merging form coarser structures (Fig. 4.4 left). During the merging, crystal structures with a slightly different crystallite arrangement come together. The different crystallite arrangement or phase should fit on each other. This might lead into a different degree of disorder or to the introduction of defects (lower values of I_{111}/I_{200} on figure 4.9 at certain T_d).

A further important issue in this section is the determination of the thickness of a thin layer. The thickness is determined by x-ray reflectometry. These measurements are performed using a diffractometer with a two circle geometry. The basic idea is to use a phenomena equivalent to the interference fringes observed in visible light to determine the thickness of samples. It is possible to divide the thin films in three media: substrate, metal and air. If the incident angle is sufficiently small, each interface reflects the x-ray radiation and an interference pattern can be measured. The measured interferences depend on the differences of the reflective indexes and the roughness (in the nm scale). Besides, the dynamical scattering theory[103] offers a relation

between thickness and the positions of the intensity maxima

$$2t\sqrt{\sin^2\alpha_{im} - \sin^2\alpha_c} = m\lambda, \tag{4.9}$$

where t is the film thickness, α_{im} is the angular position, m is an integer number, λ is the wave length and α_c is the critical angle of the total reflection of the film. The former equation is equivalent to the Bragg relation. For small incident angles, equation (4.9) can be conveniently approximated to[103]

$$\alpha_{im}^2 - \alpha_c^2 \approx m^2(\frac{\lambda}{2t})^2. \tag{4.10}$$

Equation (4.10) allows to estimate the thickness just by measuring the position of several maxima. In order to perform an accurate thickness estimation, the reflected pattern is simulated by Parrat. The main parameters needed to perform the simulations are the refractive indexes, the roughness and the thickness. This software is also capable to simulate many interfaces, therefore it can be also used for multilayer systems.

4.2.3 Bulk magnetometry

The saturation magnetization (M_s) is a characteristic property of ferromagnets. Particularly, for half-metallic ferromagnets a certain value of M_s is connected to a characteristic crystal structure. Even without a straightforward relation between M_s and the ordering of the crystal lattice, the M_s can be used in combination with x-ray data to estimate qualitatively whether the sample has certain content of the $L2_1$, DO_3 or B2 phase (Fig. 2.5). For instance, it is possible to measure two samples with approximately the same integral intensity for the (111) reflection but different values of M_s. Therefore, it is possible to estimate the change in the concentration of disorder. In case of permalloys, it is more interesting to know the coercive field in the direction of the applied temperature gradient. The voltage measured for the magnon-driven spin Seebeck effect should describe an hysteresis loop (V vs. H) which might match with the hysteresis loop measured for the magnetization (M vs. H).

For this purpose, our facilities are provided with a vibrating sample measurement (VSM) and a SQUID (Quantum Design MPMS II). In both devices the sample is mounted in a rod which is introduced in a cryostat. These instruments allow to perform measurements from 2 K to 300 K (in case of the SQUID up to 400 K). Typically, samples of $10\times5\,\mathrm{mm}^2$ are mounted with the long side parallel to the applied magnetic field (H) in a coil geometry. The rod is hold by a mechanical oscillator on the opposite edge of the sample.

Through the vibration introduced by the oscillator, an oscillating magnetic flux appears. It will be detected by a pickup coils.

VSM exploits Faraday's law. An oscillatory motion of a magnetized sample induces a voltage in the coils which can be detected. The induced voltage will be proportional to the sample's magnetization and can be measured by using a lock-in technique.[108]

RF-SQUID is a sensitive detector for measuring magnetic flux and it is used in many applications. In the available setup, the sample is mounted in a rod. This rod is introduced on the SQUID magnetometer and it places the sample in a set of superconducting coils. While the sample is moving to different positions in the coils, the superconducting coils produce a current to compensate the magnetic flux created by the magnetic sample. The current is transported by a "flux transformer" to the field free region where the superconducting loop with a Josephson junction is placed. The resistivity from this SQUID arrangement will change. A feedback coil compensates the change of flux at the SQUID position. Therefore, one measures the change in current produced by the feedback coil which counter acts the changes produced by the coils with Josephson junctions.

4.2.4 X-ray photoelectron spectroscopy (XPS)

XPS is a spectroscopy technique used to analyze semi-quantitatively the chemical composition of the surface. This technique becomes interesting in the course of this work since it allows to estimate how the oxidation evolves in time, how deep the oxidation reaches into the thin films or to find out an effective way to preserve the samples.

The basic idea of this method consists in the use of a x-ray source to irradiate a target and to ionize the atoms. In the ionization process, the atoms will emit electrons with a characteristic energy. The electrons are collected and their energy is analyzed. Each element present in the target contributes to the final spectrum with a set of peaks at specific energies. Depending on the energies associated with those peaks and their intensity, the stoichiometric composition of the surface can be estimated. The following balance of energy has to be considered for electrons from the surface that could leave the sample without inelastic scattering:

$$E_b = h\nu - E_k, \tag{4.11}$$

where E_b is the binding energy, $h\nu$ is the energy of the incident radiation and E_k is the kinetic energy of a resulting electron. By measuring the distribution of E_k, the binding energy can be infered. Since each element has

a characteristic electronic configuration, the different elements can be identified. Note that the former equation describes a process which implies two steps. To remove an electron from the atom E_b is needed and E_k determines the movement of the free electron. In solids, the binding energy is considered with respect to the Fermi level instead to the vacuum. Consequently, the work function Φ has to be considered (Fig. 4.11).

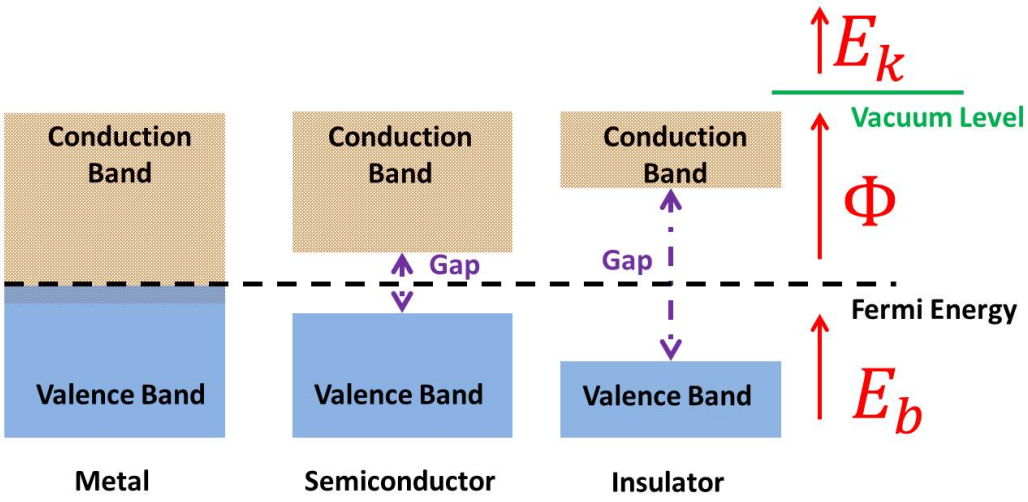

Figure 4.11: Schematic description of the energy bands at 0 K.

In a regular XPS spectrum, it is possible to distinguish valence electrons, core-like electrons and Auger electrons. The valence electrons, which have the lower E_b, have a maximum $E_b \approx 20eV$. The electrons which come from the inner shells are called core-like electrons and typically show the most sharp and intense peaks. By using x-ray beams with high enough energy, it is possible to observe Auger electrons. For this relaxation process, a X-ray photon releases a core electron. An other electron from a higher level occupies the vacancy and emits a photo-electron. The kinetic energy of such photo-electron is calculated as the energetic difference between the primary electronic transition and the ionization energy for an electron in a particular shell from where it is emitted. Their kinetic energy is driven by the orbital energy from the primary electron transition, it will lead in to a fixed E_k for Auger electrons. In addition, a background arising from inelastically scattered photoelectrons is added to the measured spectrum.

This technique is strongly sensitive to oxidation or chemical contamination. Such processes produce a shift in the measured peaks or chemical shifts.

In order to preserve the surface of the sample from contamination, the measurements were performed in a UHV system, at a base pressure of 10^{-10} mbar and a x-ray source with an Al anode (1486,6 eV) was used.

Chapter 5

Influence of disorder on AHE

The general features related with the evolution of the crystal structure by using different thickness and temperature deposition were presented in the previous chapter. This evolution implies a change in the order phase as a function of the deposition temperature. The influence of the defects and disorder phase on the electric transport properties of the Heusler compounds is presented in this chapter. As it was already mentioned, a part of this thesis is focused on Anomalous Hall effect. Therefore, the results regarding the data treatment of the AHE will be discussed in detail. In addition, the longitudinal resistivity (ρ_{xx}) and the anisotropic magnetoresistance ($\rho_{xx\perp}$ and $\rho_{xx\parallel}$) in $Co_2FeSi_{0.6}Al_{0.4}$ and $Co_2FeGa_{0.5}Ge_{0.5}$ were studied. These results will be also presented in the current chapter to complement the data from AHE.

For this purpose, epitaxial thin films of the selected material were grown on MgO (100) and Al_2O_3 (110) substrates by DC-magnetron sputtering in an UHV system with a base pressure of 1×10^{-9} mbar. Argon at 4×10^{-2} mbar served as sputtering gas to prepare several sets of samples. They were deposited at different deposition temperatures (T_d) in a range from 450 °C to 700 °C in order to tune the amount of defects. X-ray diffraction (XRD) and measurements of the saturation magnetization were used to inspect the crystal structure.

The current chapter is divided in two sections: i) experimental considerations, where different experimental details are given in order to properly understand how the measurements were performed. A short analysis of the crystal structure of the films used in this research is presented, too. ii) Transport measurements, where the data is presented and discussed.

5.1 Experimental considerations

In order to minimize any possible accidental damage on the films by measuring them on different devices and to ensure that the properties of a film can be associated to its partner film, a 10×10 mm substrate and a second one of 10×5 mm were mounted on the same holder. The deposition procedure took place simultaneously on both substrates.

The film deposited on the substrate 10×5 mm was used to determine the magnetization saturation (either with VSM, SQUID or both in order to check the measurements). Its thickness was also determined. Finally, it was mounted on the 4-circle diffractometer. The different scans were performed to get the integral intensity from each peak of each reflection family ({1,1,1}, {2,0,0}, {2,2,2} and {2,2,0}).

On the partner 10×10 mm thin film, the thickness was also measured. Typically, it was found a difference in thickness between the two films prepared simultaneously of ≈ 5 nm. This is probably due to a misalignment between the cathode and the substrate position during the deposition process. On the next step, these films were etched and used to measure the electric transport properties.

The etching took place in a clean room class 100 (ISO 5). The process was required to increase the accuracy of the measurements. In this process, the samples were covered with a positive photoresist. In order to dry it, the sample was annealed up to 95 °C on a heat plate. A mask from a glass plate was selected and placed on top of the sample to draw a Hall bar. Then, the sample was illuminated 15 s with an UV lamp and chemical reactions took place in the uncovered part of the photoresist. This process resulted in a figure drawn on top of the films. Once this was done, the uncovered area could be removed. The unprotected areas could be etched by argon bombarding in an ion bean chamber placed inside the clean room.

The Hall measurement depends mainly on the film thickness $V_H = \frac{R_H B I}{t}$, where V_H is the expected Hall voltage and t is the film thickness. However, heat dispersion and measurement accuracy can be optimized by choosing an appropriate length/width ratio of the Hall bar etched on the sample. Experimentally, one has to consider that instead of V_H, one is measuring $V_m = -\int_{-w/2}^{+w/2} E_y dy$, where V_m is the experimental value. Isenberg et al.[109] theoretically and experimentally studied the ratio V_m/V_H as function of the ratio l/w. They found that when the l/w ratio is increased then the ratio V_m/V_H goes to 1. This value is reached at $l/w = 4$. However, any value of l/w between 2 and 4 gives a ratio $V_m/V_H > 0.92$.[109] In addition, it is convenient to use the same film to measure the magnetoresistance parallel and transversal

to the applied magnetic field ($\rho_{xx\perp}$ and $\rho_{xx\parallel}$). Therefore, the width has not to be much smaller than the length. In consequence a Hall bar of $8 \times 3\,\mathrm{mm}^2$ is selected, which gives a ratio $l/w \approx 2.6$ (fig. 5.1).

Further experimental considerations are related with the measurement procedure itself. For cancellation of thermovoltages, parallel and antiparallel current was applied, and the resulting absolute values of voltages were averaged. To avoid magnetoresistive contributions due to misalignment of the contacts, the measurements of Hall effect were accomplished with positive and negative magnetic field.

All the samples were placed in a ^{4}He cryostat. It allowed to change the magnetic field by using superconducting coils and to perform measurements from 2 K to 300 K. It also offered the possibility of mounting the samples parallel or perpendicular to the applied magnetic field.

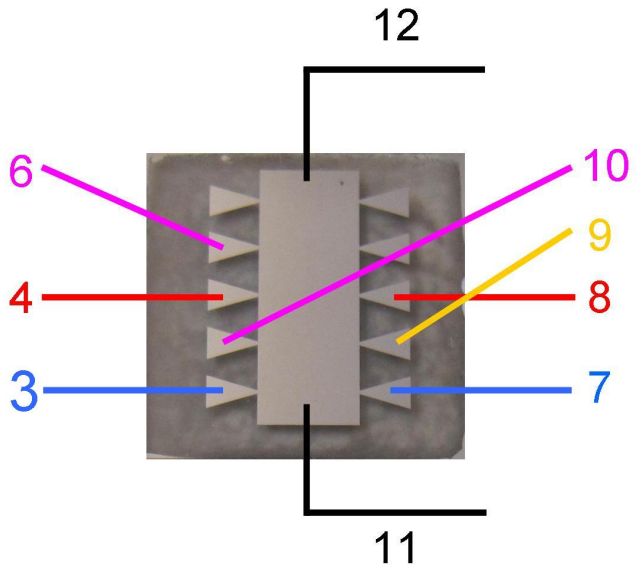

Figure 5.1: Hall bar and wiring scheme. Colors and numbers are related with internal working parameters of the ^{4}He cryostat. The lines describe the wires distribution in the set-up.

First, the sample (fig. 5.1) was mounted perpendicular to the magnetic field and it was cooled down to 5 K. However, during the cooling process, a magnetic field was not applied yet. While, it was cooled, a current was set through the contacts 12-11 (black lines) and the voltage between 6-10 (pink lines) was measured ($\propto \rho_{xx}$). Once the temperature was stabilized at 5 K, a magnetic field was established from -5 T to +5 T in steps of 0.2 T. The Hall

voltage was measured ($\propto \rho_{xy}$) by the contacts 4-8 (red lines). Afterwards, the temperature was enhanced in steps of $\approx 50\,\mathrm{K}$ and the procedure was repeated to measure the Hall effect for each temperature step. Finally, the platforms were mounted parallel to the magnetic field (the long side of the Hall bar was parallel to the magnetic field). A sweeping magnetic field was applied and a current was placed through the contacts 12-11 (black lines) and the voltage ($\propto \rho_{xx\parallel}$) was measured by using the connections 6-10 (pink lines). To measure the part $\propto \rho_{xx\perp}$, it is required a current transversal to the magnetization. The connections 4-8 (red lines) and 3-7 (blue lines) were used to place a current. They were used simultaneously. This minimizes the non parallel contributions between the points 10-9 (pink and yellow lines). While the magnetic field was swept, the contacts 10-9 served to measure the voltage ($\propto \rho_{xx\perp}$). Unfortunately, the analysis of the magneto resistance data is not adding new relevant data.

Previous works[110] revealed a discrepancy of 2 % between electric transport measurements performed on cobalt based Heusler compounds thin films capped with a thin Al layer and uncapped. The uncapped films, also exhibit an unchanged crystal structure and magnetic properties, even six months later. Therefore, there was no need to cap them. The typical time scale was not exceeding in any case two days, since the thin film were produced shortly before they were measured.

5.1.1 Sample characterization

As it was already discussed, the DO_3 disorder is challenging to detect with a laboratory x-ray source. Co and Fe have nearly the same form factor in x-ray scattering. However, ab initio calculations suggest a high formation energy for DO_3 disorder.[111] Experimentally, in the case of Heusler compounds, DO_3 disorder increases with the annealing temperature, becoming important above 600 °C.[112] On the other hand, it is possible to estimate indirectly the presence of this kind of disorder since it is responsible for the reduction of the measured saturation magnetization at high temperatures.[44] In consequence, it is impossible to give a precise value of the degree of order in the respective crystal structure in the samples. However, a magnetic moment of 5.5 μB/f.u. is expected for both compounds in fully ordered samples. Considering the data from XRD and magnetometry together (fig. 5.2) allows to analyze qualitatively the evolution of the crystal structure in relation to the deposition temperature.

In chapter 4 the x-ray data of $Co_2FeGa_{0.5}Ge_{0.5}$ was shown and analyzed. In the current chapter, x-ray data of $Co_2FeSi_{0.6}Al_{0.4}$ is used to have a complete overview about the x-ray data for both compounds. Figure 5.2 (right)

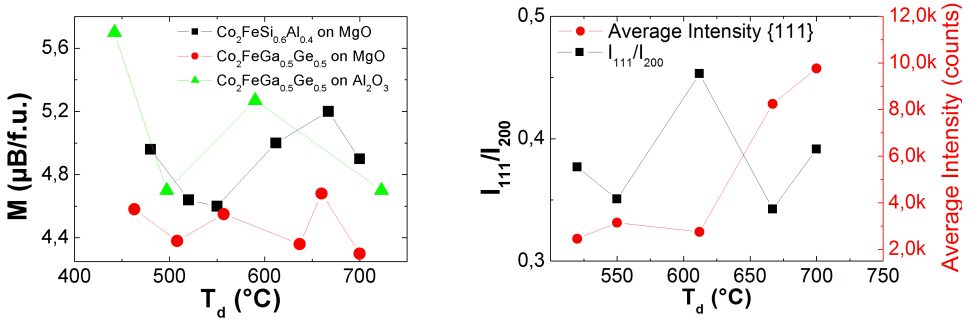

Figure 5.2: Left, saturation magnetization for different compounds as a function of deposition temperature. Right, Crystallographic analysis of ordering peaks determined in a four circle geometry for $Co_2FeSi_{0.6}Al_{0.4}$. Square symbols (left ordinate) represent the ratio of the integral intensity between (111) and (200) reflections. Circular symbols (right ordinate) represent the integral intensity measured for the (111) reflection.

indicates a maximum degree of $L2_1$ ordering for the $Co_2FeSi_{0.6}Al_{0.4}$ sample deposited at 600 °C by a corresponding maximum in I_{111}/I_{200}. In agreement with this XRD result for this sample preparation temperature, maximum residual resistivity ratio ($\rho_{xx}(300K)/\rho_{xx}(50K)$) was found (Fig. 5.3 (b, d and f)). The red line on figure 5.2 right is used to stress that the increase of the integral intensity is not going in parallel with an increase of the I_{111}/I_{200} ratio. It proves the necessity of study the integral intensity ratio between reflection peaks instead of the integral intensity.

Additionally, the saturation magnetization was measured by a superconducting quantum interference device (Quantum Design MPMS II). Figure 5.2 (left) shows a common maximum around 600 °C. The increase in the value of magnetization at low temperatures should be attributed to the formation of A2 disorder. The maximum magnetization value at 600 °C is reached when the $L2_1$ structure is prominently formed and the final decrease is due to introduction of a significant amount of DO_3 disorder.[44,111]

5.2 Electronic transport measurements

In this section, the data of $Co_2FeSi_{0.6}Al_{0.4}$with different degree of ordering is used as a reference to analyze qualitatively and quantitatively ρ_{xx} and ρ_{xy}. As the same behavior is observed for $Co_2FeGa_{0.5}Ge_{0.5}$, the analysis can accordingly be extended to this second compound. There is only one

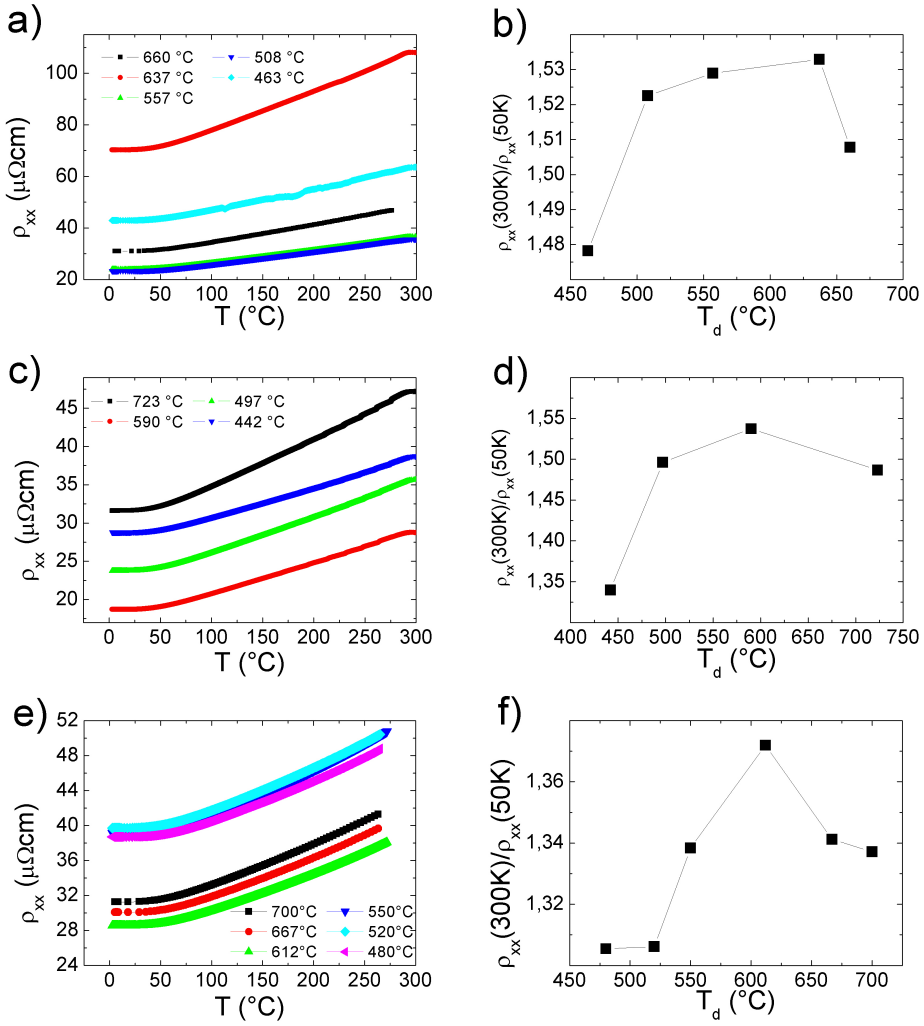

Figure 5.3: a), c) and e) ρ_{xx} measured at different temperatures of $Co_2FeGa_{0.5}Ge_{0.5}$ on MgO and Al_2O_3 and $Co_2FeSi_{0.6}Al_{0.4}$ on MgO, respectively. b), d) and f) residual resistivity ratio, where T_d is the deposition temperature.

discrepancy in the longitudinal resistivity data. Figure 5.3 (a) shows the data for $Co_2FeGa_{0.5}Ge_{0.5}$ on MgO. The red curve shows maximum absolute values of ρ_{xx}. This could imply maximum concentration of defects. However, it also shows (fig. 5.3 (b)) maximum value of residual resistivity, which is suggesting better crystalline ordering. In addition, the Hall effect measurements for this sample shows no discrepancy with the general trend. In consequence, the discrepancy in absolute value might be attributed to an unappropriate

wiring. Unfortunately, it was not possible to remeasure the sample. ρ_{xx} (fig. 5.3) and ρ_{xy} (fig. 5.4) were determined at various temperatures and in a magnetic-field range from 0 to 50 kOe. The following discussion is done considering the same compound ($Co_2FeSi_{0.6}Al_{0.4}$). Therefore in a metal with a simple Fermi surface one should observe the same intrinsic or band effects. However, in the case of Heusler compounds, the former affirmation is no longer true because the introduction of disorder or defects can modify appreciably the shape of the Fermi surface. The main difference between the samples discussed is the amount of atomic disorder and the quality of grain alignment. In consequence, any observed effect should be attributed mainly to defects and disorder. Doing a qualitative analysis of $\rho_{xx}(T)$ raw data, the data curves displayed in figure 5.3 (a, c and e), can be split in a temperature independent resistivity below 50 K and a temperature dependent resistivity above,

$$\rho_{xx} = \rho_{xx0} + \rho_{xxT}(T) \tag{5.1}$$

In a semiclassical framework, ρ_{xx} is inversely proportional to the mean free path. The temperature-independent part, ρ_{xx0}, is proportional to the defect concentration and it reaches a minimum value for the sample with lowest defect concentration. One can attribute an increase of defect concentration with the enhanced ρ_{xx0} for films deposited at temperatures higher than 600 °C or deposited at low temperatures. The increase of ρ_{xxT} at higher temperatures of measuring is related with the increase of the scattering events due to the thermal phonon and magnon excitation. Theoretically, the ρ_{xxT} is modeled with a function proportional to T^{α}. The value of α is connected with the scattering mechanism.[113,114] Experimental works performed on Heusler compounds[110,115,116] reveal that the value of α is also function of the measuring temperature. These results suggest that the scattering mechanisms change progressively their contribution while the measuring temperature is changed.

Each plot in figure 5.4 shows $\rho_{xy}(H)$ data measured at different temperatures. By extrapolating the data of $\rho_{xy}(H)$ taken above saturation to zero magnetic field one can extract the value of ρ_{xy}^{AHE} corresponding to each temperature. The extrapolation method is explained in detail in many references.[7,110,117,118]

From the direct observation of the ρ_{xy} raw data, two general relations arise between the crystal quality and ρ_{xy}^{AHE}. Like in the ρ_{xx} case, ρ_{xy}^{AHE} is approximately temperature independent below 50 K. The low-temperature values for the different samples evolve with the deposition temperature. They assume negative values for samples deposited at high temperatures with higher

concentration of DO_3 disorder (figs. 5.4(a) and 5.4(b)). The values at intermediate temperatures are close to zero (fig. 5.4(c)) for the sample with the highest degree of $L2_1$ order. Finally, they tend to positive values, for samples deposited at low temperatures with more defects and lower degree of $L2_1$ crystalline order (figs. 5.4(d) and 5.4(f)). It is important to remark that like in ρ_{xx}, the absolute value of ρ_{xy}^{AHE} reaches a minimum value in the same range of deposition temperatures. This indicates the presence of mechanisms connected with defect and disorder concentration participating both in longitudinal and transverse resistivity. In the appendix, the $\rho_{xy}(H)$ raw data for $Co_2FeGa_{0.5}Ge_{0.5}$ deposited on Al_2O_3 and on MgO is shown.

Figure 5.5 represents the anomalous Hall resistivity against the longitudinal resistivity. Equation (3.14) is used to fit the data. While the data points can be reproduced nicely by this relation, one must note that a region without physical meaning appears in all cases and is marked in the plots. This is due to the fact that this equation is not considering explicitly the possibility of different scattering mechanisms that contribute qualitatively different to the AHE. Subsumming to only one skew scattering and one intrinsic contribution yields the fits shown in figure 5.5. Remarkably, the linear contribution visible in the low ρ_{xx} regime has a negative sign for all these fits.

At the actually measured low-temperature resistivities ρ_{xx} the linear contribution would give a huge negative AHE, which, however, seems to be nearly exactly compensated by the positive quadratic contribution for all samples with different disorder. Also evidence for a curvature is not visible in the raw data of figure 5.5, while a quadratic contribution is evaluated from the fitting procedure. This data evaluation has no meaning in compounds with a significant residual resistivity. Recent work suggests slightly different approach to analyze the experimental data.[119] However, once this method was applied on the experimental data, worst fit was obtained and similar criticisms to this results can be done.

Also logarithmic scaling plots of the Hall conductivity are questionable in these materials, though they have been applied successfully to a wide range of materials.[120] In order to demonstrate this point, the resistivity data shown in Figure 5.5(c) in terms of conductivities was replotted, $\log(|\sigma_{xy}|)$ vs. $\log(\sigma_{xy})$ in Figure 5.5(d). As both positive and negative Hall conductivities exists one must plot the absolute values. Since the zero crossing will lead to a divergence in this case, there is no meaning in deriving a scaling exponent α from a relation $\sigma_{xy} \propto \sigma_{xy}^{\alpha}$, anywhere near to the divergence point. At the same time the residual resisitivity ratios are small and thus the range covered in σ_{xx} is far less than ten units, so the local slope is changing strongly leading to unreasonable values of α. In part (d) of this figure, the fit functions used in (c) with dotted lines were also replotted. These functions all approach

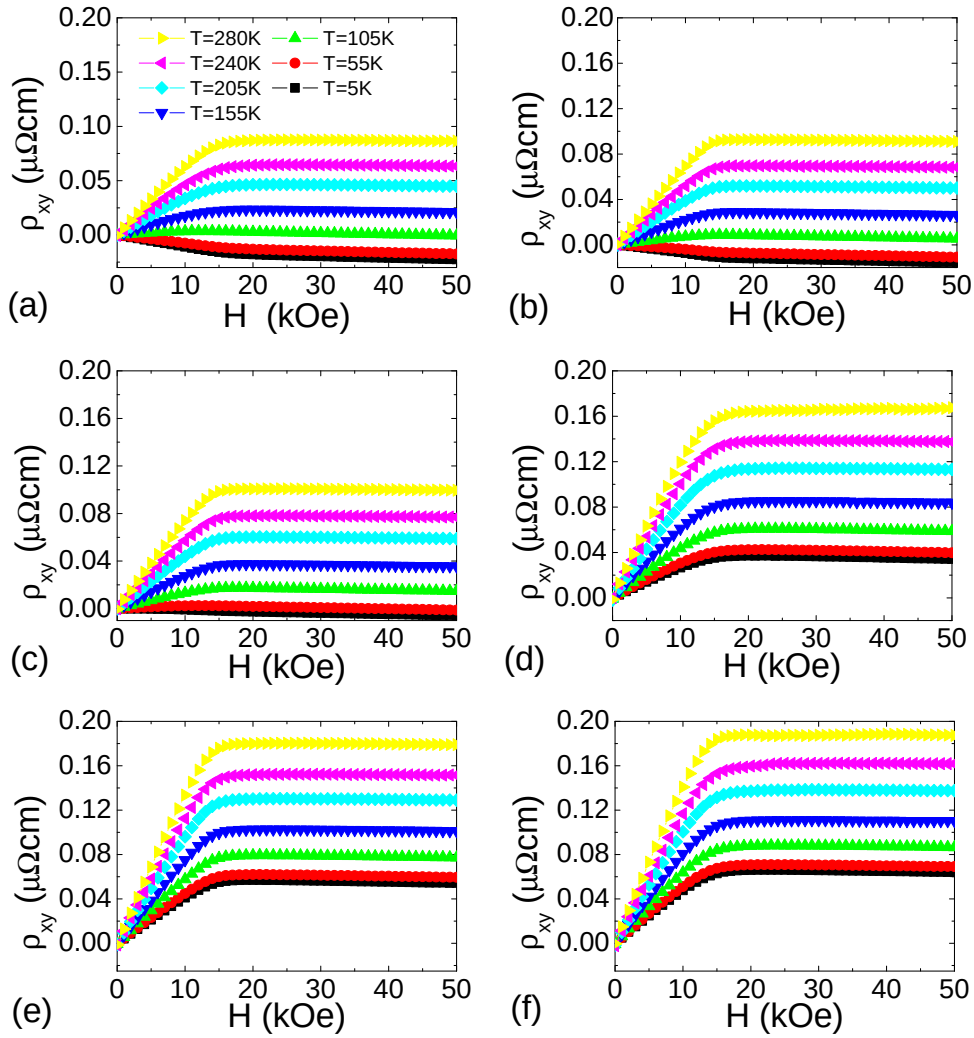

Figure 5.4: Representative set of Hall effect measurements of $Co_2FeSi_{0.6}Al_{0.4}$ deposited at (a) 700 °C, (b) 667 °C, (c) 612 °C, (d) 550 °C, (e) 520 °C, and (f) 480 °C. The legend on (a) indicates the respective measurement temperatures and is also valid for (b)–(f).

asymptotically a straight line of slope one in the scaling plot for high values of σ_{xx}. However this is a mathematical necessity implied by equation (3.14). Extracting a skew scattering parameter from a conductivity regime related to superclean metals is not sensible for the moderately dirty metals used in this thesis. Thus this range containing no real data was shaded, as unphysical in this case.

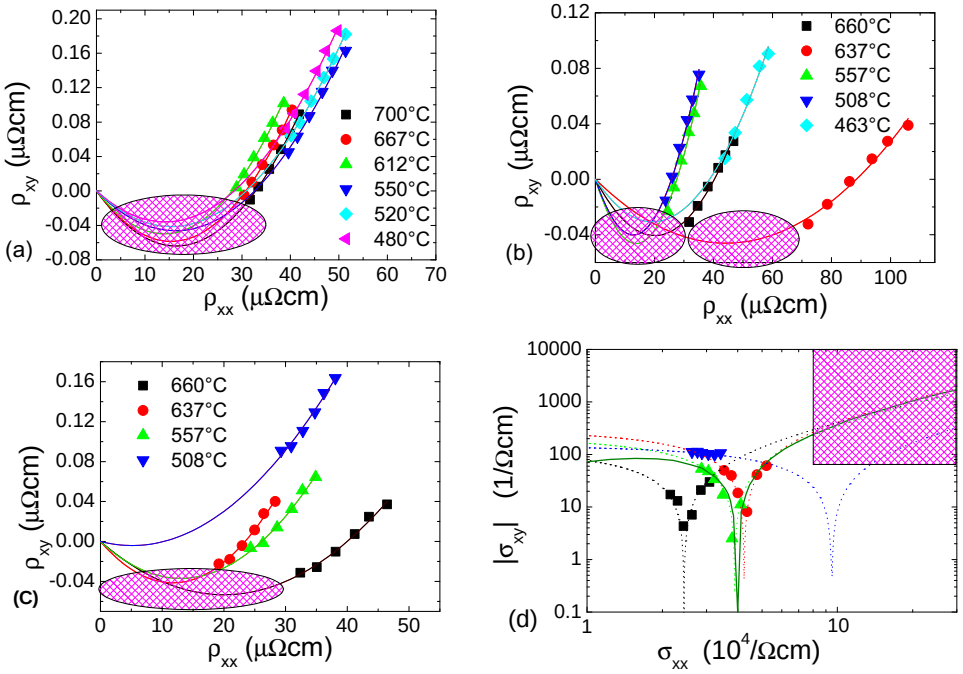

Figure 5.5: Anomalous Hall resistivity ((d) Anomalous Hall conductivity) against longitudinal resistivity ((d) longitudinal conductivity). Each curve corresponds to one sample and consists of the data points extracted from measurements at 5, 55, 105, 155, 205, 240, and 280 K, respectively. In the legend the deposition temperature of each sample is noted ((c) and (d) share the legend). The films are made of (a) $Co_2FeSi_{0.6}Al_{0.4}$ and (b) $Co_2FeGa_{0.5}Ge_{0.5}$ on MgO and (c),(d) $Co_2FeGa_{0.5}Ge_{0.5}$ on Al_2O_3.

Based on Berry curvature effects and scattering a theoretical explanation for the sign change of the AHE has been presented by Kovalev et al.[121] They calculate for a two dimensional Rashba model the AHE in a Keldysh formalism. Their results for attractive impurity potentials are in agreement with the work presented by Onoda et al.[120] distinguishing three distinct regimes: the skew-scattering regime, the disorder independent regime, and the dirty regime. Implementing also repulsive scattering potentials they find a sign change of the AHE. Their numerical solution presented in Figure 10 was digitalized from their article[121] for an impurity scattering potential of strength $mV_0/\hbar^2 = 0.2$. Scaling this two dimensional solution with the layer density ($1/a$, with $a = 0.576$nm) results in the full line in Figure 5.5(d). The agreement of this a priori calculated solution with some of the exper-

imental data in the conductivity scaling plot is astonishing. However, one should keep in mind, that in terms of the resistivites the experimental relation $\rho_{xx}(\rho_{xy})$ is just a straight line, on which correlation is judged on a linear scale. Also for the layer density, the crystallographic unit cell dimension and not the density of atomic planes was taken. While this could be compensated possibly by a different scattering strength, a quantitative comparison with the calculated two-dimensional system should not be performed at the current state. The parameters in the calculated model are adjusted for diluted magnetic semiconductors with a simple band structure, a strong spin-orbit coupling and relatively weak magnetic exchange strength. The Heusler compounds, however, are clearly three dimensional metals with a complex Fermi surface topology, strong magnetic exchange and comparably weak spin orbit coupling. Indeed, an extension of these calculations to a three dimensional system with different densities of positive and negative scattering potentials would be most useful.

As such a calculation is not available, it is discussed in the following the action of different scattering mechanisms explicitely based on the (Hall) resistivities. The splitting of the longitudinal resistivity into a constant and a temperature dependent part leads to a separation of the AHE transverse resistivity in equation 3.14 to

$$\begin{aligned}\rho_{xy}^{AHE}(T) = \rho_{xy0} + (a + 2\sigma^{AH-bj}\rho_{xx0})\rho_{xxT}(T) + \\ + \sigma^{AH-bj}\rho_{xxT}(T)^2\end{aligned} \tag{5.2}$$

where

$$\rho_{xy0} = a\rho_{xx0} + \sigma^{AH-bj}\rho_{xx0}^2 \tag{5.3}$$

The constant ρ_{xy0} is related to temperature independent contributions to the AHE. One will see later that ρ_{xy0} has a positive or negative value depending on the degree of ordering and defect concentration.

This approach allows to separate the temperature dependent parts by subtraction of high (T_h) and low (T_l) temperature data, which results in the following general expression:

$$\begin{aligned}&\rho_{xy}^{AHE}(T_h) - \rho_{xy}^{AHE}(T_l) = \\ &\quad =(a + 2\sigma^{AH-bj}\rho_{xx0})(\rho_{xxT}(T_h) - \rho_{xxT}(T_l)) + \\ &\quad +\sigma^{AH-bj}(\rho_{xxT}(T_h)^2 - \rho_{xxT}(T_l)^2)\end{aligned} \tag{5.4}$$

Depending on the dominance of the skew scattering term "a" ($\sigma^{AHE-skew}$) or scattering independent term σ^{AH-bj} one expects either a linear or a quadra-

tic behavior in ρ_{xxT}. Assuming a dominating skew scattering part, in figure 5.6 the rescaled temperature dependent quantities are replotted and one finds approximately straight lines. In Figure 5.6, the $\rho_{xxT}(T_l) = \rho_{xxT}(50\,\mathrm{K})$ was selected. In order to fit the data, the equation (5.4) was used.

In order to perform a quantitative analysis, it is important to point out that σ^{AH-bj} values are in the range of $\approx 10^{-4}(\mu\Omega\mathrm{cm})^{-1}$. With ρ_{xx0} in the range of $\approx 10^{+1}\mu\Omega$cm the expression $\sigma^{AHE-bj}\cdot\rho_{xx0}$ is $\approx 10^{-3}$. Thus the linear coefficient $(a+2\sigma^{AH}\rho_{xx0}) \approx 10^{-2}$ is dominated by skew scattering parameter 'a' and the observed linear slope was attributed to the skew scattering.

In figure 5.6 a difference between $Co_2FeSi_{0.6}Al_{0.4}$ and $Co_2FeGa_{0.5}Ge_{0.5}$ can be observed. For the first compound all the curves have the same slope. For the second one, the slope has a tendency to increase while the degree of $L2_1$ order decreases. However, this difference between both compounds is not a direct result of the different scattering strength of e.g. disorder of lower mass Al-Si atoms compared to the corresponding disorder of Ga-Ge atoms as the impurity scattering should be temperature independent. Magnon or phonon scattering should be responsible for the temperature dependence. As a magnetic scattering event, magnon scattering is more probably to induce a skew scattering contribution. The importance of magnon scattering in ferromagnetic Heusler compounds is a topic intensively discussed in the framework of tunneling magnetoresistive (TMR) elements. The strong temperature dependence of the TMR is attributed to a strong increase in magnon scattering events and inelastic magnonic features exist in the tunneling spectra.[122,123]

In general, while the band structure of the spin up channel is not strongly changed by introduction of disorder, for the spin down channel disorder results in a shrinking of the gap. In case of $Co_2FeSi_{0.6}Al_{0.4}$ the Fermi energy lies in the middle of the band gap.[42] Therefore, even by introducing some disorder the Fermi energy stays in the middle of the band gap.[44,111] As it was already mentioned, the density of states for $Co_2FeGa_{0.5}Ge_{0.5}$ is not calculated. However, Co_2FeGe is expected to be a true half metal but this is not the case for Co_2FeGa. Now, it is important to remember the discussion presented in relation with $Co_2FeSi_{1-x}Al_x$. It was shown that a systematic tuning of the $Si-Al$ composition in $Co_2FeSi_{1-x}Al_x$, produces a systematic change of the relative position of the Fermi energy in the spin down band. Thus, it is expected that the Fermi energy for $Co_2FeGa_{0.5}Ge_{0.5}$ lies at the bottom of the spin down band gap.[124] If this result is extrapolated, then smaller amounts of disorder might destroy the half-metallic behavior. This might introduce electrons from the spin down channel. The resulting expected change in the topology of the Fermi surface should modify its properties. Thus the spectrum of the magnonic excitations would also change, leading to a different strength of the skew scattering contribution as observed.

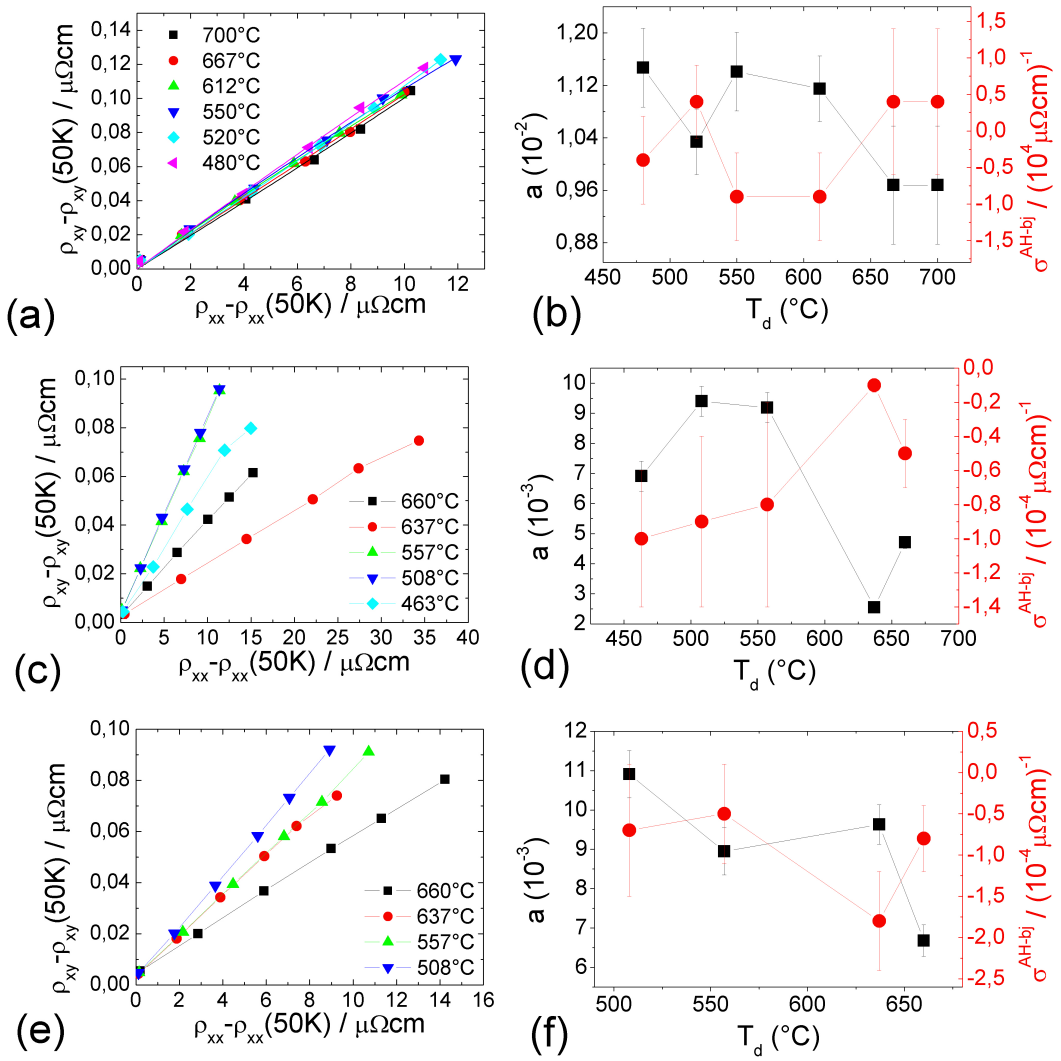

Figure 5.6: Left column: $\rho_{xy}^{AHE}(T) - \rho_{xy}^{AHE}(50\,\mathrm{K})$ against $\rho_{xx}(T) - \rho_{xx}(50K)$. Each point represents data from one temperature curve of figure 5.4. The different lines represent samples deposited at different temperatures as given in the legend. Right column: linear (black squares, left ordinate) and quadratic (σ^{AH-bj}, red circles, right ordinate) fitting coefficients against deposition temperatures. $Co_2FeSi_{0.6}Al_{0.4}$ on MgO (a) and $Co_2FeGa_{0.5}Ge_{0.5}$ on MgO (c) and Al_2O_3 (e).

In a previous work the influence of the relative position of the Fermi energy in the conduction band edge of the minority states was studied, by

changing the iron content in $Co_2Fe_xMn_{1-x}Si$ which resulted in an effective tuning of the Fermi energy position.[125] A systematic shift of the slope, from negative to positive values, was observed in the representation ρ_{xy} versus ρ_{xx}. Results presented in figure 5.6, support the idea that the sign change in the slope is driven mainly by the shift of the effective Fermi energy position inside the minority state band gap. For the samples studied here with $x = 0.5$ fixed, the different degree of disorder can change at most the slope, but not produce a sign change.

For discussion of the temperature independent AHE ρ_{xy0} in equation (5.3), the values measured at 50 K are used. One must keep in mind that the skew scattering parameter "a" was determined quantitatively above for the temperature dependent scattering events. However, the different scattering mechanism leading to the residual resistance will generally be associated with different or even vanishing skew scattering strength. Thus, there is no possibility to determine the parameters straightforwardly as one sample yields only one data point $\rho_{xy0}(\rho_{xx0})$ but there are two parameters. a is the effective skew scattering parameter averaged over different scattering contributions and σ^{AH-bj} combines side jump and Fermi surface contributions for that sample. The general trend one observes for ρ_{xy0} for both compounds is that a positive value at low deposition temperature (high degree of $B2$ disorder) reduces to values close to zero or slightly negative for samples with a high degree of $L2_1$ order. In contrast to a previous work[125] now samples with some degree of DO_3 type disorder were investigated and even stronger negative values were found.

Chapter 6

Magnetic field sensor based on Co_2MnAl

Co_2MnAl is an interesting compound for applications. It only offers a 15 % of spin polarization in the $L2_1$ phase.[45] However, 76 % of spin polarization is calculated at B2 phase.[45] The B2 phase is a disorder phase which can be obtained at lower temperatures than the $L2_1$ phase. Therefore, it is easier to grow Co_2MnAl with higher spin polarization than other Heusler compounds like $Co_2FeGa_{0.5}Ge_{0.5}$.

A Giant Hall Effect, driven by the AHE of Co_2MnAl was already proposed for usage in Hall sensors by Chen et al.[47] They showed only room temperature (RT) data. This pointed out viability of this compound for applications. However, many information was still lacking. For instance, in automotive applications a temperature range well above RT is required in order to place the sensor close to the engine. Also, unchanged properties in the working range would be desirable.

In this chapter, such potential applications of Heusler materials are emphasized by demonstration of a high working temperature. The influence of the crystalline structure on the measured Hall signal will be also detailed as well as showing the efficiency of the material with respect to temperature and magnetic field. It is also convenient to stress commercial details like production cost and durability.

6.1 Sample preparation and characterization

For sample preparation, the attention was focused on finding a range of deposition conditions for materials suitable for sensors. In this case, the deposition parameters were tuned to measure the defect and disorder influence on the

Hall signal as well as the base pressure required to obtain usable sensors. The lower is the base pressure required to obtain the desirable properties, the higher is the money necessary to invest in equipment.

Films of 70 nm thickness were deposited in "clean" and "dirty" conditions: For "clean" conditions an ultra high vacuum (UHV) system with a base pressure of $\approx 1\times10^{-9}$ mbar was used. For "dirty" conditions the UHV system was air exposed prior to each deposition, in order to introduce contaminants. Then, it was pumped to a base pressure of $\approx 4\times10^{-6}$ mbar only (high vacuum regime).

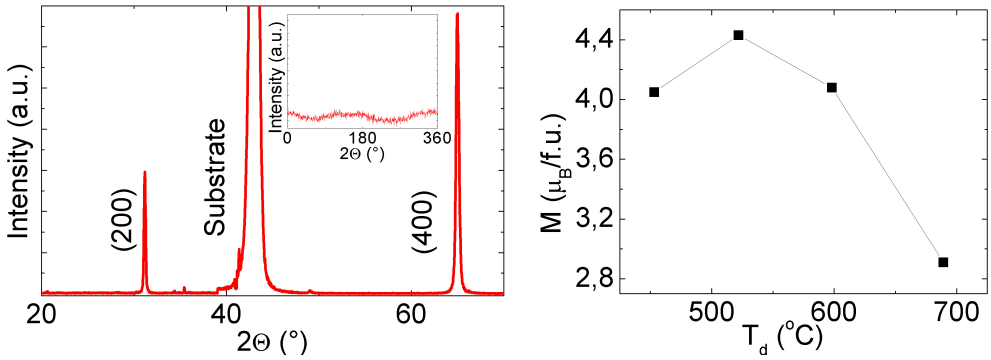

Figure 6.1: left: θ–2θ x-ray diffraction scan of Co_2MnAl deposited at 688 °C on MgO. Inset left shows the corresponding phi-scan of four equivalent {111} reflections. Right: Saturation magnetization for samples deposited at different T_d.

In clean conditions, epitaxial thin films of Co_2MnAl were grown directly onto MgO (100) substrates by radio frequency (RF) magnetron sputtering. Argon at 4×10^{-2} mbar was used as sputtering gas. These samples were deposited at different heater temperatures in a range from 450 °C to 700 °C in order to tune the crystal quality. X-ray diffraction was used to inspect the crystal structure. The presence of a B2 phase was confirmed by measuring its characteristic (200) and (400) reflections (Fig. 6.1(left)). The (111) reflection which is characteristic for the $L2_1$ phase was not found (inset of Fig. 6.1(left)). In general, disorder is connected with the saturation magnetization (M_S).[44] Particularly, Co_2CrAl which is a compound with a similar density of states presents a drop of M_s when increasing the presence of DO3 disorder.[126] On Co_2MnAl bulk samples a M_s of 4.16 μB/f.u. is expected for the B2 phase.[127] By using a SQUID (Quantum Design MPMS II) a maximum value of M_s is measured at 522 °C deposition temperature (T_d) (Fig. 6.1(right)). Correspondingly the maximum amount of B2 phase is expected. Further increase

of T_d leads to the characteristic reduction of M_s due to DO_3 disorder. In "dirty" conditions, thin films of Co_2MnAl were grown directly onto MgO (100) and Si (100) substrates at RT without post-annealing. The absence of (200) and (400) reflections hint to the presence of polycrystalline material with very small grains. A maximum amount of A2 phase is expected for such deposition conditions, which can be easily achieved in an industrial environment.

6.2 Electronic transport measurements

For the transport phenomena measurements, a Hall bar was patterned on each film via ion beam etching using the same procedure as described in the former chapter (figure 5.1). By applying parallel and anti-parallel current and averaging the absolute value of the resulting voltages, the influence of thermovoltages is compensated. To avoid residual magnetoresistive contributions due to misalignment of the contacts, the measurements were accomplished with positive and negative magnetic fields. Transport measurements have been performed using a variable temperature inset in a superconducting magnet below room temperature and in an electromagnet above room temperature, respectively.

The measurements displayed in figure 6.2(a) and figure 6.2(b) were performed at low temperature (5 K) on samples made under clean conditions. They show the dependence of the output signal ρ_{xy} and the normalized sensor linearity $d\rho_{xy}/dB$, respectively, on magnetic field for samples prepared at different deposition temperatures, i.e., with different crystal quality. The size of the output signal with deposition temperature resembles that of the saturation magnetization and one can correlate a high content of the B2 phase with the maximum.

The sensitivity of a sensor will be determined by the achievable response per unit of drive. Thus, the responsiveness was calculated by interpolating a linear behavior between consecutive points in figure 6.2(a) and the slope was extracted. As a final step, the slopes are normalized with the value extracted at lowest magnetic field. The sample deposited at highest temperature, which presents the maximum DO3 phase, presents the best linearity of the signal before magnetization saturation sets in.

Figure 6.2(e) shows the viability of this material for temperatures up to 300 °C keeping the linearity of the response in clean conditions. No drop of the signal is observed in this temperature range, which was restricted by the sample stick. Ultimately the limiting temperature should be the Curie temperature which is about 394 °C for the B2 phase of Co_2MnAl.[127]

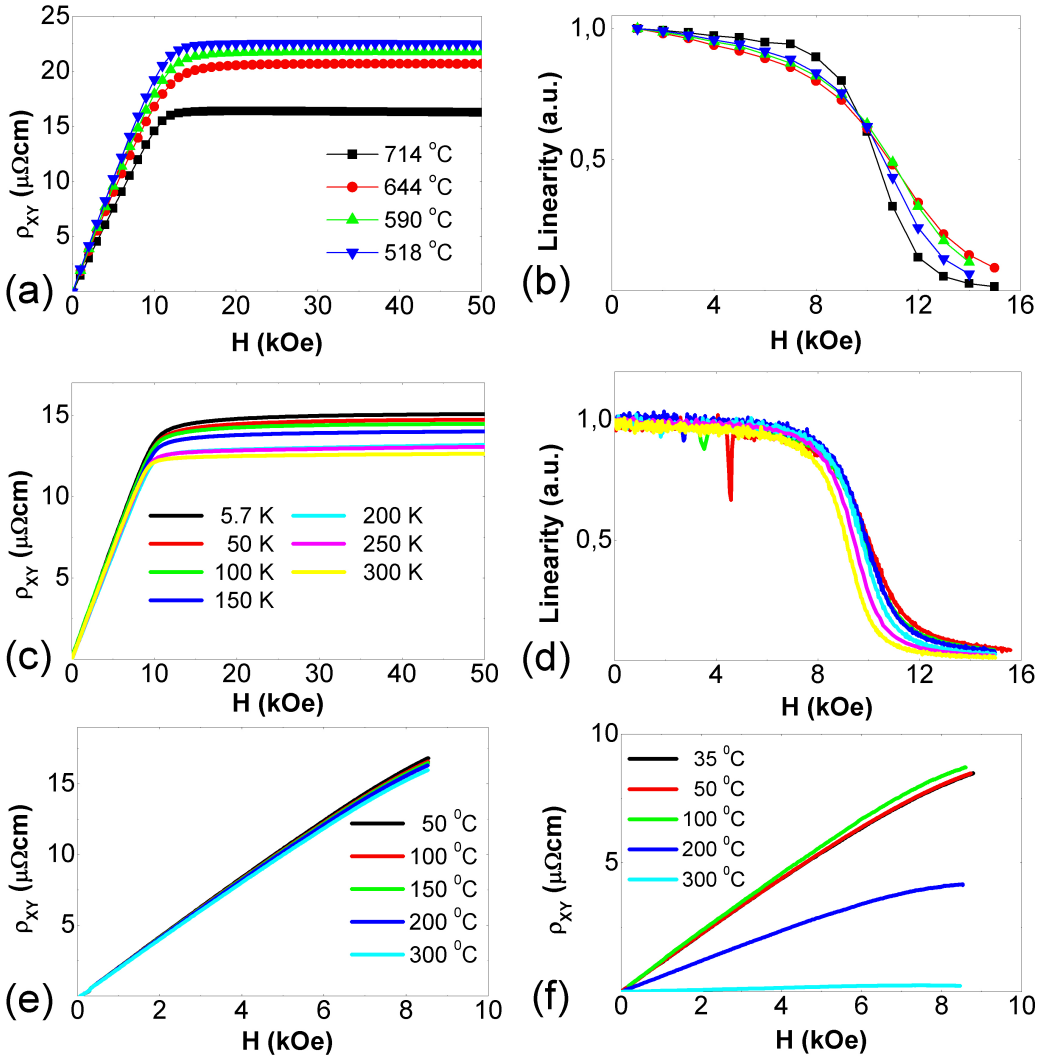

Figure 6.2: The legends on (a) and (c) are valid for (b) and (d), respectively. (a) Hall data at T=5 K for samples deposited at different temperatures under "clean" conditions onto MgO (100). (b) Linearity of the signal in (a) normalized to initial slope. (c) Hall measurements performed at different temperatures on samples deposited at room temperature onto Si (100) under "dirty" conditions. (d) Linearity of the signal in (c) normalized to initial slope. (e) and (f) Hall effect measurements performed in an electromagnet at different temperatures on a sample deposited at 530 °C (RT) in clean (dirty) conditions.

The typical viability of the commercial available Hall effect sensors is from ≈-40 °C to ≈+150 °C. A sensor based on Co_2MnAl, deposited on "clean" conditions, has the potential to extend this range of work considerably.

Figure 6.2(f) presents Hall measurements on samples deposited on "dirty" conditions on Si at high temperatures. They exhibit only a small reduction of the maximum output signal level and linearity for measurement temperatures up to 100 °C compared to films on "clean" conditions. The reduction of the Curie temperature as consequence of the presence of A2 phase and impurities for the "dirty" films is visible in the reduced AHE at high temperatures. However, up to at least 100 °C, they provide a similar level of output signal and linearity. Thus, at low fields, the AHE of Co_2MnAl shows up in a nearly temperature independent linear signal that is robust with respect to deposition conditions and atomic order.

6.3 XPS measurements

For sensor production the effects of surface contaminants and corrosion become important. Therefore, x-ray photoelectron spectroscopy (XPS) measurements at a base pressure of $\approx 10^{-10}$ mbar was performed by using a x-ray source with an Al anode. Two films were prepared under "clean" conditions and deposited at 590 °C. The first sample was air exposed after deposition and stored one week before the XPS analysis. The second one was transferred to the XPS system using a portable UHV system immediately after deposition. The portable UHV system keeps the pressure at $\approx 2\times10^{-8}$ mbar. The sample transferred in such conditions is called "fresh" film.

The analysis of the O1s core level peak for a "fresh" sample reveals a slight oxidation of the sample surface (figure 6.3 left). Two maxima can be recognized. The one corresponding to the lower binding energy might be attributed to the formation of metallic oxides. The maximum at higher binding energy is related to the existence of residual CO_2 contamination.

Once the "fresh" film was analyzed, it was exposed to oxygen with a partial pressure of $\approx 10^{-7}$ mbar during 15 s, 45 s, 6 min, and 11 min and analyzed after each exposition. The behavior of the intensities of O1s core level peaks (figure 6.3 right), after oxygen treatment, reveals a tendency to saturation. Even after 11 min of oxygen exposition, one can recognize the characteristic profile of the Co_2MnAl valence band spectrum (figure 6.3 right). This fact excludes probing depth limitation as reason for the saturation. Thus, only the outermost atomic layers of Co_2MnAl are oxidized. The top oxidized layer caps the film and keeps its major bulk volume protected against further contamination. Even the air exposed film shows still features of the metallic

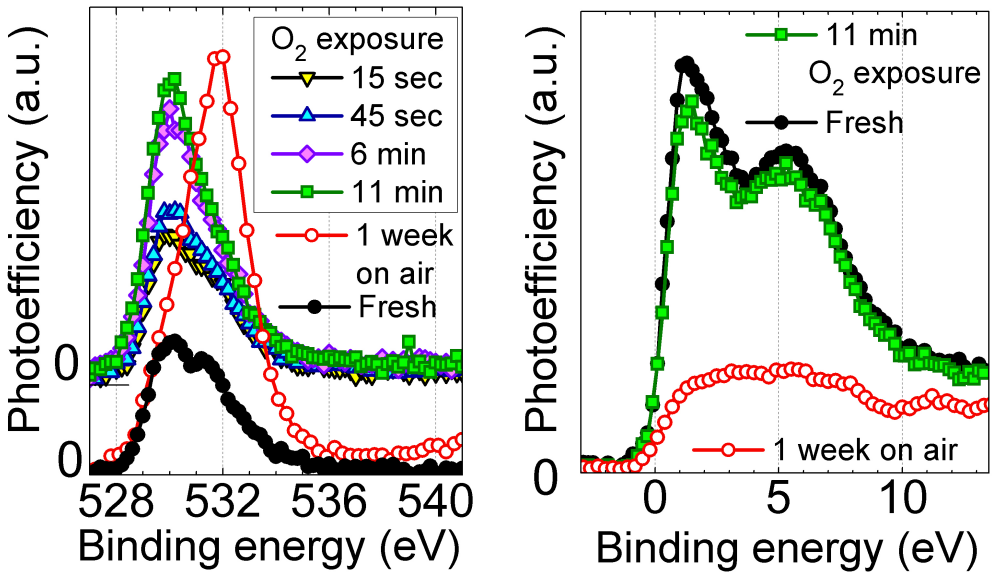

Figure 6.3: Left and right are the photoelectron emission spectra in the range of O1s peak and valence states, respectively. The measurements were performed at 19 °C with an excitation energy of 1486.6 eV.

Co_2MnAl valence band, especially a Fermi edge (figure 6.3 right). Hence, the thickness of the contaminated Co_2MnAl layer does not exceed the probing depth (≈ 2 nm) of the used XPS technique. A shift of the O1s peak maximum to higher binding energies (figure 6.3 left) indicates a binding of complex oxygen containing molecules from air onto the film surface.

6.4 Analysis of the potential sensor

A drawback of a Hall sensor based on Co_2MnAl is the loss of energy through heat in the highly resistive Heusler compounds with specific resistivities of the order of $\approx 100\,\mu\Omega$cm at RT. The dissipated power is proportional to the square of the current and the longitudinal resistance. As the longitudinal resistance is proportional to the length to width ratio for a certain thickness, a Hall sensor should have a small length to width ratio. This can be easily achieved by shunting the Heusler film with a highly conducting cover layer everywhere aside from the actual Hall bar. For very small length to width ratios, however, the cover electrode will short the Hall signal. Thus it will be necessary to optimize the ratio in order to obtain the maximum hall signal for a given dissipated power density.

Further engineering of sensors based on Co_2MnAl is still required. The advantage with Co_2MnAl lies on its linear behavior in a wide range of temperatures. It might be possible to protect the compound against corrosion by a short pure oxygen exposition which should result into an extension of its life time. In addition, it can be deposited on different substrates and conditions keeping its Hall response.

Chapter 7

Optical measurements

7.1 Magneto-Optic Kerr Effect (MOKE)

In 1877 John Kerr discovered the magneto-optic Kerr effect. Nowadays, this technique is widely used to characterize magnetic thin films and explore their properties like magnetic anisotropy and magnetization reversal. By using a laser focused on the surface of the sample, the technique is capable to map the magnetization of the sample and to study magnetic domains.[128] In literature, it is frequent to find the names LMOKE, PMOKE and TMOKE. These names refer to the direction of the magnetization vector of the sample in relation with the incidence plane and the reflecting surface. The labels L, P and T mean Longitudinal, Polar and Transversal, respectively. It is also possible to find QMOKE which correspond to measurements of the quadratic contribution of the MOKE signal G_{ijkl} (eq. (7.1)).

In a first rough approach, MOKE can be described as a change of the light polarization and intensity due to an interaction with a magnetic medium. In this case, the light is produced by a laser beam which interacts with a ferromagnetic half metallic thin film. In LMOKE geometry, an incoming linear polarized beam of light becomes elliptically polarized. The change results from the interaction between the light and the electrons and can be quantized in the dielectric tensor.[129] Originally, the effect in ferromagnets was larger than expected. This discrepancy was explained by Hulme[130] after the introduction of the Heisenberg model for magnetism. At the microscopic level, the shift of polarization results from the spin orbit coupling which makes the coupling of the light electric field and the spin of the electron in a magnetic medium possible. This interaction is computed in the off-diagonal terms of the dielectric tensor[129] and its components can be written

as follows[131]

$$\begin{aligned}\varepsilon_{ij} = \varepsilon_{ij}^0 + (\frac{\partial \varepsilon_{ij}}{\partial M_k})_{M=0} M_K + \frac{1}{2}[\frac{\partial^2 \varepsilon_{ij}}{\partial M_k \partial M_l}]_{M=0} M_k M_l + ... = \\ = \varepsilon_{ij}^0 + K_{ijk} M_k + G_{ijkl} M_k M_l,\end{aligned} \tag{7.1}$$

where $\varepsilon_{ij}^0 = \varepsilon_{ji}^0$ are the zero order components of the tensor which are independent of the magnetization. K_{ijk} are the linear components of the tensor and G_{ijkl} are the quadratic components.

In principle, one would expect a vanishing contribution for the quadratic term. However, Ni-Fe bilayer systems and Fe films have shown a measurable quadratic contribution.[132–135] Especially interesting are the Co-based Heusler compounds. Most of them have shown a strong quadratic effect.[136] The case of Co_2FeSi is remarkable. It presents the largest quadratic MOKE signal.[137] By using $Co_xFe_yGa_z$, a dependence of the quadratic-MOKE signal with the composition was found. A possible explanation was suggested regarding to the strong dependence of magnetic properties of the Heusler compounds with the crystalline structure.[136,138] Following this reasoning, Trudel et al.[139] studied thin films of $Co_2FeSi_{0.5}Al_{0.5}$ annealed at different temperatures. This process implies the change of the crystalline phase and in consequence a change in the magnetic properties of the Heusler compounds. They found a correlation between the ordering of the crystal structure and the quadratic-MOKE signal. They also claim that the ordering has a higher contribution than the spin-orbit coupling and the orbital moment. Wolf et al[140] performed further experiments in this direction. They use thin films of Co_2MnSi annealed at different temperatures and claim a link between the $L2_1$ ordering and the quadratic-MOKE signal.

In this work, $Co_2FeSi_{0.6}Al_{0.4}$ was used to grow thin films with different crystal qualities. This compound is slightly different to the one used in the work presented by Trudel et al.[139] By doing this one can explore differences due to the composition and to the deposition procedure. $Co_2FeGa_{0.5}Ge_{0.5}$ was also studied in order to gain further insight into the relation between ordering and the MOKE signal. The measurements presented were performed by Georg Wolf (AG Magnetismus) in the Technische Universität of Kaiserslautern.

7.2 Sample preparation and setup

In chapter 5, the preparation process of $Co_2FeSi_{0.6}Al_{0.4}$ and $Co_2FeGa_{0.5}Ge_{0.5}$ films is described in detail. As it was already mentioned, during the de-

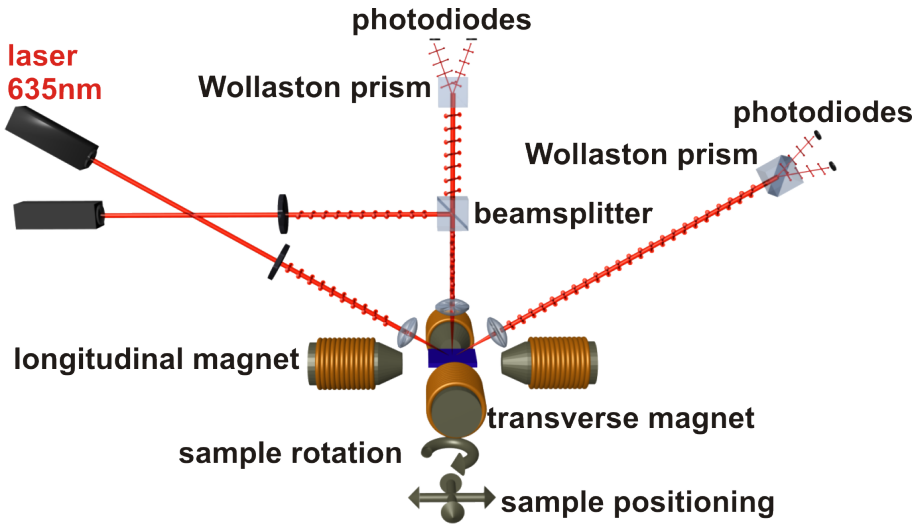

Figure 7.1: Dual-beam MOKE magnetometer.[141]

position process two substrates were used simultaneously. The first one (10 ×10 mm) was etched and used to measure transport properties. The second one (10 ×5 mm) was used to determine the crystal structure carefully and to measure the saturation magnetization. In order to perform the MOKE measurements, these second samples were sent to Technische Universität of Kaiserslautern. Thus, we complemented the information already obtained from the transport measurements.

In the basic MOKE setup, only a source of light, the appropriate polarizer, the magnetic medium and the detector are required. The setup used to perform the measurements is presented in figure 7.1 and it allows to obtain data of MOKE and QMOKE simultaneously . A detailed description of the setup and its working procedure can be found in different articles.[140,141] In order to fix the reference i.e. to establish the 0°, one has to consider the plane, which contains the incident and the reflected beams. The position 0° and 180° is marked, when the defined plane is parallel to the long side of the substrate.

7.3 MOKE measurements

A2, B2, DO_3 and $L2_1$ are the different ordered phases in which the Heusler compounds crystallize. These phases are corresponding to cubic structures. Without further considerations, one would expect for a representation of coercive field against angle of measurement in a polar scan a fourfold symmetric

curve. However, the situation is richer than just considering structural factors.

One can start considering the possible influence of the intrinsic contributions to the magnetic anisotropies. As it was already mentioned, the magnetic properties of Heusler compounds are strongly related with atomic order. The Heusler compounds become ferromagnetic through the orbital hybridization which depends on the ordering. Therefore, it is reasonable to expect larger anisotropy constants by going from B2 to $L2_1$ or from DO_3 to $L2_1$. Qualitatively, one can also expect larger anisotropy constants for heavier compounds. The magnetic anisotropy has its source in the spin orbit coupling and it is a function of the atomic number. Therefore, the higher the atomic number is the higher is the expected contribution from the spin orbit coupling.

In addition, extrinsic contributions play a relevant role, even a key role. For instance, it is well known for permalloys that it is possible to tune the direction of the magnetic easy axis during the deposition process by placing a magnetic field. Moreover, other extrinsic sources have to be considered like, film morphology, dislocation lines, grain boundaries, magnetic field from the cathode, temperature gradients during the growth process or lattice stress.

Figure 7.2 shows rotational scans of LMOKE measurements. This measurements were performed to characterize the anisotropy distribution of the thin films. For these samples, the hysteresis curves were taken each 2°. In the polar plots 7.2 a correlation between the coercive field and the deposition temperature is visible. The figures 7.2 a) and b) correspond to $Co_2FeGa_{0.5}Ge_{0.5}$ and the c) and d) to $Co_2FeSi_{0.6}Al_{0.4}$. The figure 7.2 a) (figure 7.2 c)) shows the evolution of the biaxial (uniaxial) behavior to an isotropic one as function of the temperature. The plot 7.2 b) shows a pronounced biaxial behavior whereas in d) the uniaxial behavior is not well defined.

In order to skip from the main discussion the artificial effects, one has to note the step in the data visible around 0° on figures 7.2 c) and d). This sharp jump on the data might be attributed to a miss step of the stepper motor which rotates the sample with the axis normal to the substrate. The individual curves, from where the data of the coercive field is extracted, show a rich behavior with double steps. This data is evaluated automatically by a program. This evaluation is dependent on how the program establishes the offsets. That might result in a systematic introduction of errors. Concluding this point, the sharp jump mentioned is taken as an artificial effect.

In former chapters, the crystalline structure for $Co_2FeSi_{0.6}Al_{0.4}$ (fig. 5.2 right) and $Co_2FeGa_{0.5}Ge_{0.5}$ (fig 4.9) has been explored. The residual resistivity for these compounds was also studied (fig.5.3). The data indicates a maximum degree of $L2_1$ order for deposition temperatures around 600°C.

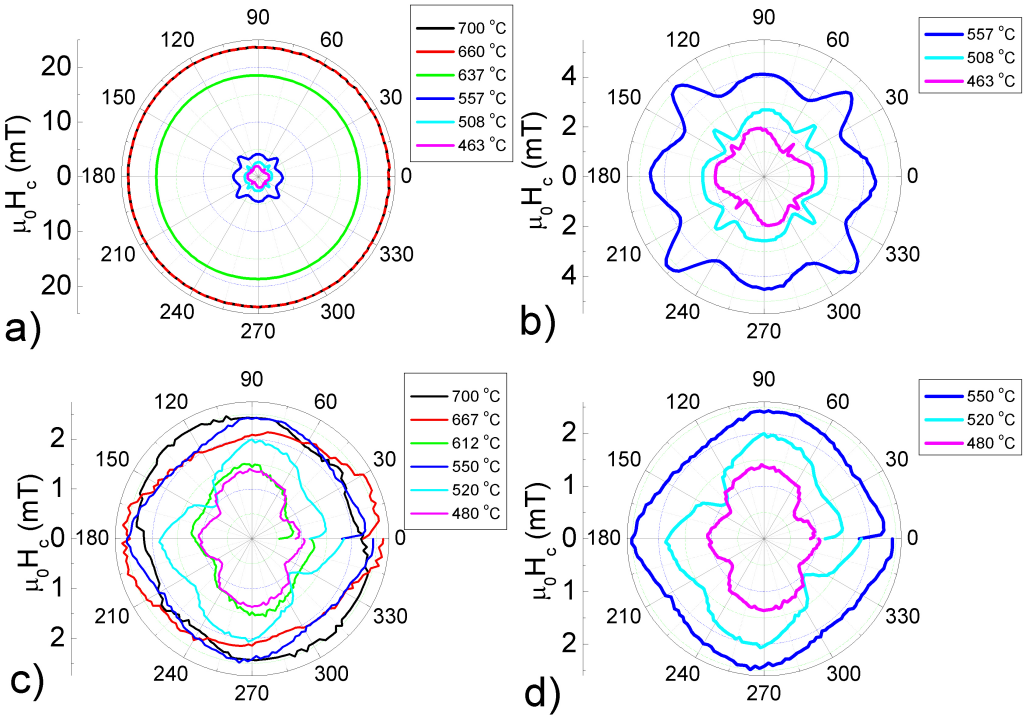

Figure 7.2: Polar plots of coercive field for films deposited at different temperatures. Upper for $Co_2FeGa_{0.5}Ge_{0.5}$ and lower for $Co_2FeSi_{0.6}Al_{0.4}$. In order to make the data more visible, the three most inner polar plots on figure a) and c) have been replotted on b) and d), respectively.

Therefore, the highest intrinsic contribution should arise around 600°C. However for both samples, at this temperature, the data reveals an isotropic behavior. It is even difficult to easily recognize a symmetric behavior for $Co_2FeSi_{0.6}Al_{0.4}$. This suggests, that the coercive field is strongly influenced by extrinsic contributions. Even more, the extrinsic contributions are dominating around 600 °C.

In figure 7.2 d) ($Co_2FeSi_{0.6}Al_{0.4}$), the fourfold symmetry is hardly distinguishable. However, the symmetry is clearly observed in figure 7.2 b) ($Co_2FeGa_{0.5}Ge_{0.5}$). Qualitatively, the difference might be explained in terms of larger magnetic anisotropy constant for $Co_2FeGa_{0.5}Ge_{0.5}$. The elements Ga and Ge are heavier than Al and Si. Thus, in $Co_2FeGa_{0.5}Ge_{0.5}$ the effect from spin orbit coupling is expected to be larger.

Discussion in terms of extrinsic effects which are not controlled might result speculative. However, all the samples were prepared in the same chamber. The samples studied by MOKE were deposited on MgO substrates, which came from the same company. The cathodes have the same magnetic configuration and they also originated from the same company. As well, it seems reasonable to expect that most of the extrinsic contributions influence the samples in the same fashion. In addition, x-ray analysis does not reveal significant differences in the grain size. On the other hand, temperature gradients can act differently. The samples were deposited at different temperatures. Through the AFM pictures (fig. 4.3), one can see that the roughnesses of the films increase systematically with higher deposition temperatures. As it is pointed out in chapter 4 the increase of the deposition temperature produces larger structures. At the higher temperatures, the features break down in a columnar structures. The columns can reach as deep as the film thickness. In this final state, the space between columns can act as micro scratch uniformly distributed in the film, which could lead into the formation of random oriented magnetic domains. This has to sum up in an isotropic distribution of the coercive field.

Unpublished[142] data support this idea. $Co_2FeSi_{0.6}Al_{0.4}$ was deposited on MgO using different buffer layers. The films were grown at room temperature and post-annealed at ≈ 550 °C. This procedure is used frequently on the fabrication of MTJ to improve the epitaxial growth and the surface of the interfaces. In general, the consequence observed in the coercive field is better defined anisotropic behavior. The polar plots, for samples deposited directly on MgO and for samples with a buffer layer of MgO are similar to the ones published by Trudel et al.[139] By using double buffer layer, Cr on top of MgO, the fourfold symmetric behavior appears.

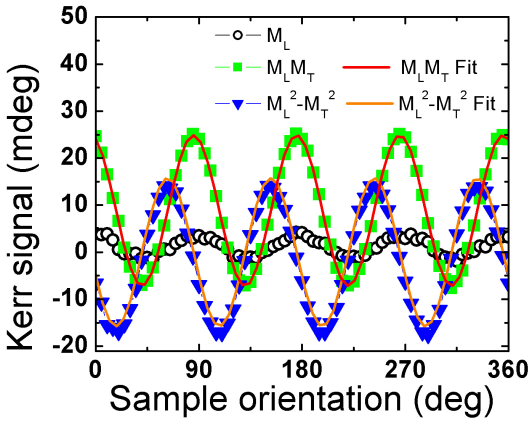

Figure 7.3: Example of splitting of the QMOKE contributions as a function of the sample orientation. Black circles represent the part proportional to M_L. Green squares represent the part proportional to $M_L \cdot M_T$. The blue triangles represent the part proportional to M_L^2-M_T^2. The lines are the fit according to the used model.[132] The data correspond to $Co_2FeSi_{0.6}Al_{0.4}$ deposited at 588 °C.

7.4 QMOKE measurements

The QMOKE signal is more related to intrinsic material properties. It arises from the second order effect on the spin orbit coupling interaction. Therefore, an evolution of the crystalline phase has to have an influence on the QMOKE signal. In consequence, the extrinsic contributions due to anything related with interaction or formation of magnetic domains can be skipped from the discussion.

The method used to extract and analyze the QMOKE signal is explained in many articles.[132,139,140,143,144] For soft magnetic thin films, the Kerr signal can be expressed as a sum of three terms.[132] They are proportional to M_L, $M_L \cdot M_T$ and (M_L^2-M_T^2). M represents the magnetization. The indices L and T mean Longitudinal and Transversal, respectively. The polar component is neglected. This component refers to the out of plane magnetization. The longitudinal magnetization is defined parallel to the plane, which contains the incident and the reflected beam. The transversal magnetization is defined transversal to the former plane.

In figure 7.3, one can see the typical result which arises from the analysis of the Kerr signal. The signal proportional to M_L has almost vanished. This can be achieved by aligning the incident beam perpendicularly to the surface. In this situation the incident beam is perpendicular to the magnetization.

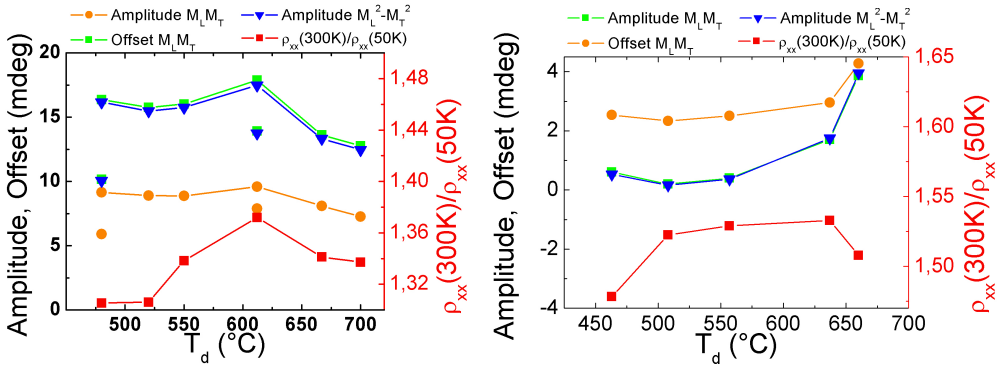

Figure 7.4: For both plots, the left Y axis is the QMOKE amplitude. The left plot corresponds to $Co_2FeSi_{0.6}Al_{0.4}$ and the right corresponds to $Co_2FeGa_{0.5}Ge_{0.5}$. The points represent samples deposited at different temperatures. Orange circles and green squares represent the offset and the amplitude of the term proportional to $M_L \cdot M_T$. Blue triangles are the part proportional to M_L^2-M_T^2. The right Y axis represents the residual resistivity. The red squares and lines are the data for residual resistivity.

Therefore, the first order of the spin-orbit interaction energy is zero[145] and the signal has to origin from the quadratic contribution.

In figure 7.4 (left axis), the different contributions to the QMOKE signal are plotted against deposition temperature. On the right axis, the residual resistivity is plotted for each partner sample. Wolf et al.[140] showed an increase of the QMOKE signal with the annealing temperature for Co_2MnSi. The samples were post annealed at different temperatures and the highest temperature was 500 °C. $Co_2FeSi_{0.6}Al_{0.4}$ reproduces this behavior up to ≈ 600 °C. The isolated points on figure 7.4 (left) represent single samples of $Co_2FeSi_{0.6}Al_{0.4}$ used to check the reproducibility of the data. They are not resulting in the same absolute values. However, the same trend is present.

By comparing the QMOKE signal with the residual resistivity a correlation arises between them. One can clearly see the correlation in case of $Co_2FeSi_{0.6}Al_{0.4}$. The sample deposited around 600 °C shows a maximum in QMOKE contributions. At this temperature, the plot of the ratio I_{111}/I_{200} against temperature has a maximum. This maximum also matches with the maximum in residual resistivity. Therefore, the most ordered crystalline structure is expected for this temperature. Note, for the lowest temperature, one observes an increase of the QMOKE signal. This series of films are expected to present the maximum A2 structure at the lowest temperature. If one expects a straight forward connection between ordering and QMOKE signal, the plot would have to show lower values of QMOKE for higher values

of A2. However, it happens the other way around.

The left axis of figure 7.4 (right), represents the contributions to the QMOKE signal for $Co_2FeGa_{0.5}Ge_{0.5}$ and in the right axis the residual resistivity for each partner sample. In this case the situation is more complex. For the lowest temperature, the increase observed for $Co_2FeSi_{0.6}Al_{0.4}$ is present in $Co_2FeGa_{0.5}Ge_{0.5}$, too. At the three medium temperatures, the trend present in the residual resistivity is reproduced by the QMOKE signal. Finally, at the highest temperature, residual resistivity and QMOKE behave in opposite direction. The lowest and the highest temperatures correspond to an increase of the A2 and DO_3 phase, respectively. This increase in the disorder is reflected in the x-ray measurements and in the residual resistivity.

Such observation reinforce the idea that the QMOKE signal is connected with the intrinsic material properties.[140] However, it seems not as straight forward connected with the ordering phase as the resistivity.[102] One might note that for the highest content of DO_3 phase a decrease of the QMOKE contributions for $Co_2FeSi_{0.6}Al_{0.4}$ and an increase for $Co_2FeGa_{0.5}Ge_{0.5}$ is measured. In consequence more effort is required to understand the connection between ordered phase and QMOKE.

Chapter 8

Magnon-driven spin Seebeck effect

In 2008, the spin Seebeck effect (SSE) was detected for the first time by Uchida et al.[4] This phenomenon is situated within the framework of spincaloritronics. It allows the conversion of a heat current into a spin flow, which finally is detected via the inverse spin Hall effect. The SHE depends on the spin orbit coupling, which is a function of the atomic number. Therefore, it is convenient to use a good a conductor with a high Z number. Platinum fits with these conditions.

As already mentioned in chapter 3, the explanation for the SSE has evolved in the past years. At an early stage, it was argued in terms of different Seebeck coefficients for the different spin channels. In this context, the Heusler compounds were excellent candidates to observe the SSE due to their potentially large spin polarization. Bosu et al.[146] recently published measurements of SSE on Co_2MnSi. However, the explanation had a weakness in the spin flip length. This length is too short compared with the size of the sample used in the experiments. Finally, it was formally demonstrated the impossibility to explain the SSE via different Seebeck coefficients for each spin channel.[85]

Subsequently, the source of the SSE was attributed to the spin injection mediated by magnons (MSSE).[84] The heat bath communicates energy to the phonon system within the ferromagnetic medium so that the phonons can excite magnons. The magnons can propagate in the sample and this propagation distance is compatible with the length of the sample. On the interface ferromagnet/Pt, the magnons lose torque producing the spin injection in the normal metal. Due to this new explanation, it was decided to include a permalloy $Ni_{80}Fe_{20}$ in the research. Finally, the original experiment was tried to be reproduced.

To detect the MSSE is a challenging issue. One has to consider the experimental similarities with the Nernst effect and the planar Hall effect. The signal from both these effects can mask the contribution from the MSSE. In this chapter, the different experimental conditions are described in detail.

8.1 Sample characterization and preparation

To perform these experiments, a 20 nm ferromagnetic (Heusler or permalloy) thin film was prepared and capped with 10 nm of platinum. The films were deposited on 10×15 mm MgO and Al_2O_3 substrates.

Following the explanation based on different Seebeck coefficients for each spin channel, Co_2MnAl, $Co_2FeGa_{0.5}Ge_{0.5}$ and $Co_2FeSi_{0.6}Al_{0.4}$ were deposited using different deposition parameters. They were already optimized to obtain the maximum $L2_1$ order in the structure. Therefore, the optimum deposition conditions obtained from previous experiments (see, chapter 5 and 6) were reproduced. Additional samples were deposited at temperatures slightly higher and lower ($\approx 100\,^{\circ}C$) to cover the range of temperatures were the samples have shown the maximum ratio (111)/(200).

In the case of $Ni_{80}Fe_{20}$, the goal was to reproduce the original experiment, considering the explanation based on magnon propagation. Permalloys have been widely studied during the last century and several groups reported low damping values ($\alpha \approx 0.01$) for samples deposited by magnetron sputtering with an argon pressure between 1×10^{-2} mbar[147] and 1.5×10^{-3} mbar.[148] The best result offered by Nahrwold et al.[147] corresponds to a sample deposited at room temperature. Therefore, it was not important to grow epitaxial thin films with a high crystalline quality. The relevant parameter was the magnetic damping. In addition, it was desirable to obtain a smooth interface $Ni_{80}Fe_{20}$-Pt to avoid interface effects.

The deposition conditions were tuned to get low magnetic damping and smooth surfaces at the same time. A set of ≈ 20 nm thick samples was deposited at room temperature and different argon pressures. DC-magnetron sputtering at 50 mA was used.

Figure 8.1 shows results of measurements performed in a VSM setup. One can see no significant difference in the curves resulting from the measurements on different samples. They present similar magnetization saturation and coercive fields. The sample deposited at 0.2×10^{-2} mbar shows the highest magnetization saturation value. However, the value is similar to one measured on the sample deposited at 2.58×10^{-2} mbar.

In addition a sample was deposited at 0.25×10^{-2} mbar and 450 °C in order to check the influence of the deposition temperature. The yellow curve in

figure 8.1 shows an increase of the coercive field and a reduction of the magnetization saturation compared with the sample deposited at 0.2×10^{-2} mbar and at room temperature. In principle, this difference would not lead to a significant change in the expected MSSE signal.

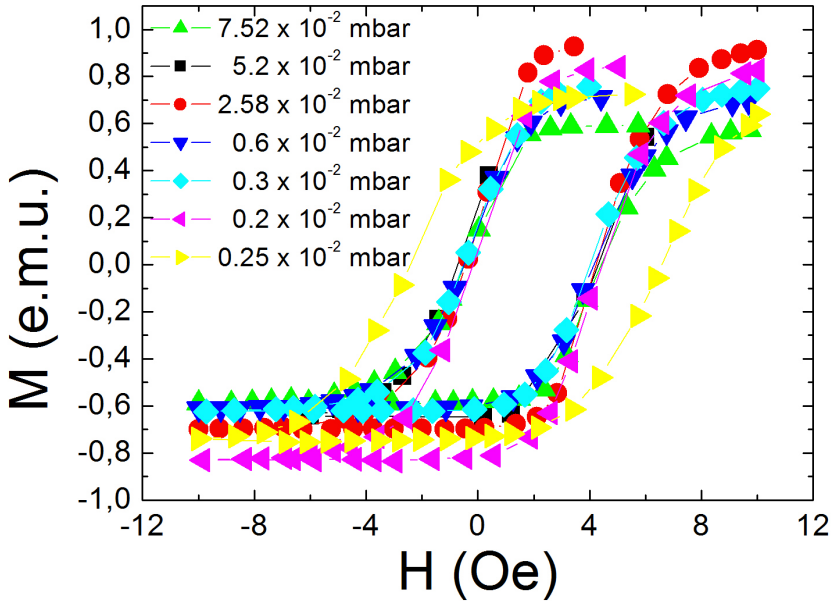

Figure 8.1: Magnetization hysteresis loops result of $Ni_{80}Fe_{20}$ thin films deposited at different pressures. The yellow curve belongs to a measurement of a sample deposited at 450 °C. The other measurements belong to samples deposited at room temperature.

Since the measurements of the magnetization saturation did not reveal enough information to determine the optimum growing conditions, the samples deposited at 0.2×10^{-2} mbar and 0.3×10^{-2} mbar were delivered to the AG Magnetismus group in the "Technische Universität Kaiserslautern" to measure the magnetic damping constant α. It resulted in $\alpha = 0.01$ and $\alpha = 0.019$ for the samples deposited at 0.2×10^{-2} mbar and 0.3×10^{-2} mbar, respectively. Both measurements have an error of 10 %.

Therefore, $Ni_{80}Fe_{20}$ samples were deposited by DC magnetron sputtering ($\approx$ 296 V and 50 mA) at room temperature and an argon pressure of 0.2×10^{-2} mbar where they showed the lowest magnetic damping value.

The 10 nm platinum layer was deposited by DC magnetron sputtering (50 mA) at room temperature. In order to minimize the time that the fer-

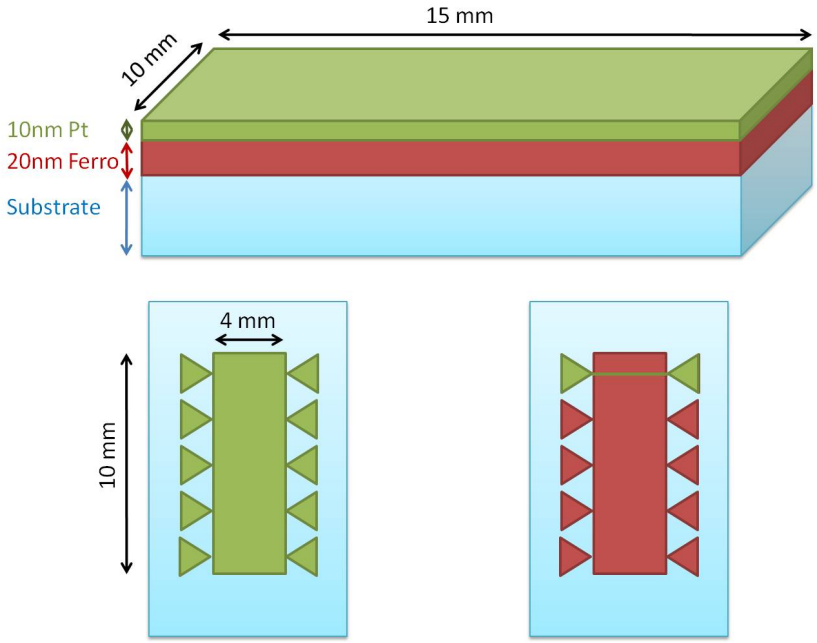

Figure 8.2: Upper figure, thin film resulting from the deposition procedure. Lower left, first etching step. Lower right, second etching step.

romagnetic material was uncapped, the pressure set for the underlying material was also used to deposit the platinum. By using this procedure, the contamination with residual oxygen, carbon dioxide or other elements was minimized.

The final shape of the samples consisted in a 20 nm thick and 10 ×4 mm wide ferromagnetic layer. On top was a 4 mm long, 10 nm thick and 100 μm wide platinum wire (fig. 8.2 right).

In order to define this structure, a two step lithographic process was followed. In the first step the general geometry was defined. The shape was selected to minimize the effect from the misalignment of the contacts (fig. 8.2 left).

The second step consisted of removing parts of the 10 nm platinum layer and only the wire plus the contacts of the wire remains on the film (fig. 8.2 right). To remove this 10 nm thick platinum layer a 10 nm thick platinum sample was deposited to use it as reference in the etching process.

In this second step, the reference sample was glued on a holder, which allowed to contact the reference. Afterwards, it was connected to a voltmeter. By doing this, it is possible to measure in situ the resistance of the reference sample, while the etching process took place. Next to the refer-

ence sample, the structured film was glued. Finally, the etching step was performed. When the measurement of the platinum resistance was in the range of mega ohms, the etching process was stopped. AFM measurements confirmed a thickness of the wire of 10 nm and EDX measurements confirmed the absence of platinum in the etched region.

The etching process had one inconvenience. While the samples were cleaned after each etching step, some silver particles from the silver glue used to fix the sample to the holder were deposited on the film surface. The silver glue contamination was eliminated by fixing the substrates to the holder mechanically instead of gluing. By doing this, clean surfaces were obtained and the process required less time.

The anisotropy of a $Ni_{80}Fe_{20}$-Pt sample resulting from the etching process, as described above, was investigated. The angular dependence of the coercive field was measured (fig. 8.3). The values at 0° and 180° could be compared with the values resulting from the VSM measurements (fig. 8.2). One has to keep in mind that with the VSM the whole volume of the thin film was measured while with the LMOKE just the illuminated region was investigated. The VSM gave $H_c \approx 4$ Oe and LMOKE $H_c \approx 7.5$ Oe. Both results are in the same order of magnitude. The difference is only ≈ 3.5 Oe. If the sample would have one magnetic domain, one would expected to observe an easy axis parallel to the long side of the substrate. However, a hard axis was measured in this direction (fig. 8.3). An important factor to understand this result is the laser spot size. The diameter was $\approx 200\,\mu$m and it was focused on the center of the sample. Due to the magnetic domain distribution, it is possible to find different magnetization directions in different positions.

The coercive field and the magnetic damping of the mentioned permalloy thin films is compatible with the values achieved by different groups.[147,148] Therefore, the optimum conditions to grow permalloy with the desirable behavior were obtained.

8.2 Experimental setups

For this experiment two setups have been prepared, one for room temperature and one for low temperatures. Both setups shared the same main parts. In order to perform the MSSE measurements, it is required to establish an in plane temperature gradient. Two copper blocks were used, for this purpose. One acts as a warm side. In this copper block one can place a heater and a Pt-100 resistance to measure the temperature. The other one acts as a cold side. In this case, for the room temperature setup, it was only possible to place a Pt-100 resistance. For the low temperatures setup, it was possible to

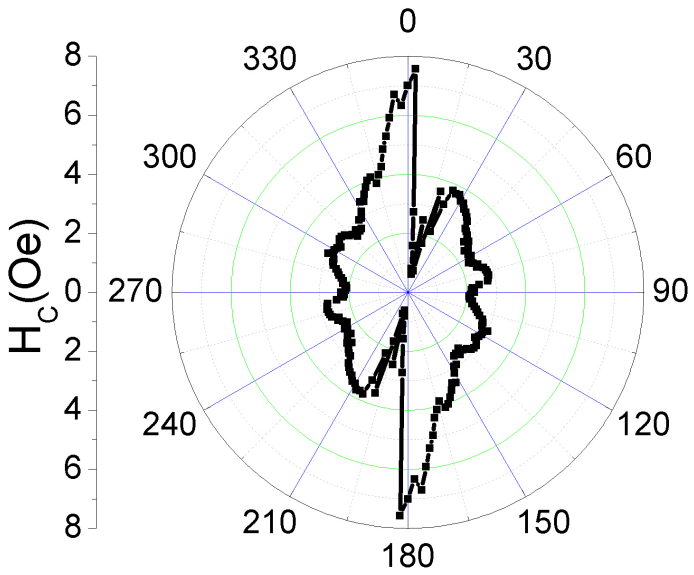

Figure 8.3: Angular dependence of the coercive field measured on a structured $Ni_{80}Fe_{20}$ sample. Long side of the 10×15 mm substrate parallel to the direction 0°-180°.

place a heater and a Pt-100 resistance. This allowed us to invert the gradient transforming the cold side in a warm side and vice versa. To avoid parasitic thermo-current, platinum wires of 0.05 mm diameter were used to measure the signal. To obtain a structurally stable setup, the two copper blocks were connected by a teflon piece.

In case of the room temperature setup, the magnetic field parallel to the sample surface was provided by an electromagnet. The cooling system of this electromagnet was used to cool down one copper block and establish the temperature gradient. Additionally, the electromagnet poles also clamped the setup fixing its position (fig. 8.4 left). The magnetic field was measured by a Hall probe.

For the low temperature setup, superconducting coils were used to apply the magnetic field. The Helium environment served for keeping the temperature of one of the copper blocks colder than the other one. The setup was mounted on two platforms (fig. 8.4 right), which allowed to adapt the setup for the existent devices for measuring in the He^4 cryostat. The magnetic field is calculated from the current placed in the superconducting coils.

Since in both setups, only a passive cooling system can be used, it was not possible to get a control of the temperature on the cold side. However, the temperature difference between the warm and the cold side can be tuned

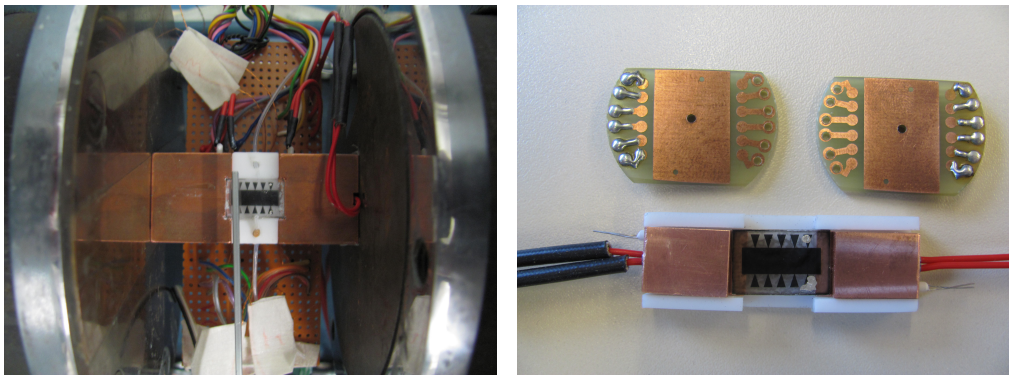

Figure 8.4: Left, room temperature setup. Right, low temperature setup.

with sufficient accuracy.

Finally, the temperature gradient produced by the room temperature setup was measured. Six Pt-100 resistances were used, one cylindrical placed in the warm copper block, one cylindrical in the cold copper block and four planar ones on the film surface. The measurement obtained in temperature equilibrium and without gradient was used to normalize the signal from the six resistances. Unfortunately, such measurement could not be done an the low temperature setup.

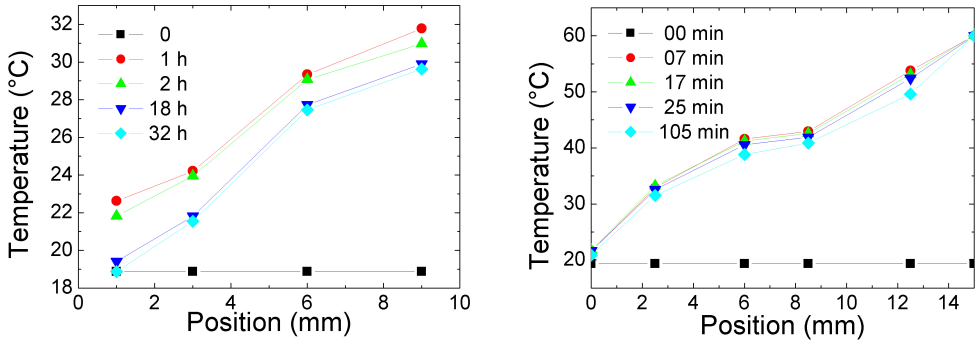

Figure 8.5: Study of the temperature gradient on the room temperature setup. Left, on Al_2O_3 substrate. Right, on MgO substrate.

In figure 8.5 one can see the temperature gradient evolution measured on Al_2O_3 (left) and on MgO (right). A deviation from a linear behavior is also visible. However, it was not possible to define the position of the Pt-100 sensors on the film with high precision. Such deviations can be attributed to the uncertainty in the sensor position. From figure 8.5 right, one can conclude that it is necessary to wait seven minutes to get a stable temperature gradient.

Afterwards, the temperature difference between the cold and warm side stays constant during several hours (fig. 8.5 left).

8.3 Measurements with the electromagnet

Before performing any measurement, it was necessary to estimate the possible sources of error and characterize them. For instance, the room temperature setup was not electromagnetically shielded, a contact misalignment could drive into a Seebeck voltage and the applied magnetic field could induce currents.

In order to calibrate the system, a structured $Ni_{80}Fe_{20}$-Pt sample was mounted on the setup and placed between the poles of the electromagnet. We measured without an applied magnetic field and neither a temperature gradient. The result was a fluctuating signal in the range of 0.1 μV. Then, the applied magnetic field was varied from -300 Oe to +300 Oe (performing several cycles) without any applied temperature gradient. The error of this signal was 0.15 μV. Afterwards, a temperature difference of 32 °C was applied at zero magnetic field. For this signal a error of 0.2 μV was measured. Therefore, the measurement error was 0.45 μV. Since, the largest signal measured by Uchida et al.[4] at $\Delta T = 18\,°C$ was $\approx 5\,\mu V$ and in the setup used in this thesis achieved a higher temperature difference, no further improvements on the measurement accuracy were required.

Unfortunately, the measurements performed on Heusler-Pt and $Ni_{80}Fe_{20}$-Pt films did not reveal any characteristic hysteresis loops expected from the original experiment as result of the MSSE. On Heusler-Pt samples, oscillations within the expected error range were detected. On $Ni_{80}Fe_{20}$-Pt samples an unexpected feature arises (fig. 8.6). For both cases, the deposition parameters were changed to obtain smooth interfaces. Different thickness configurations for $Ni_{80}Fe_{20}$ and platinum layers were tried. However, similar signals were observed.

To clarify the origin of the signal, further measurements were required. In MSSE, the signal measured on the cold side is inverted with respect to the signal from the warm side. Also, if the source of the measurement shown in figure 8.6 is the conversion of a spin current into a charge current, it has to vanish by measuring on a contact, which has no platinum.

Keeping the heat flow in the same direction, we performed measurements with the platinum wire placed on the cold side, on the hot side and direct on $Ni_{80}Fe_{20}$ film surface. The figures 8.6 and 8.7 look different, because the step size between two measurements was increased. In the second case, the step size is one order of magnitude larger.

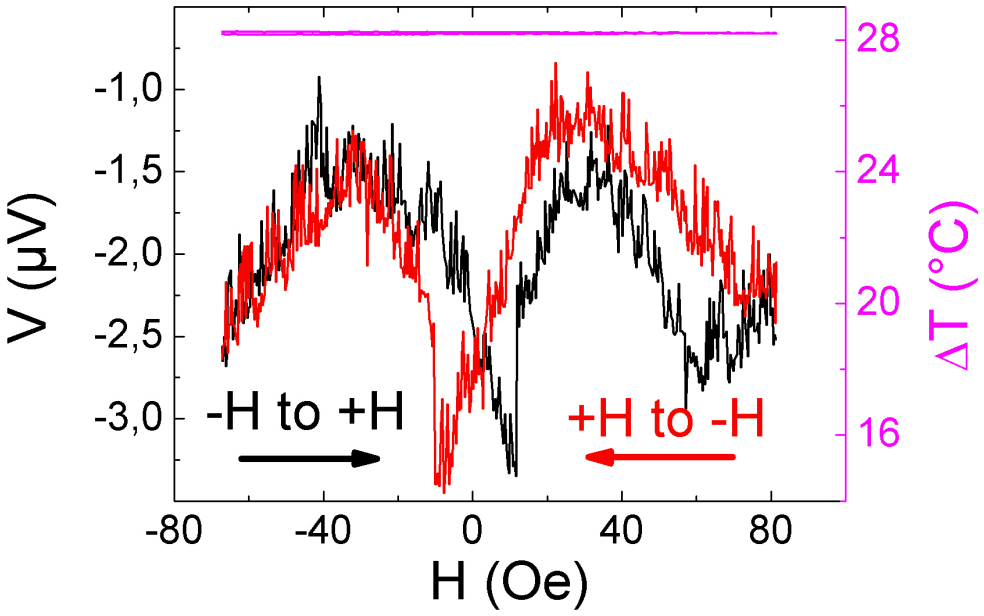

Figure 8.6: Measurement on $Ni_{80}Fe_{20}$-Pt structured film while the magnetic field was varied. Black, from negative to positive values. Red, from positive to negative values. The magenta lines indicates the temperature difference between the two copper blocks.

An equal shape signal was obtained from the three cases (fig. 8.7). The shift of 5 Oe observed in the peak position can be explained by the gradient in film thickness, which was described in chapter 5. In the thickest parts of the films more energy is required to switch the magnetization. This observation can also help to understand the discrepancy in coercive field observed in the different the VSM measurements (fig. 8.1) $H_c \approx 4$ Oe and the ones measured by LMOKE at 0°, $H_c \approx 7$ Oe (fig 8.3). Since, the VSM results came from an average of the whole film and LMOKE measures a 200 μm point placed on the center of the film surface. This measurements discard the conversion of the spin current into a charge current for the described experiments. Therefore, a classic effect has to be the source of the signal.

In the same fashion, the Nernst effect can be understood as equivalent to the Hall effect. The Nernst effect has the same experimental geometry like the Hall effect. However, the source of the current is substituted by an applied heat flow. It has to be possible to observe an equivalent of the Planar Hall effect driven by a temperature gradient, the Planar Nernst effect.[149]

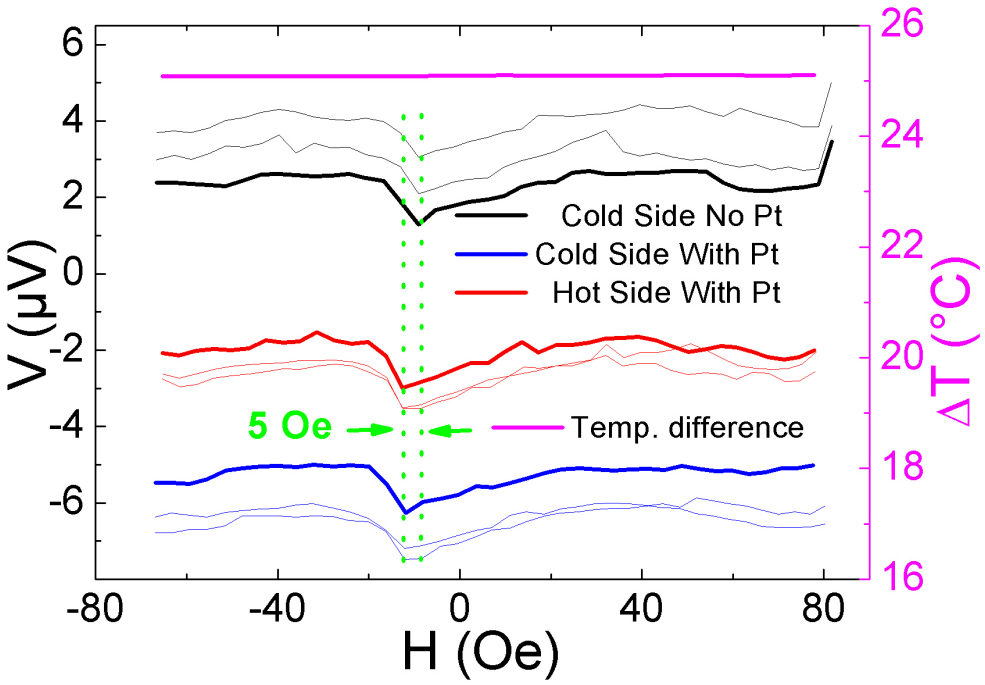

Figure 8.7: Measurements on $Ni_{80}Fe_{20}$-Pt structured film while the magnetic field was tuned from positive to negative values. The temperature gradient was in the same direction. Red (Hot side) and Blue (cold side) lines represent measurements taken on the platinum contacts. Black (cold side) represent the direct measurement on $Ni_{80}Fe_{20}$. The magenta line indicates the temperature difference between the two copper blocks. Green doted lines mark the peak positions.

Antonov et al.[150] studied the Planar Hall effect on multi domain permalloy samples. They established a theoretical model based on one and two domain structures distributed on the sample. In this model the internal effective magnetic field, the domain wall area, the domain wall motion and contributions from the OHE are considered.

Since the Planar Nernst effect can be understood as equivalent to the Planar Hall effect in which the current flow is substituted by a heat flow. At least, one would expect to observe a comparable behavior to the one described in the Antonov's work and the presented measurements (fig. 8.6 and 8.7). Indeed, if we suppose an angle between the magnetization and the gradient direction in the range of 30° and 60°, the numerical results from this model reproduce the behavior of the measured data. There are still discrepancies between the proposed model and the presented experimental

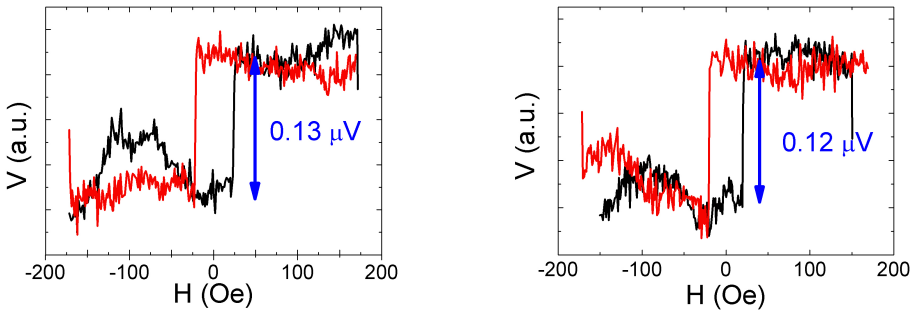

Figure 8.8: 10 nm of Pt on 20 nm of $Co_2FeSi_{0.6}Al_{0.4}$ deposited on Al_2O_3. Left, measured on the cold side with a 20 K gradient and on bare $Co_2FeSi_{0.6}Al_{0.4}$. Right, with both heaters working.

results but this might be attributed to a more complex domain distribution.

8.4 Measurements in the cryostat

Adachi et al.[87] published data of a giant enhancement of the MSSE by phonon drag at low temperatures. Therefore, the following experimental approach was based on the possibility to observe a MSSE signal at low temperatures which overcomes the one caused by the Planar Nernst effect. Additionally, the cryostat offers an electro-magnetically shielded environment as well as the wiring. As a result, the noise level of the measurement was reduced by a factor ≈ 20.

The measurements performed at room temperature were repeated at different low temperatures and for different temperature gradients. In case of structured $Ni_{80}Fe_{20}$ samples, similar curves to figure 8.6 were observed. In these cases, these curves were attributed to the Planar Nernst effect. The MSSE was not observed at any temperature with any temperature gradient.

Further attempts were performed on $Co_2FeSi_{0.6}Al_{0.4}$ and permalloy structured thin films. The permalloy sample was grown by molecular beam epitaxy and covered with 10 nm of palladium instead of platinum. This sample has an isotropic magnetization.

Since, the signal observed on $Co_2FeSi_{0.6}Al_{0.4}$ (fig. 8.8) (permalloy) was observed by using the contacts with Platinum (Palladium) and by measuring on the bare $Co_2FeSi_{0.6}Al_{0.4}$ (permalloy), it was not possible to attribute the signal to the MSSE. In figure 8.8, one can see the anomalous Nernst effect (equivalent to anomalous Hall effect) which is proportional to the magnetization. In consequence, a jump in the signal has to be observed when the

magnetization switches. This signal was not detected in the room temperature setup because its size is below the measurement error.

For an in plane temperature gradient, one would expect to invert the signal by inverting the temperature gradient. However, the same behavior was measured independent on the direction of the temperature gradient. Even more, a similar signal was measured by applying heat from both sides (fig 8.8 right), simultaneously.

The former observation can be explained by the temperature distribution during the measurements. The temperature difference between the hot side and the cold side is up to 30 K. The difference between the cold side and the environment is up to 50 K. Therefore, on any sample position there are three gradients presents, one in plane and two out of plane (fig. 8.9). The one out of plane, across the film surface, together with the inplane magnetization yields on anomalous Nernst effect.

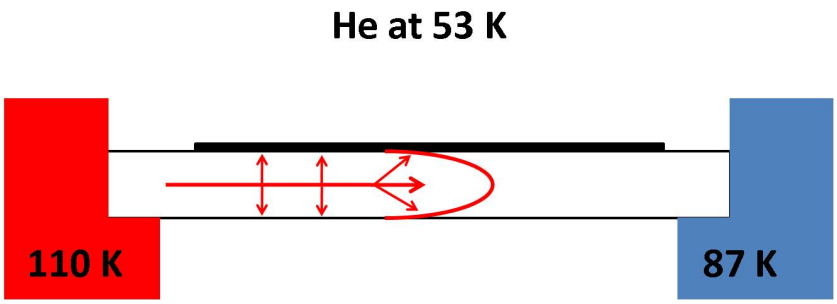

Figure 8.9: Heat flow scheme.

This problem was solved by placing a second substrate on top of the film. It was also in thermal contact with the heat baths. In this situation the out of plane heat flows, coming from each substrate cancel each other. With these experimental conditions, it was possible to reverse the signal (fig. 8.8) by reversing the heat flow. However, the signals detected on the platinum and on the bare material were identical. Therefore, it has to be attributed to the anomalous Nernst effect.

8.5 Summary

In order to measure the MSSE, the experiment described by Uchida et al.[4] was reproduced. The deposition conditions which lead to permalloy thin films with low magnetic damping and coercive fields were achieved. The AFM pictures reveal a featureless permalloy surface. The platinum top layer

is deposited a few seconds after the deposition of permalloy to avoid contamination. The etching process was improved in two ways, i) by measuring in situ the resistance of the platinum reference sample and ii) by eliminating the silver glue from the etching process. The AFM pictures confirm the accuracy of the etching process. The images indicate a wire thickness of 10 nm. Therefore, the etching process is not producing a significant over etching. EDX measurements confirm the absence of platinum in the region around the platinum wire. Regarding the experimental setup, the problems coming from the heat flow direction were solved. The sensitivity was also improved to $\pm 0.02\,\mu$V. However, even in the room temperature setup the accuracy of the measurement has to be sufficient ($\pm 0.5\,\mu$V). The signal reported by Uchida et al.[4] was $5\,\mu$V ($\Delta T = 21$ K).

The reproduction of this signal was not possible in this work. However, also other groups in Germany with long expertise in magnetoelectronics could not reproduce the Uchida experiment in spite of strong efforts.

Chapter 9

Conclusions

The present thesis studies the evolution of the crystal structure in thin films of three Heusler compounds in dependence of the preparation conditions. Consistently with the behavior of many Heusler compounds reported in literature, a change in $L2_1$ order as a function of the deposition temperature was observed. The maximum is established at $T \approx 550°C$ for $Co_2FeSi_{0.6}Al_{0.4}$ and $Co_2FeGa_{0.5}Ge_{0.5}$. Co_2MnAl thin films with $L2_1$ structure have never been produced. However, the maximum value of saturation magnetization, for Co_2MnAl, is measured at $T \approx 550°C$. This value is compatible with the expected value for the B2 phase.

By using AFM images, x-ray analysis and transport measurements, a consistent picture of the growth process at certain deposition temperatures arises for the studied Heusler compounds. In early deposition stages (up to $\approx 20\,nm$), small grain-like structures appeared. As the thickness of the deposited material increases, the size of the structures also increases due to the unification of adjoined structures. The final structures can be columns or labyrinth structures depending on the deposition temperature. X-ray and residual resistivity data suggest a higher content of $L2_1$ phase for the thinnest films, which might be explained considering the growth process described above. For the thinnest films, the smallest structures were observed. These structures minimize the elastic energy due to the lattice mismatch with the substrate. While the structures grow and incorporate material from the surrounding they have to accommodate a crystalline structure from different grains and different crystalline phases. This process adds new sources of further defects and disorder. Finally, the grain size was studied. It was seen that different crystalline ordering coexist inside each grain.

Once the morphology and the crystal quality of the selected Heusler compounds were determined, the influence of the disorder and defects on the AHE was studied. A simple mathematical data treatment is presented for anal-

ysis of the AHE in materials with low residual resistivity ratios. For these materials the idealized assumptions of one skew scattering contribution and one intrinsic contribution often used failed. The analysis allows to eliminate the influence of the otherwise dominating temperature-independent parts $\rho_{xxT}(T_l)$ and $\rho_{xy}^{AHE}(T_l)$:

$$\begin{aligned}\rho_{xy}^{AHE}(T_h) - \rho_{xy}^{AHE}(T_l) = \\ =(a + 2\sigma^{AH-bj}\rho_{xx0})(\rho_{xxT}(T_h) - \rho_{xxT}(T_l))+ \\ +\sigma^{AH-bj}(\rho_{xxT}(T_h)^2 - \rho_{xxT}(T_l)^2).\end{aligned} \tag{9.1}$$

For the Heusler compounds $Co_2FeSi_{0.6}Al_{0.4}$ and $Co_2FeGa_{0.5}Ge_{0.5}$ the skew scattering is found to be the dominating temperature dependent contribution to the anomalous Hall effect. By comparing the samples with different degree of atomic ordering, the information on the temperature-independent part of the AHE $\rho_{xy,0}$ was obtained. This term increases in the positive direction with increasing level of B2 disorder. $L2_1$ ordered samples have a slightly negative AHE at low temperature, while a DO_3 phase leads to stronger negative values.

In addition, the strong and temperature independent AHE of the complex Heusler compound Co_2MnAl was investigated, which opens the possibility to produce magnetic field sensors working in a wide range of temperatures. The AHE properties are remarkably robust with respect to the deposition procedure up to 100°C. The films can be deposited on different substrates and also under moderate vacuum conditions and nevertheless exhibit the characteristic Hall behavior. An extension of the working range up to 300 °C using appropriate deposition conditions was achieved. A linear response to magnetic fields up 0.6 T makes the material suitable for applications under high temperatures. The photoelectron spectroscopy studies show a saturation of the oxidation, such that possibly no additional protection layers are needed for a sensor. The comparably high longitudinal resistivity of the Heusler compound can be compensated with a suitable sensor design.

LMOKE and QMOKE measurements were performed on $Co_2FeSi_{0.6}Al_{0.4}$ and $Co_2FeGa_{0.5}Ge_{0.5}$. The polar plots of coercive field reveals that an extrinsic factor like film roughness is a key on the observation of the magnetic anisotropy. In such cases, the presence or absence of a $L2_1$ phase plays a marginal role. For samples deposited at lowest temperatures, with the highest content of A2 phase and lowest roughness, the magnetic anisotropy is observed clearly. For samples deposited at highest temperatures, the roughness shows a maximum and no magnetic anisotropy is observed. In the case of QMOKE measurements, a relation between the crystalline order and the

QMOKE signal is present. However, more investigations are required to achieve an appropriate understanding of the relation.

The magnon-driven spin Seebeck effect (MSSE) was investigated by reproducing the experimental conditions described on the first paper[4] published on this novel effect. Permalloy and Heusler thin films on different substrates were used. The deposition parameters were optimized to achieve permalloy samples with the required low magnetic damping constants. Additionally, smooth permalloy surfaces were obtained. Platinum wires were used to minimize parasitic thermo voltage. The improvement of the etching process resulted in cleaner samples. In the worst case, the accuracy of our measurement was one order of magnitude lower than the signal expected. The MSSE was investigated at room temperature and at low temperature (an enhancement of the signal was expected). Experimental challenges, like the measurement of the in plane heat flow, were appropriately solved. However no Spin Seebeck signal was measured. Similar results are reported by other groups that tried to measure the effect. At this point, it is possible to conclude that some relevant experimental parameters were not published. In relation with this topic, the most relevant experimental attempts (with positive results) on permalloy,[4,151] on Heusler[146] and on magnetic insulators[152] as well as the longitudinal MSSE[153] belong to Ken-Chi Uchida and Eiji Saitoh. Therefore, an independent cross check of these results is still lacking.

Appendix

In this section, raw data from Hall effect measurements at different temperatures is showed. Each plot corresponds to $Co_2FeGa_{0.5}Ge_{0.5}$ samples deposited at different temperatures. In the first set of figures, the data taken on samples deposited on Al_2O_3 is shown and the second set correspond to samples deposited on MgO.

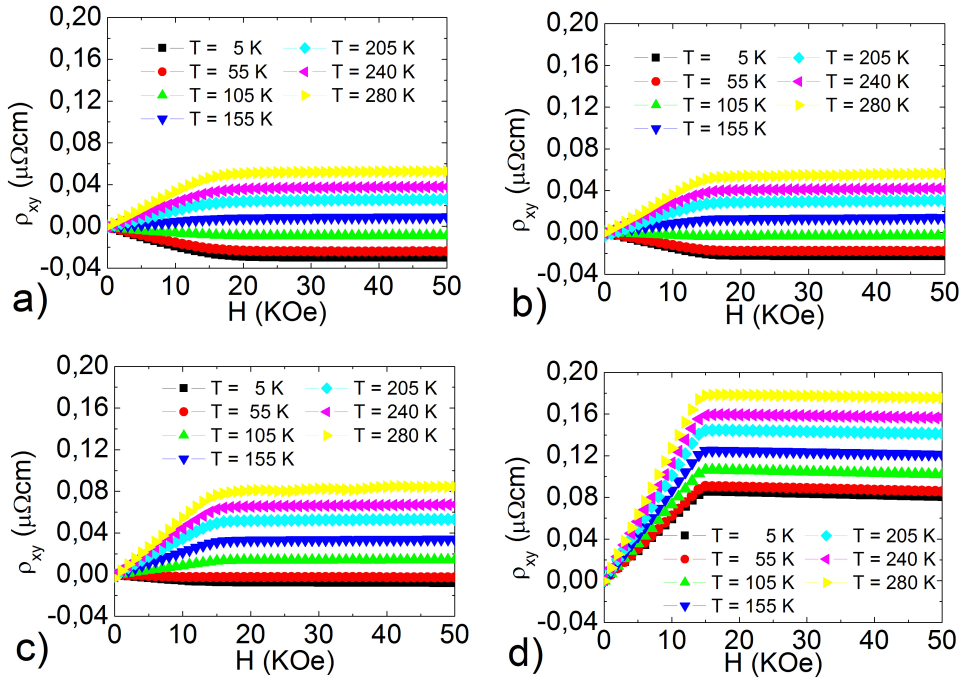

Figure 9.1: Hall effect measurements of $Co_2FeGa_{0.5}Ge_{0.5}$ deposited at (a) 723 °C, (b) 590 °C, (c) 497 °C and (d) 442 °C. The legends indicate the respective measurement temperatures.

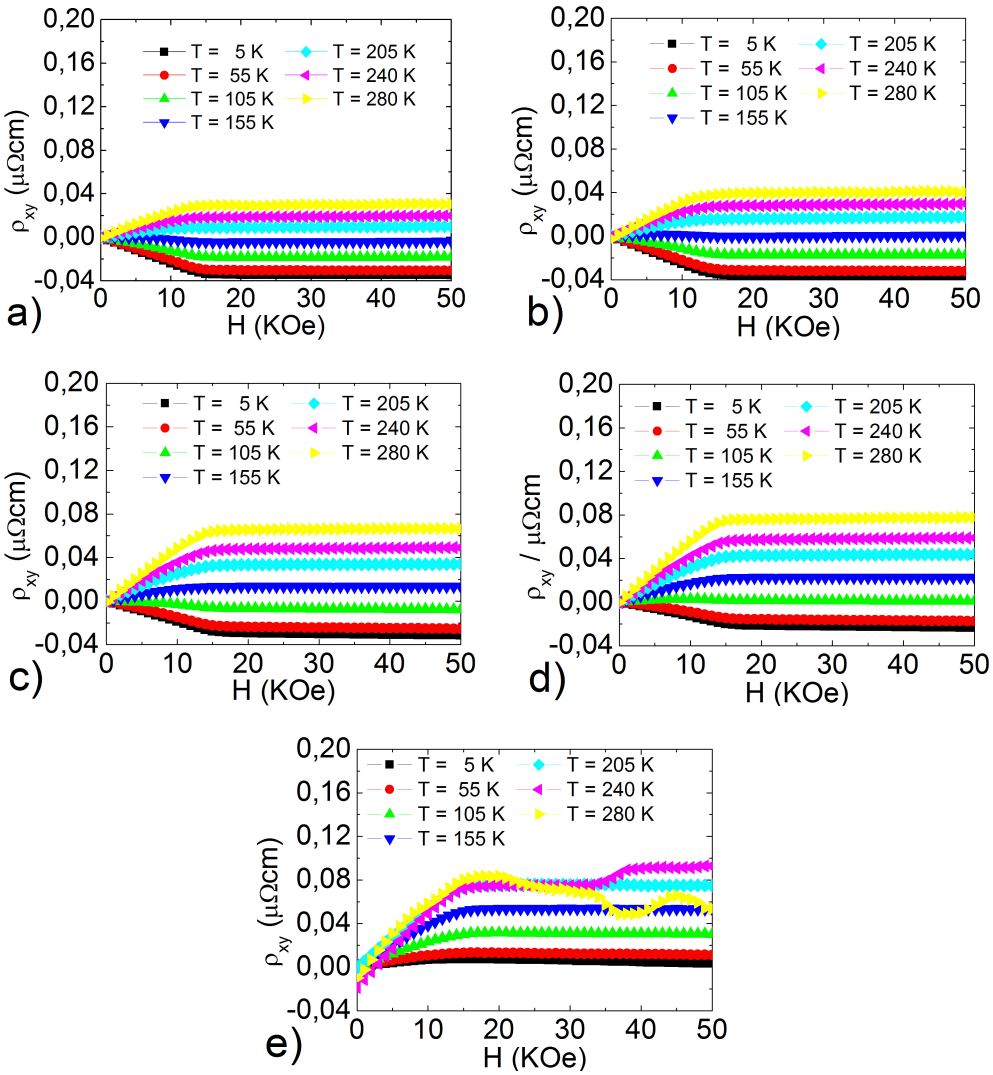

Figure 9.2: Hall effect measurements of $Co_2FeGa_{0.5}Ge_{0.5}$ deposited at (a) 660 °C, (b) 637 °C, (c) 557 °C, (d) 508 °C and 463 °C. The legends indicate the respective measurement temperatures.

Bibliography

[1] S. S. Kubakaddif, P. N. Butchert, and B. G. Mulimanit *Phys.: Condens. Matter*, vol. 3, p. 5445, 1991.

[2] N. W. Ashcroft and N. D. Mermin, *Solid State physics*. Saunders college publishing at Florida, 1976.

[3] P. N. Butcher, N. H. March, and M. P. Tosi, *Physics of Low-Dimensional Semiconductor Structures*. Plenum Press, New York, 1993.

[4] K. Uchida, S. Takahashi, K. Harii, J. Ieda, W. Koshibae, K. Ando, S. Maekawa, and E. Saitoh *Nature*, vol. 455, p. 778, 2008.

[5] C. Garritz, J. A. Chamizo, and A. Garritz, *Estructura átomica*. National University of Mexico, 1986.

[6] J. Gratton, *Introdución a la mecánica cuántica*. University of Buenos Aires, 2003.

[7] S. Blügel, D. Bürgler, M. Morgenstern, C. M. Schneider, and R. Waser, *Spintronics: From GMR to Quantum information*. Schriften des Forschngszentrums Jülich, 2009.

[8] A. Aharoni, *Introduction to the Theory of Ferromagnetism*. Oxford university press at Israel, 1996.

[9] D. D. Stancil and A. Prabhakar, *Spin Waves: Theory and Applications*. Springer, 2009.

[10] N. W. Ashcroft and A. Aharoni, *Solid State Physics*. Saunders College Publishing at Florida, 1976.

[11] R. F. Butler, *Paleomagnetism:Magnetic Domains to Geologic Terranes*. Department of Chemistry and Physics, University of Portland, 2004.

[12] J. D. Jackson, *Klassische Elektrodynamik*. Walter de Gruyter, Berlin, New York, 2002.

[13] M. Hanson, C. Johansson, B. Nilsson, P. Isberg, and R. Wäppling *J. Appl. Phys.*, vol. 85, p. 2793, 1999.

[14] S. Chikazumi, *Physics of Magnetism*. Wiley, New York, 1964.

[15] *Bell System laboratory, British Patent*, pp. No. 188,688.

[16] M. R.Andrews *Phys. Rev.*, vol. 18, p. 245, 1921.

[17] H. Gong, M. Rao, D. E. Laughlin, and D. N. Lambeth *J. Appl. Phys.*, vol. 85, 8, p. 5750, 1999.

[18] F. Michelini, L. Ressier, J. Degauque, P. Baulés, A. R. Fert, J. P. Peyrade, and J. F. Bobo *J. Appl. Phys.*, vol. 92, 12, p. 7337, 2002.

[19] I. B. Puchalska, A. Sukiennicki, Z. Petykiewicz, and T. Tymosz *Phys. stat. sol.*, vol. 21, p. 183, 1967.

[20] A. Gangulee and R. L. Anderson *Journal of Electronic Materials*, vol. 3, 1, p. 171, 1974.

[21] T. G. S. M. Rijks, W. J. M. de Jonge, W. Folkerts, J. C. S. Kools, and R. Coehoorn *Appl. Phys. Lett.*, vol. 65, p. 916, 1994.

[22] K. T. Wu and R. J. Gambino *J. Appl. Phys.*, vol. 79, p. 6285, 1996.

[23] T. Devolder, C. Chappert, Y. Chen, E. Cambril, H. Bernas, J. P. Jamet, and J. Ferre *Appl. Phys. Lett.*, vol. 74, p. 3383, 1999.

[24] F. Heusler *Verh. Dtsch. Phys*, vol. 5, p. 219, 1903.

[25] I. Galanakis, P. Mavropoulos, and P. H. Dederichs *J. Phys. D: Appl. Phys.*, vol. 39, p. 765, 2006.

[26] R. A. de Groot and F. M. Mueller *Phys. Rev. Lett.*, vol. 50, p. 2024, 1983.

[27] T. Miyazaki, N. Tezuka, and S. Kumagaia *J. Magn. Magn. Mater.*, vol. 139, p. L231, 1995.

[28] J. S. Moodera, L. R. Kinder, T. M. Wong, and R. Meservey *Phys. Rev. Lett.*, vol. 74, p. 3273, 1995.

[29] J. S. Moodera, L. R. Kinder, T. M. Wong, and R. Meservey *J. Magn. Magn. Mater.*, vol. 159, p. L1, 1996.

[30] L. Berger *Phys. Rev. B*, vol. 54, p. 9353, 1996.

[31] I. Galanakis and P. H. Dederichs *Phys. Rev. B*, vol. 66, p. 174429, 2002.

[32] Y. Miura, M. Shirai, and K. Nagao *J. Appl. Phys.*, vol. 99, p. 08J112, 2006.

[33] P. Mavropoulos, K. Sato, R. Zeller, and P. H. Dederichs *Phys. Rev. B*, vol. 69, p. 054424, 2004.

[34] P. Mavropoulos, I. Galanakis, V. Popescu, and P. H. Dederichs *J. Phys.: Condens. Matter*, vol. 16, p. S5759, 2004.

[35] M. Sargolzaei, M. Richter, K. Koepernik, I. Opahle, and H. Eschrig *Phys. Rev. B*, vol. 74, p. 224410, 2006.

[36] L. Chioncel, E. Arrigoni, M. I. Katsnelson, and A. I. Lichtenstein *Phys. Rev. Lett.*, vol. 96, p. 137203, 2006.

[37] J. Slater *Phys. Rev.*, vol. 49, p. 931, 1936.

[38] L. Pauling *Phys. Rev.*, vol. 54, p. 899, 1938.

[39] G. H. Fecher, H. C. Kandpal, S. Wurmehl, J. Morais, H.-J. Lin, H.-J. Elmers, G. Schönhense, and C. Felser *J. Phys.: Condens. Matter*, vol. 17, p. 7237, 2005.

[40] B. Balke, G. H. Fecher, H. C. Kandpal, and C. Felser *Phys. Rev. B*, vol. 74, p. 104405, 2006.

[41] N. Tezuka, N. Ikeda, S. Sugimoto, and K. Inomata *Appl. Phys. Lett.*, vol. 89, p. 252508, 2006.

[42] G. H. Fecher and C. Felser *J. Phys. D: Appl. Phys.*, vol. 40, p. 1582, 2007.

[43] B. Balke, G. H. Fecher, and C. Felser *Appl. Phys. Lett.*, vol. 90, p. 242503, 2007.

[44] Z. Gercsi and K. Hono *J. Phys.: Condens. Matter*, vol. 19, p. 326216, 2007.

[45] M. Oogane, Y. Sakuraba, J. Nakata, H. Kubota, Y. Ando, A. Sakuma, and T. Miyazaki *J. Phys. D: Appl. Phys.*, vol. 39, p. 834, 2006.

[46] Y. Sakuraba, J. Nakata, M. Oogane, Y. Ando1, H. Kato, A. Sakuma, T. Miyazaki, and H. Kubota *Appl. Phys. Lett.*, vol. 88, p. 022503, 2006.

[47] Y. J. Chen, D. Basiaga, J. R. O. Brien, and D. Heiman *Appl. Phys. Lett.*, vol. 84, p. 4301, 2004.

[48] C. M. Hurd, *The Hall effect in metals and alloys.* Plenum Press, New York, 1972.

[49] K. Behnia *J. Phys.: Condens. Matter*, vol. 21, p. 113101, 2009.

[50] E. H. Sondheimer *R. Soc. London*, vol. Ser. A 193, p. 484, 1948.

[51] S. Zhang and Z. Yang *Phys. Rev. Lett.*, vol. 94, p. 066602, 2005.

[52] C. Brüne, A. Roth, E. G. Novik, M. König, H. Buhmann, E. M. Hankiewicz, W. Hanke, J. Sinova, and L. Molenkamp *Nature Physics*, vol. 6, p. 448, 2010.

[53] L. K. Werake, B. A. Ruzicka, and H. Zhao *Phys. Rev. Lett.*, vol. 106, p. 107205, 2011.

[54] R. H. Silsbee *J. Phys.: Condens. Matter*, vol. 16, p. R179, 2004.

[55] J. Sinova, D. Culcer, Q. Niu, N. A. Sinitsyn, T. Jungwirth, and A. H. M. Donald *Phys. Rev. Lett.*, vol. 92, 9, pp. 126603–1, 2004.

[56] J. E. Hirsch *Phys. Rev. Lett.*, vol. 83, 9, p. 1834, 1999.

[57] N. Nagaosa, J. Sinova, S. Onoda, A. H. MacDonald, and N. P. Ong *Rev. Mod. Phys.*, vol. 82, p. 1539, 2010.

[58] T. Jungwirth, Q. Niu, and A. H. MacDonald *Phys. Rev. Lett.*, vol. 88, p. 207208, 2002.

[59] S. Onoda and N. Nagaosa *J. Phys. Soc. Jpn.*, vol. 71, p. 19, 2002.

[60] M.-C. Chang and Q. Niu *Phys. Rev. B*, vol. 53, p. 7010, 1996.

[61] D. Xiao, M. C. Chang, and N. Qian *Reviews of Modern Physics*, vol. 82, p. 1959, 2010.

[62] J. Smit *Physica (Amsterdam)*, vol. 18, p. 877, 1955.

[63] J. Smit *Physica (Amsterdam)*, vol. 24, p. 39, 1958.

[64] J. N. Chazalviel *Phys. Rev. B*, vol. 11, p. 3918, 1975.

[65] N. A. Sinitsyn, Q. Niu, and A. H. MacDonald *Phys. Rev. B*, vol. 73, p. 075318, 2006.

[66] R. Karplus and J. M. Luttinger *Phys. Rev.*, vol. 95, p. 1154, 1954.

[67] S. N. Kaul and M. Rosenberg *Phys. Rev. B*, vol. 27, p. 5689, 1983.

[68] A. Fert and R. Azomosa *J. Appl. Phys.*, vol. 50, p. 1886, 1979.

[69] U. Dibbern *Sensors and Actuators*, vol. 10, p. 127, 1986.

[70] P. P. Freitas and T. S. Plaskett *Phys. Rev. Lett.*, vol. 64, p. 2184, 1990.

[71] I. A. Campbell, A. Fert, and O. Jaoul *J. Phys. C: Solid State Phys.*, vol. 3, p. S95, 1969.

[72] T. R. McGuire and R. I. Potter *IEEE transactions on magnetics*, vol. Mag 11, 4, p. 1018, 1975.

[73] M. Weiler, F. D. Czeschka, A. Brandlmaier, I.-M. Imort, G. Reiss, A. Thomas, G. Woltersdorf, R. Gross, and S. T. B. Goennenwein *Appl. Phys. Lett.*, vol. 98, p. 042501, 2011.

[74] J. H. J. Fluitman *Sensors and Actuators*, vol. 2, p. 155, 1981.

[75] L. Ejsing, M. F. Hansen, A. K. Menon, H. A. Ferreira, D. L. Graham, and P. P. Freitas *Appl. Phys. Lett.*, vol. 84, 23, p. 4729, 2004.

[76] Y. Bason, L. Klein, H. Q. Wang, J. Hoffman, X. Hong, V. E. Henrich, and C. H. Ahn *J. Appl. Phys.*, vol. 101, p. 09J507, 2007.

[77] F. Montaigne, A. Schuhl, and F. V. Dau *Sensors and Actuators*, vol. 81, p. 324, 2000.

[78] A. Adeyeye, M. Win, T. Tan, G. Chong, V. Ng, and T. Low *Sensors and Actuators*, vol. A 116, p. 95, 2004.

[79] B. Hillebrands and K. Ounadjela, *Spin Dynamics in Confined Magnetic Structures I.* Spinger, 2002.

[80] F. J. Dyson *Phys. Rev.*, vol. 102, p. 1217, 1956.

[81] F. J. Dyson *Phys. Rev.*, vol. 102, p. 1230, 1956.

[82] T. Oguchi *Phys. Rev.*, vol. 117, p. 117, 1960.

[83] Y. Tserkovnyak, A. Brataas, and G. E. W. Bauer *Phys. Rev. Lett.*, vol. 88, p. 117601, 2002.

[84] J. Xiao, G. E. W. Bauer, K. Uchida, E. Saitoh, and S. Maekawa *Phys. Rev. B*, vol. 81, p. 214418, 2010.

[85] M. Hatamia, G. E. Bauer, S. Takahashi, and S. Maekawab *Solid State Commun.*, vol. 150, p. 480, 2010.

[86] D. J. Sanders and D. Walton *Phys. Rev. B*, vol. 15, p. 1489, 1977.

[87] H. Adachi, K. Uchida, E. Saitoh, J. Ohe, S. Takahashi, and S. Maekawa *Appl. Phys. Lett.*, vol. 97, p. 252506, 2010.

[88] C. M. Jaworski, J. Yang, S. Mack, D. D. Awschalom, J. P. Heremans, and R. C. Myers *Nature Materials*, vol. 9, p. 898, 2010.

[89] F. J. Blatt, P. A. Schroeder, C. L. Foiles, and D. Greig, *Thermoelectric Power of Metals*. Plenum, New York, 1976.

[90] E. M. Lifshitz and L. P. Pitaevskii, *Physical Kinetics*. Pergamon, New York, 1982.

[91] Y. Gurevich and O. Mashkevich *Phys. Reports*, vol. 181, No. 6, p. 327, 1989.

[92] K. Köhler, J. W. Coburn, D. E. Horne, and E. Kay *Appl. Phys.*, vol. 57, p. 59, 1985.

[93] C. Beneking *Appl. Phys.*, vol. 68, p. 4461, 1990.

[94] P. J. Webster *J. Phys. Chem. Solids*, vol. 32, p. 1221, 1971.

[95] M. Zhang, E. Bruck, F. R. de Boer, Z. Li, and G. Wu *J. Phys. D: Appl. Phys.*, vol. 37, p. 2049, 2004.

[96] B. L. Flur and J. Riseman *J. Appl. Phys.*, vol. 35, p. 344, 1964.

[97] S. U. Jen, Y. T. Chen, N. T. Yang, and W. C. Cheng *Appl Phys A*, vol. 94, p. 431, 2008.

[98] G. A. Slack *Phys. Rev.*, vol. 126, p. 427, 1962.

[99] J. Du, S. Gnanarajan, and A. Bendavid *Supercond. Sci. Technol.*, vol. 18, p. 1035, 2005.

[100] J. Thompson *Proc. Camb. Philos. Soc.*, vol. 11, p. 1120, 1901.

[101] K. Fuchs *Proc. Camb. Philos. Soc.*, vol. 34, p. 100, 1938.

[102] C. G. F. Blum, C. A. Jenkins, J. Barth, C. Felser, S. Wurmehl, G. Friemel, C. Hess, G. Behr, B. Büchner, A. Reller, S. Riegg, S. G. Ebbinghaus, T. Ellis, P. J. Jacobs, J. T. Kohlhepp, and H. J. M. Swagten *Appl. Phys. Lett.*, vol. 95, p. 161903, 2009.

[103] V. Holý, U. Pietsch, and T. Baumbach, *High-Resolution X-Ray Scattering from thin films and multilayers*. Springer-Verlag Berlin Heidelberg, 1999.

[104] P. J. Webster *Contemp. Phys*, vol. 10, 6, p. 559, 1969.

[105] E. Arbelo, M. Jourdan, M. Kallmayer, P. Klaer, and H.-J. Elmers *Journal of Physics: Conference Series*, vol. 200, p. 072006, 2010.

[106] P. Scherrer *Göttinger Nachrichten*, 1918.

[107] A. L. Patterson *Phys. Rev.*, vol. 56, p. 978, 1939.

[108] W. Burgei, M. J. Pechan, and H. Jaeger *Am. J. Phys.*, vol. 71 (8), p. 825, 2003.

[109] I. Isenberg, B. R. Russell, and R. F. Greene *Review of Scientific Instruments*, vol. 19, 10, p. 685, 1948.

[110] H. Schneider, *Wachstum und Eigenschaften dünner Co-basierter Heusler-Filme*. Johannes Gutenberg-Universität Mainz, 2010.

[111] S. Picozzi, A. Continenza, and A. J. Freeman *Phys. Rev. B*, vol. 69, p. 094423, 2004.

[112] V. Ksenofontov, C. Herbort, M. Jourdan, and C. Felser *Appl. Phys. Lett.*, vol. 92, p. 262501, 2008.

[113] K. Kubo and N. Ohata *J. Phys. Soc. Jpn.*, vol. 33, p. 21, 1972.

[114] N. Furukawa *J. Phys. Soc. Jpn.*, vol. 69, p. 1954, 2000.

[115] L. J. Singh, Z. H. Barber, Y. Miyoshi, W. R. Branford, and L. F. Cohen *J. Appl. Phys.*, vol. 95, p. 7231, 2004.

[116] C. Hordequin, D. Risouiu, L. Ranna, and J. Pierre *Eur. Phys. J.*, vol. B 16, p. 3280, 2000.

[117] W. Jiang, A. Wirthmann, Y. S. Gui, X. Z. Zhou, M. Reinwald, W. Wegscheider, C.-M. Hu, and G. Williams *Phys. Rev. B*, vol. 80, p. 214409, 2009.

[118] Y. Tian, L. Ye, and X.Jin *Phys. Rev. Lett.*, vol. 103, p. 087206, 2009.

[119] J. Kötzler and W. Gil *Phys. Rev. B*, vol. 72, p. 060412, 2005.

[120] S. Onoda, N. Sugimoto, and N. Nagaosa *Phys. Rev. B*, vol. 77, p. 165103, 2008.

[121] A. A. Kovalev, Y. Tserkovnya, K. Vyborny, and J. Sinova *Phys. Rev. B*, vol. 79, p. 195129, 2009.

[122] Y. Sakuraba, M. Hattori, M. Oogane, H. Kubota, Y. Ando, A. Sakuma, and T. Miyazaki *J. Phys. D*, vol. 40, p. 1221, 2007.

[123] D. Ebke, V. Drewello, M. Schafers, G. Reiss, and A. Thomas *Appl. Phys. Lett.*, vol. B 95, p. 232510, 2009.

[124] B. Balke, S. Wurmehl, G. H. Fecher, C. Felser, and J. Kübler *Sci. Technol. Adv. Mater.*, vol. 9, p. 014102, 2008.

[125] H. Schneider, E. Vidal, G. Jakob, S. Chadov, G. Fecher, and C. Felser *J. Magn. Magn. Mater.*, vol. 322, p. 579, 2010.

[126] Y. Miura, K. Nagao, and M. Shirai *Phys. Rev. B*, vol. 69, p. 144413, 2004.

[127] R. Y. Umetsu, K. Kobayashi, A. Fujita, R. Kainuma, and K. Ishida *J. Appl. Phys.*, vol. 103, p. 07D718, 2008.

[128] A. Hubert and R. Schäfer, *Magnetic Domains*. Springer, 1998.

[129] Z. Q. Qui and S. D. Bader *Rev. Sci. Instrum.*, vol. 71 No. 3, p. 1243, 2000.

[130] H. R. Hulme *Proc. R. Soc. London*, vol. Ser. A 135, p. 237, 1932.

[131] S. Visnovsky *Czech. J. Phys. B*, vol. 36, p. 1424, 1986.

[132] K. Postava, D. Hrabovsky, J. Pistora, A. R. Fert, S. Visoovsky, and T. Yamaguchi *J. Appl. Phys.*, vol. 91, p. 7293, 2002.

[133] S. Yan, R. Schreiber, P. Grünberg, and R. Schäfer *J. Magn. Magn. Mater.*, vol. 210, p. 309, 2000.

[134] Q. M. Zhong, A. S. Arrott, B. Heinrich, and Z. Celinski *J. Magn. Magn. Mater.*, vol. 104, p. 1837, 1992.

[135] Q. M. Zhong, A. S. Arrott, B. Heinrich, and Z. Celinski *J. Appl. Phys.*, vol. 67, p. 448, 1990.

[136] S. Trudel, O. Gaier, J. Hamrle, and B. Hillebrands *J. Phys. D: Appl. Phys.*, vol. 43, p. 193001, 2010.

[137] J. Hamrle, S. Blomeier, O. Gaier, B. Hillebrands, K. Postava, H. Schneider, G. Jakob, and C. Felser *J. Phys. D: Appl. Phys.*, vol. 40, p. 1563, 2007.

[138] P. K. Muduli, W. C. Rice, L. He, B. A. Collins, Y. S. Chu, and F. Tsui *J. Phys.: Cond. Matt.*, vol. 21, p. 296005, 2009.

[139] S. Trudel, G. Wolf, J. Hamrle, B. Hillebrands, P. Klaer, M. Kallmayer, H. J. Elmers, H. Sukegawa, W. Wang, and K. Inomata *Phys. Rev. B*, vol. 83, p. 104412, 2011.

[140] G. Wolf, J. Hamrle, S. Trudel, T. Kubota, Y. Ando, and B. Hillebrands *J. Appl. Phys.*, vol. 110, p. 043904, 2011.

[141] S. Trudel, G. Wolf, H. Schulthei, J. Hamrle, B. Hillebrands, T. Kubota, and Y. Ando *Rev. Sci. Instrum.*, vol. 81, p. 026105, 2010.

[142] A. Hillebrands, *Annual report.* Technische Universität Kaiserslautern, 2011.

[143] S. Trudel, J. Hamrle, B. Hillebrands, T. Taira, and M. Yamamoto *J. Appl. Phys.*, vol. 107, p. 43912, 2010.

[144] M. Buchmeier, R. Schreiber, D. E. Bürgler, and C. M. Schneider *Phys. Rev. B*, vol. 79, p. 064402, 2009.

[145] R. Osgood, S. Bader, B. Clemens, R. White, and H. Matsuyama *Journal of Magnetism and Magnetic Materials*, vol. 182, p. 297, 1998.

[146] S. Bosu, Y. Sakuraba, K. Uchida, K. Saito, T. Ota, E. Saitoh, and K. Takanashi *Phys. Rev. B*, vol. 83, p. 224401.

[147] G. Nahrwold, J. M. Scholtyssek, S. Motl-Ziegler, O. Albrecht, U. Merkt, and G. Meier *J. Appl. Phys.*, vol. 108, p. 013907.

[148] C. Cowache, B. Dieny, A. Chamberod, D. Benizri, F. Berthet, S. Auffret, L. Giacomoni, and S. Nossov *Phys. Rev. B*, vol. 53, p. 15027.

[149] V. D. Ky *Phys. Stat. Sol.*, vol. 17, p. K207.

[150] I. Antonov, L. Vatskitchev, and M. Vatskitcheva *Journal of Magnetism and Magnetic Materials*, vol. 169, p. 25.

[151] K. Uchida, T. Ota, K. Harii, K. Ando, H. Nakayama, and E. Saitoh *J. Appl. Phys.*, vol. 107, p. 09A951, 2010.

[152] K. Uchida, J. Xiao, H. Adachi, J. Ohe, S. Takahashi, J. Ieda, T. Ota, Y. Kajiwara, H. Umezawa, H. Kawai6, G. E. Bauer, S. Maekawa, and E. Saitoh *Nature Materials*, vol. 9, p. 894, 2010.

[153] K. Uchida, T. Nonaka, T. Ota, and E. Saitoh *J. Appl. Phys.*, vol. 97, p. 262504, 2010.

List of publications

- E. Villanova Vidal, T. Palberg, H.J. Schöpe and H. Löwen:
  Non-equilibrium melting of colloidal crystals in confinement.
  Philosophical Magazine: Vol. 89, No. 21, 21 July 2009, 1695-1714.

- H. Schneider, E. Vilanova, B. Balke, C. Felser and G. Jakob:
  Hall effect in laser ablated Co_2(Mn,Fe)Si thin films.
  Journal of Physics D: Appl. Phys., volume 42, article 084012 (2009).

- H. Schneider, E.Vilanova Vidal, S.Chadov, G.H. Fecher, C.Felser, G.Jakob:
  Hall effect and electronic structure of $Co_2Fe_xMn_{1-x}Si$ films.
  Journal of Magnetism and Magnetic Materials 322 (2010) 579-584.

- E. Vilanova Vidal, H. Schneider, G. Jakob:
  Influence of disorder on anomalous Hall effect for Heusler compounds.
  Physical Review B 83, 174410 (2011).

- E. Vilanova Vidal, G. Stryganyuk, H. Schneider, C. Felser, G. Jakob:
  Exploring Co_2MnAl Heusler compound for anomalous Hall effect sensors.
  Applied Physics Letters 99, 132509 (2011).